Cape Peninsula
University of Technology

X-Band Substrate Integrated Waveguide (SIW) filter design with Transmission Zeros

by

ABBY OYAMA COMBO

Thesis submitted in fulfilment of the requirements for the degree

Master of Engineering: Electrical Engineering

Department of Electrical, Electronic and Computer Engineering

in the Faculty of Engineering and the Built Environment

at the Cape Peninsula University of Technology

Supervisor: Dr Susan Maas
Co-supervisor: Prof Robert van Zyl

Bellville Campus
December 2021

DECLARATION

I, Abby Oyama Combo, declare that the contents of this thesis represent my own unaided work, and that the thesis has not previously been submitted for academic examination towards any qualification. Furthermore, it represents my own opinions and not necessarily those of the Cape Peninsula University of Technology.

02/12/2021

Signed   **Date**

ABSTRACT

This thesis details the design and development of an X-band filter based on Substrate Integrated Waveguide (SIW) technology. SIW technology is introduced as an alternative to overcome some drawbacks of a planar structure (such as microstrip) and non-planar structure (such as metallic rectangular waveguide), as it combines the best aspects of the two technologies. SIW filters are low cost, compact and easy to integrate with other devices. The basic concept of SIW merges waveguide cavities' planar structures on a single dielectric high-frequency material. This is accomplished through two rows of metalized via holes in the dielectric substrate that are in between two parallel metal plates acting as the walls of the waveguide cavity.

Two design methods used to design and develop a fourth-order SIW filter are presented in this thesis. The developed SIW filter is for an X-band transmitter that will be used in a cube satellite that is developed at the French–South African Institute of Technology (F'SATI). The SIW filter is designed to have a passband ranging from 8.025 GHz to 8.425 GHz with transmission zeros at the local oscillator frequency band (6.8 GHz to 7.2 GHz) and image frequencies (5.575 GHz to 6.025 GHz).

The SIW filters are fabricated using the in-house Printed Circuit Board (PCB) prototyping machine. The measured results are in good agreement with the simulated results, hence the measured results showed that the designed SIW filters meet the filter specifications.

Key terms: Bandpass filter, CST Microwave Studio, CubeSat, F'SATI, Nanosatellite, PCB, Coupled resonator filter, SIW, SMA connectors, Transmission zero, X-band, Cavity filter.

ACKNOWLEDGEMENTS

I wish to thank the following persons and entities:

- My supervisor, Dr Susan Maas, for her continued encouragement, interest in this work, valuable advice and the knowledge she provided me with throughout the entire research project.
- Prof Robert van Zyl, for his guidance and assistance in preparation of this thesis.
- All colleagues and friends who have aided me in any way in the completion of this thesis.
- Robert Robinson, for assisting with the manufacturing of the SIW filters.
- Paul Keanly from Xsight, for CT inspection of the SIW filters.
- F'SATI, for giving me the opportunity to do the research project at the Institute.
- My family, for their continued support and motivation to work hard.

DEDICATION

For my family as a whole

TABLE OF CONTENTS

LIST OF FIGURES

LIST OF TABLES

.

GLOSSARY

Terms/Acronyms/Abbreviations	Definition/Explanation
AIS:	Automatic Identification System
ASIC:	African Space Innovation Centre
CBCPW:	Conductor-Backed Coplanar Waveguide
CBW:	Coupling Bandwidth
CPUT:	Cape Peninsula University of Technology
CPW:	Coplanar Waveguide
CST:	Computer Simulation Technology
CT:	Computed Tomography
CTE:	Coefficients of Thermal Expansion
ECal:	Electronic Calibration Module
F'SATI:	French–South African Institute of Technology
FEM:	Finite Element Model
IEEE:	Institute of Electrical and Electronics Engineers
ITU:	International Telecommunication Union
LEO:	Low Earth Orbit
LO:	Local Oscillator
OBC:	On-Board Computer
PCB:	Printed Circuit Board
RF	Radio Frequency
SIW:	Substrate Integrated Waveguide
SPENVIS:	Space Environment Information System
STK:	Systems Tool Kit
TE:	Transverse Electric
TEM:	Transverse Electromagnetic
TM:	Transverse Magnetic
TTC:	Telemetry, Tracking and Command

USB: Universal Serial Bus

VNA: Vector Network Analyser

VSWR: Voltage Standing Wave Ratio

CHAPTER 1. INTRODUCTION AND BACKGROUND

1.1   Introduction

The French–South African Institute of Technology (F'SATI) at the Cape Peninsula University of Technology (CPUT) was established in 2008. The institute offers postgraduate students an opportunity within the nanosatellite programme for research and development of subsystems used on-board CubeSats. CPUT has successfully developed two nanosatellites, namely ZACube 1 and ZACube 2, which are still in orbit, while developing MDASat-1 which will be the first South African mini-constellation of three satellites. The term 'nanosatellite' refers to a satellite weighing less than 10kg and has similar capabilities to those of larger satellites (Karunanithi et al., 2015:1).

F'SATI at CPUT is currently developing MDASat 1, a follow up mission to ZACube 2. The main objective of ZACube 2 is to monitor shipping activity in South Africa's territorial waters, by making use of the Automatic Identification System (AIS). The data from MDASat-1 will add to that already gathered by ZACube 2 and will be used by the South African government to contribute to the effective management of South Africa's territorial waters. The data gathered by the AIS and imager will require a high-speed data rate transmitter for sending back data to the ground station (De Villiers & Van Zyl, n.d:1-3).

1.2   Technical background to the research problem

A CubeSat consists of different integrated subsystems. The Telemetry, Tracking and Command (TTC) or communication subsystem is among the subsystems that comprise a CubeSat. The communication subsystem provides the interface link between the CubeSat and ground station, as well as other CubeSats in orbit. According to Larson and Wertz (1999:381), some of the TTC functions include, but are not limited to Telemetry modulation and transmission, which is responsible for receiving data from the On-Board Computer (OBC) and relaying it to the ground station; carrier tracking for use in locking onto the ground station; command reception and detection, tasked to receive the uplink signal and process it. In simple terms, the basic communication system is comprised of a transmitter and receiver onboard a CubeSat and propagation medium as illustrated in Figure 1.1 below. Figure 1.1 shows that the transmitter is responsible for transmitting status telemetry and ranging tone information during the downlink phase of the signal, and the receiver receives commands and ranging information during the uplink phase (Larson & Wertz, 1999:303).
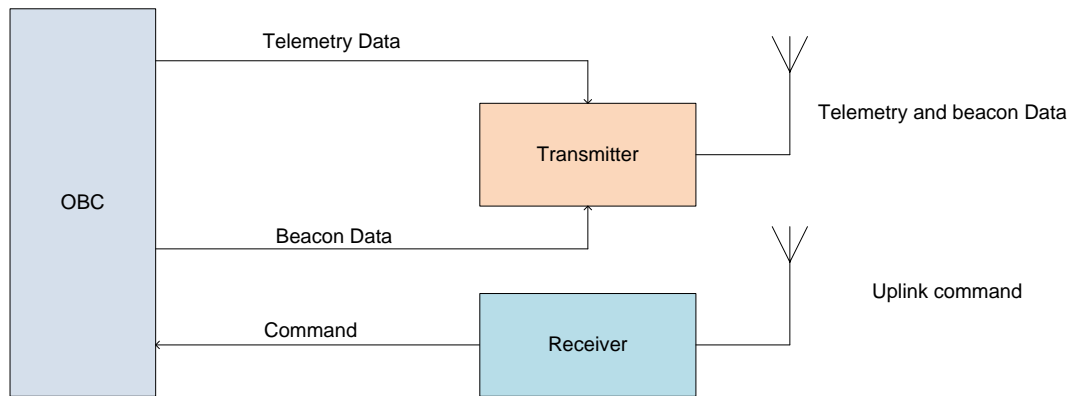
**Figure 1.1: Basic block diagram of a communication subsystem
(National Telecommunications Commission, n.d.)**

A microwave filter is one of the components used in the transmitter chain. It is used for selecting or rejecting signals at various frequencies in electronic systems such as mobile radio and satellite communications. Low-cost, lightweight and high-performance filters are required when designing microwave filters (Wu, 2001:411). The electrical performance of a microwave filter can be quantified in terms of its loss, frequency selectivity, and power-handling capacity.

Microwave filters have been developed with different structures using either microstrip or waveguide. Planar structures such as microstrip are low cost and lightweight, although they have relatively high loss factors compared with metallic waveguides. Non-planar structures, such as metallic waveguides, tend to exhibit a high quality factor; however, they are costly and heavier when compared with planar structure. Table 1.1 below illustrates the comparison between non-planar structure, such as metallic waveguide and planar sructure, such as microstrip.

Table 1.1: Comparison of a planar with a non-planar structure

	Non-planar	**Planar**
Performance	High power-handling capacity and loss sensitive	High losses
Cost	Costly	Low cost
Size	Bulky	Small size
Integration of passive and active components	Much more difficult to integrate	Easy integration

Deslandes & Wu (2001b:68-70), Fellows of the Institute of Electrical and Electronics Engineers (IEEE), have done extensive research on the design of integrated microstrip and rectangular waveguides in planar form. They conclude that taking advantage of a Substrate Integrated Waveguide (SIW) technology that combines the best of both technologies could resolve some of the above-mentioned issues.

The International Telecommunication Union (ITU) table of frequency allocation shown in Table 1.2, shows that the X-band downlink frequency band of 8.025 GHz to 8.4 GHz and 8.4 GHz to 8.45 GHz are internationally allocated for an Earth exploration satellite service and deep space research services respectively (Xie et al., 2014:433).

Table 1.2: International communication union table of frequency allocation
(National Telecommunications Commission, n.d.)

INTERNATIONAL (ITU) FREQUENCY ALLOCATIONS (REGION 3)	NATIONAL (NTC) FREQUENCY ALLOCATIONS	CHANNEL PLAN	REMARKS
8025 - 8175 MHz EARTH EXPLORATION-SATELLITE (space-to-earth) FIXED FIXED-SATELLITE (Earth-to-space) MOBILE 5.463 5.462A	8025 - 8175 MHz EARTH EXPLORATION-SATELLITE (space-to-earth) FIXED FIXED-SATELLITE (Earth-to-space) MOBILE 5.463 5.462 A		
8175 - 8215 MHz EARTH EXPLORATION-SATELLITE (space-to-earth) FIXED FIXED-SATELLITE (Earth-to-space) METEOROLOGICAL-SATELLITE (Earth-to-space) MOBILE 5.463 5.462A	8175 - 8215 MHz EARTH EXPLORATION-SATELLITE (space-to-earth) FIXED FIXED-SATELLITE (Earth-to-space) METEOROLOGICAL-SATELLITE (Earth-to-space) MOBILE 5.463 5.462 A		
8215 - 8400 MHz EARTH EXPLORATION-SATELLITE (space-to-earth) FIXED FIXED-SATELLITE (Earth-to-space) MOBILE 5.463 5.462A	8215 - 8400 MHz EARTH EXPLORATION-SATELLITE (space-to-earth) FIXED FIXED-SATELLITE (Earth-to-space) MOBILE 5.463 5.462 A	8275 - 8500 MHz Point-to-Point Radio Comm. System	ITU-R Rep 1055
8400 - 8500 MHz FIXED MOBILE except aeronautical mobile SPACE RESEARCH (space-to-earth) 5.465 5.466	8400 - 8500 MHz FIXED MOBILE except aeronautical mobile SPACE RESEARCH (space-to-earth) 5.465 5.466		

5.462A In Regions 1 and 3 (except for Japan), in the band 8 025-8 400 MHz, the Earth exploration-satellite service using geostationary satellites shall not produce a power flux-density in excess of the following values for angles of arrival (θ), without the consent of the affected administration:

-135 dB(W/m^2) in a 1 MHz band   for $0° ≤ θ <5 °$

$-135 + 0.5 (θ− 5)$ dB(W/m^2) in a 1 MHz band   for $5° ≤ θ <5 °$

-125 dB(W/m^2) in a 1 MHz band for $25° ≤ θ ≤ 90 °$

5.463 Aircraft stations are not permitted to transmit in the band 8 025-8 400 MHz (WRC-97)
5.464 (SUP-WRC-97)
5.465 In the space research service, the use of the band 8400-8 450 MHz is limited to deep space
5.4646 *Different category of service*: in Singapore and Sri Lanka, the allocation of the band 8 400-8 500 MHz to the space research service is on secondary basis

Figure 1.2 overleaf, shows the basic block diagram of the transmitter. The local oscillator (LO) frequency band of 6.8 GHz to 7.2 GHz is derived from the required transmitting band (8.025 GHz to 8.425GHz) and intermediate frequency which is the

information signal with a bandwidth of 50 MHz, that is centred at 1.225 GHz. The output frequency spectrum of the mixer, due to LO frequency band and modulation frequency, is shown in Figure 1.2.
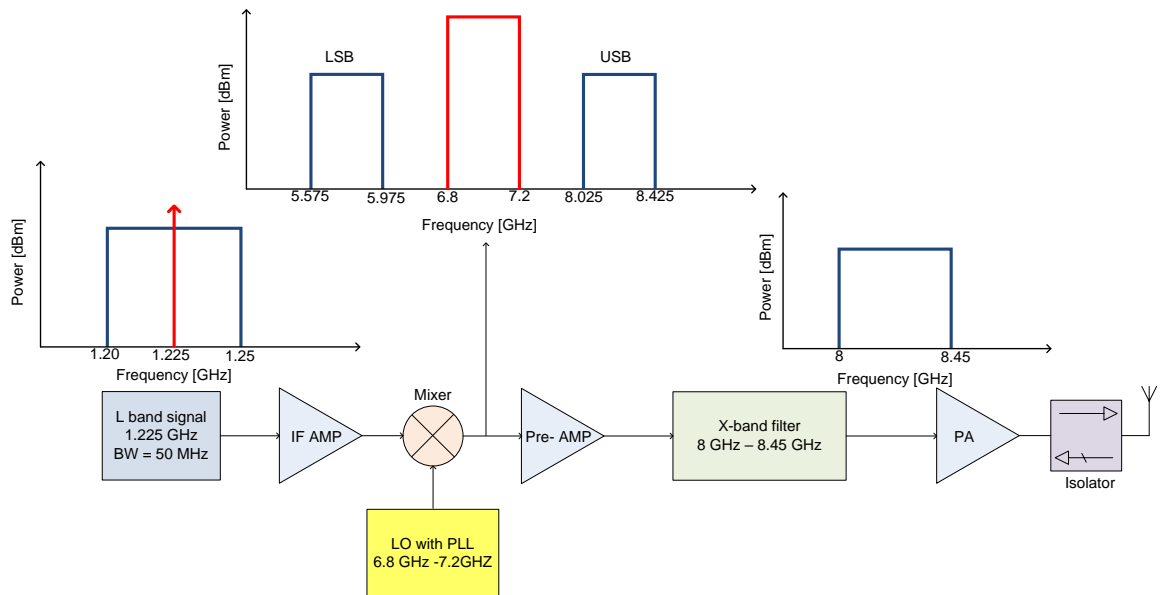
Figure 1.2: Basic block diagram of a transmitter with frequency spectrum

The upper sideband of the modulated signal presents the desired transmission frequency range. The undesired frequency components generated during the signal mixing process needs to be filtered out. Owing to the nonlinear nature of the active device (mixer), a filter that will isolate the LO and image frequency bands is needed after modulation. A filter with a passband ranging from 8 GHz to 8.45 GHz is required.

Major challenges in nanosatellite development are the mass and physical size constraints of the subsystems, while ensuring that the subsystems operate reliably in order to accomplish the CubeSat mission (Shirgur & Shannon, 2001:1). This project proposes a low-cost, lightweight and low-loss filter for an X-band transmitter for CubeSats being developed at CPUT using Substrate Integrated Waveguide (SIW) technology.

1.3   Statement of research problem

A transmitter has to fulfil certain criteria, which include: the generation of the carrier signal, modulation type and stability, ensuring as little possible drift in the carrier frequency and the spectral purity of the resulting signals. The transmitter comprises a number of components, including a filter used for both selecting and rejecting certain signals of various frequencies.

CPUT has developed an in-house S-band transmitter which has a downlink data rate of up to 2 Mbps (De Villiers & Van Zyl, n.d:3) and is currently developing MDASat-1. MDASat-1 objective is to gather navigational data of vessels sailing in South African territorial waters. The satellite is launched in low Earth orbit, where it has a limited visibility time. For this reason, it is important that a high data communication link is used to ensure that all the information collected is relayed back to Earth in a single pass. The existing S-band transmitter does not comply with this requirement, owing to its lower data rate. A transmitter with a data rate of up to 50 Mbps is currently being developed at F'SATI.

Miniaturising satellite subsystems is key when focusing on the design of CubeSat due to their requirements and constraints such as size and mass. A research that focus on the design of the X-band filter that will conform to CubeSat needs to be conducted.

1.4   Research objectives and research questions

The main objective of this research project is to study and design an SIW filter for an X-band transmitter, ranging from 8.025 GHz to 8.425 GHz. The bandwidth must be a little bit wider than 8.025 GHz to 8.425 GHz in order to have a uniform S_{21} response and a linear phase over the required band. The filter will have transmission zeros to create stop-bands at the local oscillator (6.8 GHz to 7.2 GHz) and image frequencies (5.6 GHz to 6 GHz). The S_{11} response must be less than -12 dB over the transmitting band. The S_{21} response must be less than -30 dB for transmission zeros to create stop-bands at the local oscillator and image frequencies.

The study addresses the following research questions:
- How will the performance of the filter and the SWaP-C going to be balanced to meet CubeSat standards?
- What can be achieved with SIW technology for CubeSats?
- Which coupled resonator filter topology will give the best possible results?

1.5   Research design and methodology

There are various techniques that can be used to achieve the specific research objectives, for example the filter design by the image parameter method and filter design by the insertion loss method/network synthesis method. For this research, the following methods were used:

1.5.1 Design methods

The SIW filter is designed using two different design methods. The first design method is based on the calculations of the Chebyshev *g* values from the specifications as discussed in Section 6.2. Then followed by the computation of the coupling matrix of the coupled resonator filter from the Chebyshev *g* values. The second method involves generation of the transfer and reflection polynomials from the prescribed transmission zeros. Then followed by the calculation of coupling element values from the transfer and reflection polynomials as described in Section 6.3. The literature study of SIW technology discussed in Chapter 4 and 5 is then used to design the X-band SIW filter on the Rogers 4003C™ substrate.

1.5.2 Modelling and simulation

The SIW cavities are added to the structure and tuned for desired frequency response using CST Microwave Studio®. CST Microwave Studio® is used to model the SIW filter structure in order to depict how the structure will behave in the real world. The simulated results are optimised to more closely meet the expected results.

1.5.3 Construction and testing

The SIW filter is constructed on the Rogers 4003C™ material with 1.524 mm thickness as described in Chapter 6 and 7. The HP 8720 ET VNA is used to test the manufactured SIW filter and compare the measured results with the simulated results.

1.6 Delineation

The spatial test is necessary to check the capability of the filter in the space environment. Although there are modelling tools like SPENVIS and Systems Tool Kit (STK) used by satellite engineers and spacecraft designers to give a representative example of the radiation environment that CubeSats will be exposed to, no radiation test is done as part of this research.

1.7 Significance of the research

The research study of the SIW filter will play an important role by making it easier to design SIW filters for X-band transmitter being developed at F'SATI for future cube satellites.

1.8 Expected outcome, results and contributions of the research

This research will produce an alternative filter that is lightweight, low cost and compact in size for the X-band transmitter that is being developed at F'SATI for a cube satellite. The filter is designed using SIW design guidelines and filter theory.

1.9   Structure of the thesis

Chapter 2 presents the theoretical part of filter design. Then the design process of the synthesis method, which includes generation of Chebyshev transfer and reflection polynomials, coupling matrix synthesis and impedance and admittance inverters, is also discussed in detail. Chapter 3 then discusses the technical study of waveguides and resonant cavities as they both have similar field propagation to SIW structures. The modes that can propagate in waveguides are also discussed in detail. Chapter 4 focuses on the literature review of SIW filters, detailing the importance of choosing a substrate as it is directly related to the size, losses, thermal stability and power handling of the SIW filter. Chapter 4 also presents SIW design guidelines and the performance of SIW resonators by comparing them with other resonators in terms of size, cost and losses. Chapter 5 discusses the filter theory to SIW, including miniaturization techniques of the SIW. Chapter 6 documents the design methods, modelling process and simulated results. The manufacturing steps of the SIW filter are outlined in Chapter 7, and then followed by the comparison of measured results with simulated results. Chapter 8 concludes the thesis by presenting recommendations for future work.

CHAPTER 2. FILTER THEORY

2.1   Introduction

This chapter outlines the background of filters, including the basic applications of filters, and then discusses in detail the filter design process by insertion loss. The method of generating the polynomials which represent the transfer and reflection characteristics of the filter to be realised, is also described in this chapter. Impedance and admittance inverters, including the coupling bandwidth and external quality factors used to design the coupled-resonator filter, are also presented in this chapter. The theory and design of filters are supplemented by a literature study conducted in various relevant sources.

2.2   History of filters

When the carrier telephony system was introduced in 1910, there was a need to develop a new technology that would extract and detect signals contained within a specific frequency band. This advanced the research and development of filter technology (Makimoto & Yamashita, 2001:1). The scientist K.W. Wagner established a filter design method in 1915, known as the Wagner filter, while G. Campbell proposed another design method which was later known as the image parameter method (Makimoto & Yamashita. 2001:1). According to Matthaei et al. (1980:83), Darlington and others introduced a network synthesis method that uses low-pass prototypes that are normalised in terms of impedance and frequency as the initial stage of filter design.

2.2.1 Applications of filters

Microwave frequencies are frequencies that range between 3 GHz and 300 GHz, with an electrical wavelength between 10 cm and 1mm (Pozar, 2012:1). According to Hunter (2001:1), microwave filters have various applications, which include but are not limited to, military, satellite and cellular radio communications.

- Satellite communication applications: From Kudsia et al. (1992:1133), the development of satellite communication started in the late 1960s with the launch of the Intelsat I, II and III series which found a better way of providing voice communication. The launch of Intelsat IV in 1971 established the commercial viability of satellite communication; this was followed by the launch of a Canadian domestic satellite. A block diagram of a communication payload of these satellites is illustrated in Figure 2.1. The communication payload in Figure 2.1 is made up of receive and transmit antennae, a low-noise amplifier and down-converter, input and output multiplexer and high-power amplifiers. The signal received in the satellite is channelled into a number of RF channels and then amplified separately using a low-noise amplifier. The multiplexer is

used to combine the signals before transmission via a common antenna. Owing to the nonlinearities of amplifiers and mixers, a microwave filter is needed to suppress the undesired signals.
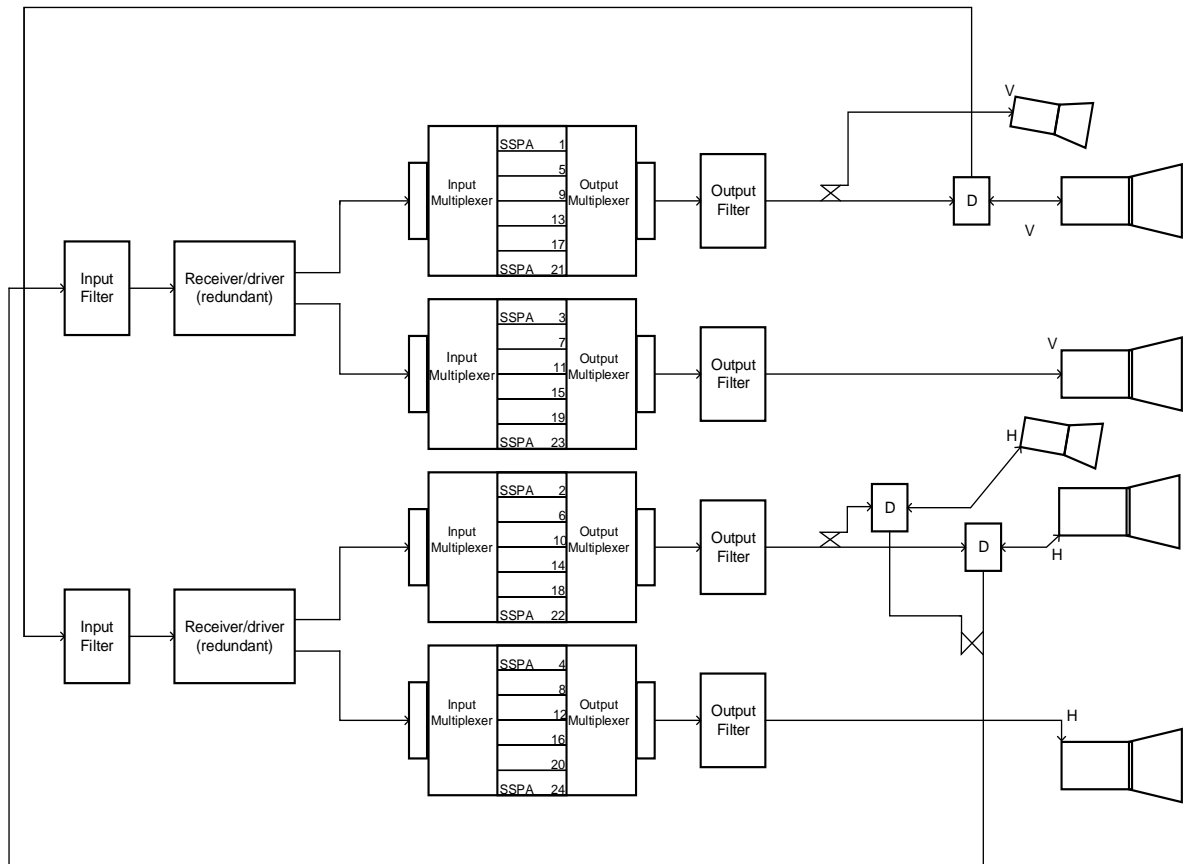
Figure 2.1: Block diagram of a communication payload
(Kudsia et al., 1992:1133)

- Cellular communication application: Hunter (2001:1-2) discussed the application of filters in cellular communication by illustrating the block diagram of the RF front-end cellular base station as shown in Figure 2.2. The base station in Figure 2.2 normally transmits and receives simultaneously. The power amplifier amplifies the signal for transmission through the antenna and the transmitter generates 30W high-power signals. The harmonics and intermodulation products produced by the transmit power amplifier need to be filtered out to prevent their being fed into the receiver. Thus, the filter needed in the transmitter must have a high level of attenuation in order to protect the receiver from the 30W transmit power. A low-passband insertion loss is also needed in the filter of the transmitter to satisfy power amplifier linearity and efficiency requirements.
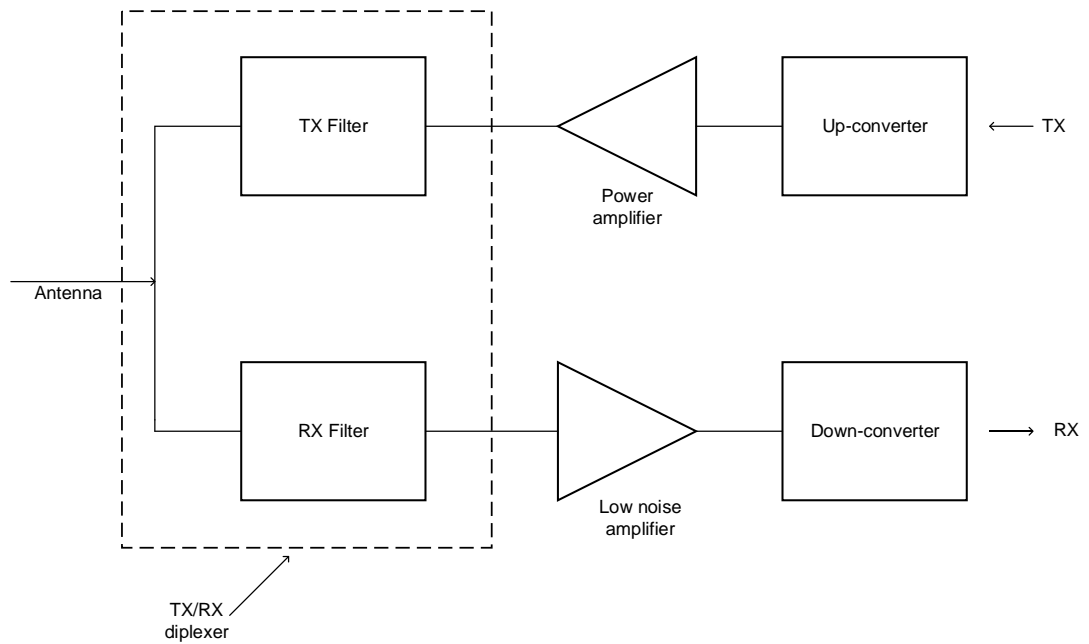
Figure 2.2: RF front end of a cellular base station
(Hunter, 2001:1)

- Military application: Radar for military use originated in World War II, and its application has been extended to other areas, such as guiding aeroplanes to safe landing in foggy and stormy weather (Tsui, 1992:1). Normally, when a new weapon is developed, another way to interfere with and defeat it is investigated. Thus, an electronic warfare receiver is needed to detect whether there is a radar signal. According to Tsui (1992:134-135), the superheterodyne receiver in electronic warfare applications is used to isolate an input signal and measure its fine information. The basic block diagram of the superheterodyne receiver shown in Figure 2.3 is made up of a mixer, local oscillator, IF filter, amplifier and video detector. The mixer generates the difference and the sum of the two input signals, which are usually called down-conversion and up-conversion respectively. Owing to the non-linearity of the mixer, the filter is often needed to pass the desired frequency band and stop all other intermodulation frequencies to avoid confusion of the receiver measurement.
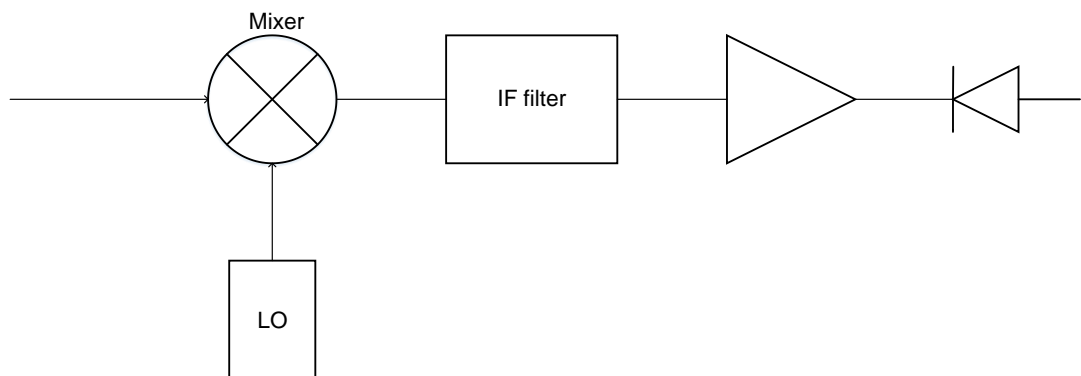
Figure 2.3: Basic block diagram of the superheterodyne receiver
(Tsui, 1992:135)

Microwave filters can be designed by using lumped element filter design theory as an initial design step that will allow the conversion into distributed elements. The lumped element filter design works well at low frequencies, but at microwave frequencies, the self-resonant frequency (SRF) of inductors and capacitors becomes a problem. Depending on the filter design approach used, lumped elements at microwave frequencies are approximated using distributed elements while other design approach originates with the TEM transmission lines.

2.3   Filter design by insertion method

The design process, by means of insertion loss, is illustrated by Pozar (2012:402) as in Figure 2.4.
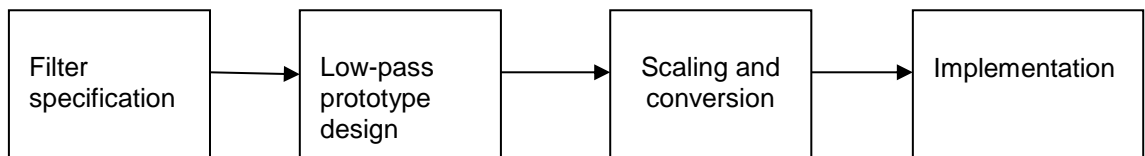
Figure 2.4: Design process by insertion loss
(Pozar, 2012:202)

1. **Filter specification**: The filter specifications describe the features of the filter. The minimum insertion loss at some frequencies on the stopband, return loss on the passband, and magnitude or phase over the frequency band, are usually specified for the design of the filter.

2. **Design of low-pass prototype**: The low-pass prototype is a passive, reciprocal, normally lossless two-port network which is designed to operate at a source impedance of 1Ω and a cut-off frequency ω_c of 1 rad/sec (Hunter, 2001:49). The normalised impedance and frequency simplify the design of the filter. Low-pass prototypes are used as a sample to produce a qualified filter design for filter specifications. The low-pass prototype parameters (g_i) are obtained from the filter specifications. Then the filter specifications help to guide which transfer function and filter order are suitable for the required filter response.

(a) Butterworth transfer function: It exhibits monotonic attenuation in the passband and offers fair selectivity. This means there is a very little ripple in the passband with moderate steepness in the transition region. Most of the energy is transmitted in the passband, meaning there is a low Voltage Standing Wave Ratio (VSWR) within the passband. The insertion amplitude is given mathematically by Equation 2.1 overleaf, where f is the frequency at which the attenuation is desired, f_c is the cut-off frequency, and N is the order of the filter (Pozar, 2012:399-400).

$$S_{21}=10\log\left[1+\left(\frac{f}{f_c}\right)^{2N}\right] \text{ [dB]} \hspace{3cm} 2.1$$

(b) Chebyshev transfer function: This has a non-monotonic passband and better selectivity. There is a ripple in the passband with an increased rate of attenuation in the transition region. Some of the energy is reflected, causing a VSWR ripple in the passband. The insertion amplitude for a Chebyshev function is given by Equation 2.2 below (Matthaei et al., 1980:86). According to Hong (2011:41-43), the minimum return loss L_r or the maximum VSWR in the passband is specified instead of passband ripple l_{ripple}. Equations 2.2 to 2.4 give the relationship among the minimum return loss, VSWR, and the corresponding passband ripple.

$$S_{21}=10\log\left[1+\varepsilon\cosh^2\left(N\cosh^{-1}\left(\frac{f}{f_c}\right)\right)\right] \text{ [dB]}, \hspace{2cm} 2.2$$

$$\text{where } \varepsilon=\left[\log^{-1}\left(\frac{l_{ripple}}{10}\right)-1\right].$$

$$l_{ripple}=-10\log\left(1-10^{0.1L_r}\right)=-10\log\left[1-\left(\frac{\text{VSWR-1}}{\text{VSWR+1}}\right)^2\right] \text{ [dB]} \hspace{1cm} 2.3$$

$$\text{VSWR}=\frac{1+|S_{11}|}{1-|S_{11}|} \hspace{3cm} 2.4$$

The equations that can be used to calculate prototype element values for the Chebychev filter, that are similar to the ones shown in Table 2.1 on page 14, are given by Matthaei et al. (1980:99) as follows:

$$\left.\begin{array}{l} \beta = \ln\left(\coth\dfrac{l_{ripple}}{17.37}\right) \\[4mm] \gamma = \sinh\left(\dfrac{\beta}{2N}\right) \\[4mm] a_k = \sin\left[\dfrac{(2k-1)\pi}{2N}\right], k=1,2,...n \\[4mm] b_k = \gamma^2 + \sin^2\left(\dfrac{k\pi}{N}\right), k=1,2,...n \\[4mm] g_1 = \dfrac{2a_1}{\gamma} \\[4mm] g_k = \dfrac{4a_{k-1}a_k}{b_{k-1}g_{k-1}}, k=2,3,...n \\[4mm] g_{n+1} = \left[\begin{array}{ll} 1 & N=odd \\ \coth^2\left(\dfrac{\beta}{4}\right) & N=even \end{array}\right] \end{array}\right\} \hspace{1cm} 2.5$$

12

(c) Bessel function: It is characterised by a monotonic passband but it has very poor selectivity. It exhibits a maximally flat group delay over the band. It has a linear phase response in the passband to avoid distortion. When the system requires that the group delay be flat and selectivity is not a requirement, this function can be an ideal candidate. Attenuation of the Bessel function is given by the expression below (Matthaei et al., 1980:111).

$$S_{21} = \frac{10\left(\frac{f}{f_c}\right)^2}{(2N-1)\ln 10} \ [\text{dB}].$$
2.6

Group delay is the propagation time of a signal through the filter. Group delay is defined as the rate of change of phase with frequency and its mathematical expression is given by $\tau_g = \frac{d\theta}{d\omega}$. A linear phase response on the passband will result in a maximally flat group delay.

(d) Filter order (N): The order of the filter determines its behaviour, where higher-order filters are required to achieve steeper slopes in the transition region, which will result in better selectivity. The order of the low-pass filter is equal to the number of reactive elements in the filter.

The amplitude response of the filter is designed to, at least, meet a minimum specification on the passband return loss and stopband insertion loss (Hunter, 2001:49). With filter specifications given, the required filter order (N) to satisfy the insertion loss can be determined from the graph similar to the one in Figure 2.5. A table of elements, similar to Table 2.1 on page 14, gives the prototype element values. Figure 2.6 shows examples of prototype circuits. The element values are in Farad for capacitors and Henry for inductors.
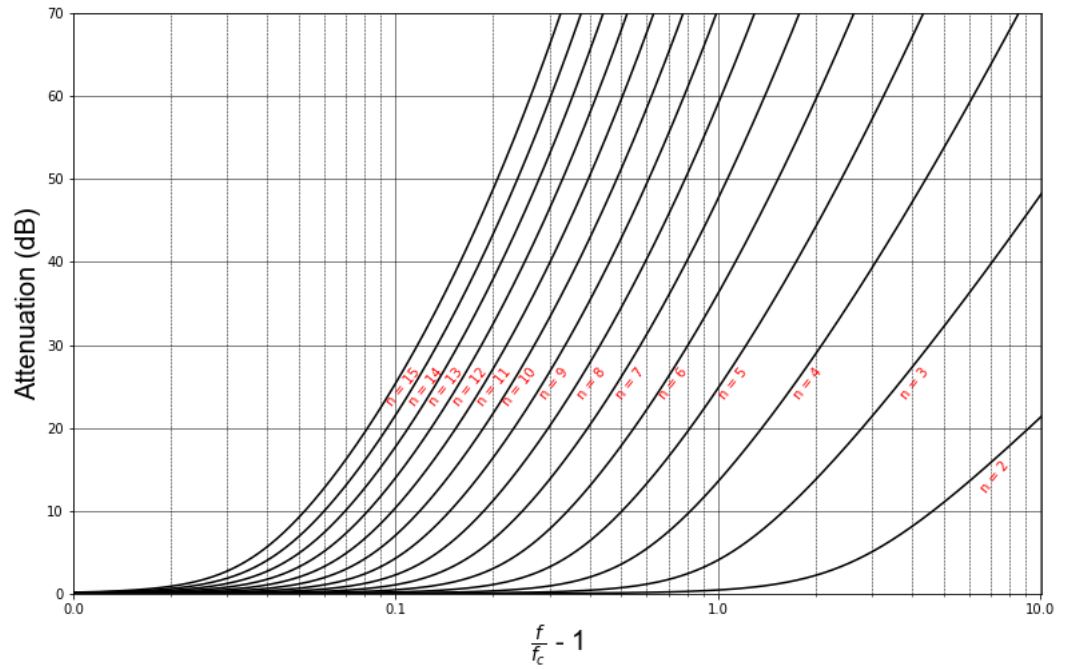
Figure 2.5: Attenuation versus normalised frequency for Chebyshev filters with 0.01 dB ripple (Matthaei et al., 1980:88)

Table 2.1: Element values for maximally flat time delay low-pass filter prototype (Pozar, 2012:408)

N	g_1	g_2	g_3	g_4	g_5	g_6	g_7	g_8	g_9	g_{10}	g_{11}
1	2.0000	1.0000									
2	1.5774	0.4226	1.0000								
3	1.2550	0.5528	0.1922	1.0000							
4	1.0598	0.5116	0.3181	0.1104	1.0000						
5	0.9303	0.4577	0.3312	0.2090	0.0718	1.0000					
6	0.8377	0.4116	0.3158	0.2364	0.1480	0.0505	1.0000				
7	0.7677	0.3744	0.2944	0.2378	0.1778	0.1104	0.0375	1.0000			
8	0.7125	0.3446	0.2735	0.2297	0.1867	0.1387	0.0855	0.0289	1.0000		
9	0.6678	0.3203	0.2547	0.2184	0.1859	0.1506	0.1111	0.0682	0.0230	1.0000	
10	0.6305	0.3002	0.2384	0.2066	0.1808	0.1539	0.1240	0.0911	0.0557	0.0187	1.0000
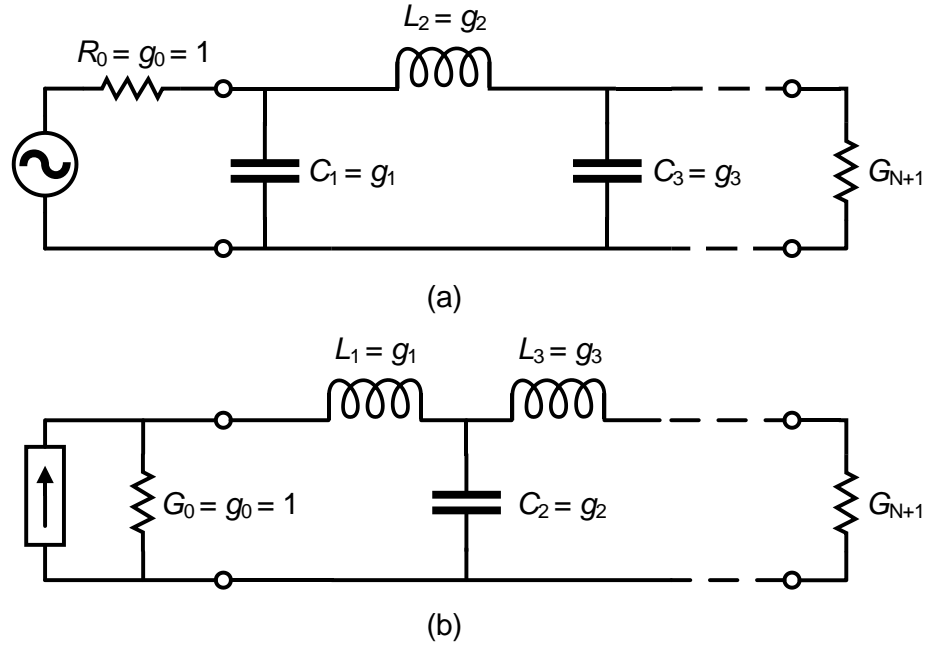
Figure 2.6: Example of a low-pass prototype circuit. (a) Prototype beginning with shunt element. (b) Prototype beginning with a series element (Pozar, 2012:403).

3. **Scaling and conversion:** The low-pass prototype is denormalised from its 1Ω source impedance and 1 rad/s cut-off frequency to the desired cut-off frequency and source impedance (R_0). The capacitor and inductor in the prototype filter are converted to the actual values using the equations below (Pozar, 2012:409).

$$C_k = \frac{g_k}{2\pi f_c R_0}$$

2.7

$$L_k = \frac{R_0 g_k}{2\pi f_c}.$$

2.8
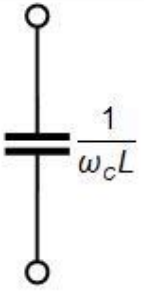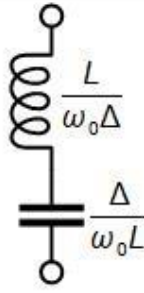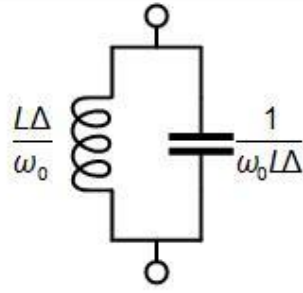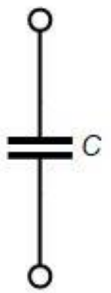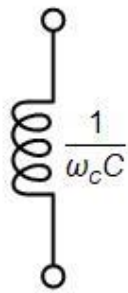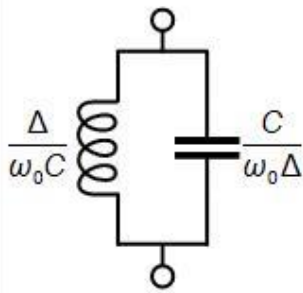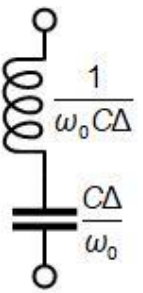
The input and output termination resistances is equal to unity (1) in the prototype design, except for Chebyshev filters which have a nonunity output termination resistance for an even order number (Pozar, 2012:408). The source resistance is equal to the load resistance when the input and output termination resistance in the prototype design is equal. When the input resistance is not equal to the output termination resistance, the load resistance is given by the equation below.

$$R_L = \frac{R_0 g_{N+1}}{g_0}.$$

2.9

Low-pass prototype filter designs can be transformed to have high-pass, bandpass or bandstop responses as summarised in Table 2.2 overleaf, where ω_2 and ω_1 are the

15

frequency cutoffs of the bandpass and bandstop filters. Impedance scaling is not included in Table 2.2. The centre frequency ω_0 is the arithmetic mean of ω_1 and ω_2. The first row in Table 2.2 is for the series component, while the second row is for the shunt component. The filter order (N) of the bandpass filter can be determined from the chart similar to the one in Figure 2.5, by using Equation 2.10 below.

Table 2.2: Prototype filter transformation - $\Delta=\frac{\omega_2-\omega_1}{\omega_0}$ (Pozar, 2012:414)

$$\frac{\omega}{\omega_c}=\frac{1}{\Delta}\left(\frac{f}{f_0}-\frac{f_0}{f}\right)$$

2.10

4. **Implementation:** Lumped components become impractical to implement at microwave frequencies because of the self-resonant frequency (SRF) of inductors and capacitors that becomes a problem. Therefore, distributed elements, such as open- or short-circuit transmission line stubs, are often used to approximate lumped elements while other design approach originates with the TEM transmission line (Pozar, 2012:416). Kuroda's identities and Richards' transformations are used to convert lumped element filter design to a distributed filter. According to Pozar (2012:416), Richards' transformation is used to overcome the problem of lumped components having a limited range of values by converting lumped elements to the transmission line section, while Kuroda's identities are used to separate filter elements by cascaded transmission line sections. In Richards' transformation, the inductor is replaced with a short-circuit stub and the capacitor is replaced with an open-circuit stub as illustrated in Figure 2.7.
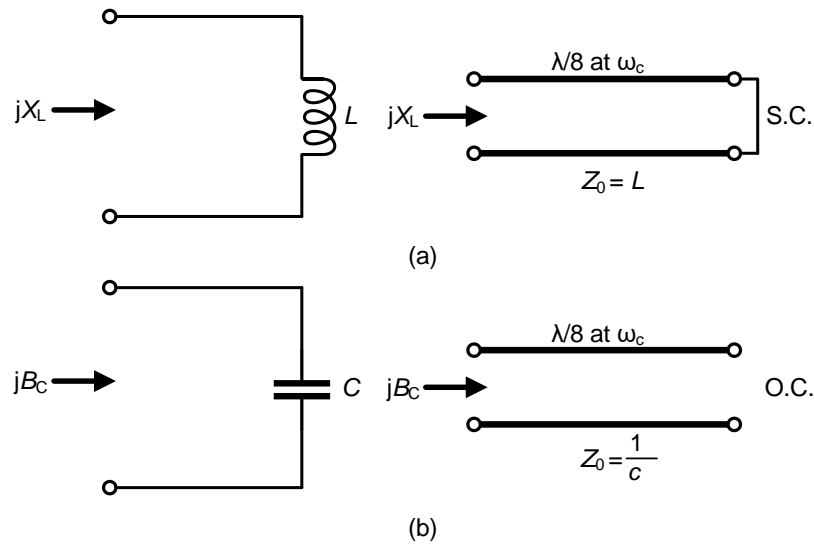
Figure 2.7: Richards' transformation. (a) Inductor to a short stub (b) Capacitor to an open stub (Pozar, 2012:417).

According to Pozar (2012:421), Kuroda's identities are not useful for bandstop and bandpass filters, but the inverters are useful for bandpass and bandstop filters that have a bandwidth of less than 10%. These inverters are of utmost importance for modelling the coupled resonator filter (Pozar, 2012:421). The impedance inverter works like a quarter-wavelength line of characteristic impedance K at all frequencies, and similarly, the admittance inverter also works like a quarter-wavelength line of characteristic admittance J at all frequencies (Matthaei et al.,1980:144).

2.4 Generation of the Chebyshev transfer and reflection polynomials

The method for generating the Chebyshev transfer and reflection polynomials with prescribed transmission zeros as presented by Cameron et al. (2018:189-196) is outlined in this section. The transfer and reflection functions of any two port lossless filter network composed of N interconnected resonator cavities may be defined as the ratio of two N^{th} degree polynomials as in Equation 2.11.

$$S_{11}(\omega)=\frac{F_N(\omega)}{\varepsilon_r E_N(\omega)} \quad , \quad S_{22}(\omega)=\frac{P_N(\omega)}{\varepsilon E_N(\omega)} \qquad \text{2.11}$$

In Equation 2.11, ω is the real frequency variable related to the complex variable s by $s=j\omega$, where $\varepsilon_r=1$ for partial canonical function or $\varepsilon_r=\varepsilon/\sqrt{\varepsilon^2-1}$ if the function is fully canonical, and ε is a ripple constant normalising $S_{21}(\omega)$ to the equiripple at $\omega=\pm1$ and it can be expressed in terms of the prescribed return loss (RL) in decibels as follows.

$$\varepsilon=\frac{1}{\sqrt{10^{\frac{RL}{10}}-1}}\left|\frac{P_N(\omega)}{F_N(\omega)}\right|_{\omega=1} \qquad \text{2.12}$$

The polynomials are assumed to be normalised so that their highest degree are unity. Equation 2.11 shows $S_{11}(\omega)$ and $S_{21}(\omega)$ have a common denominator $E_N(\omega)$, zeros of $S_{11}(\omega)$ (roots of the polynomial $F_N(\omega)$) are points of zero reflected power known as reflection zeros and zeros of $S_{21}(\omega)$ (roots of the polynomial $P_N(\omega)$) are the prescribed transmission zeros of the filtering function. The roots of $E_N(\omega)$ (poles of $S_{11}(\omega)$ and $S_{21}(\omega)$) are real or conjugate pairs and the real part must be negative (strict Hurwitz polynomial). The roots of $F_N(\omega)$ can be everywhere in the complex plane and the roots of $P_N(\omega)$ can be on the imaginary axis (conjugate pair) or on the real axis (pairs with opposite values) or as a complex pair.

For lowpass and bandpass filters, the degree of $F_N(\omega)$ (the numerator polynomial of $S_{11}(\omega)$) is equal to N and for bandstop filter the degree of $F_N(\omega)$ can be less than N (Cameron et al., 2018:178). The number of transmission zeros with finite position is assumed to be n_{fz} and $n_{fz} \le N$ and if $n_{fz} < N$, the transmission zeros without finite position must be placed at infinity. When all the transmission zeros are prescribed at finite frequencies that is $n_{fz} = N$ (for fully canonical filters), ε_r is given by $\varepsilon_r = \varepsilon / \sqrt{\varepsilon^2 - 1}$ in equation 2.11. Recalling the conservation of energy formula $|S_{11}|^2 + |S_{21}|^2 = 1$ for a two-port lossless system and Equation 2.11, the transfer function can be defined in terms of the Chebyshev filtering function $C_N(\omega)$ as in Equation 2.13 where $C_N(\omega)$, the filtering function of degree N is given in Equation 2.14.

$$|S_{21}(\omega)|^2 = \frac{1}{1 + \varepsilon^2 C_N^2(\omega)}$$ 2.13

$$C_N = \frac{F_N(\omega)}{P_N(\omega)}$$ 2.14

$C_N(\omega)$ has a form for the general Chebyshev characteristic shown in Equation 2.15 where $x_n = (\omega - 1/\omega_n)/(1 - \omega/\omega_n)$ and $j\omega_n = s_n$ is the position of the nth transmission zero in the complex frequency domain.

$$C_{N(\omega)} = \cosh\left[\sum_{n=1}^{N} \cosh^{-1}(x_n)\right]$$ 2.15

Cameron et al. (2018:197) continues with the polynomial synthesis procedure by replacing $\cosh^{-1}(x)$ in Equation 2.15 with its identity $\cosh^{-1}(x) = \ln\left(x + \sqrt{x^2 - 1}\right)$ which gives Equation 2.16.

$$C_{N(\omega)} = \cosh\left[\sum_{n=1}^{N} \ln(a_n + b_n)\right], \qquad a_n = x_n, \qquad b_n = \sqrt{x_n^2 - 1} \qquad\qquad 2.16$$

Then by using the identity $\cosh(x) = \ln(e^x + e^{-x})/2$, Equation 2.16 is rewritten as in Equation 2.17.

$$C_N(\omega) = \frac{1}{2}\left[\exp\left(\sum_{n=1}^{N}\ln(a_n+b_n)\right) + \exp\left(-\sum_{n=1}^{N}\ln(a_n+b_n)\right)\right]$$

$$= \frac{1}{2}\left[\prod_{n=1}^{N}(a_n+b_n) + \frac{1}{\prod_{n=1}^{N}(a_n+b_n)}\right] \qquad\qquad 2.17$$

When the numerator and denominator of the second term in Equation 2.17 is multiplied by $\prod_{n=1}^{N}(a_n+b_n)$ and noting that $\prod_{n=1}^{N}(a_n^2+b_n^2)=1$ gives Equation 2.18.

$$C_N(\omega) = \frac{1}{2}\left[\prod_{n=1}^{N}(a_n+b_n) + \prod_{n=1}^{N}(a_n-b_n)\right] \qquad\qquad 2.18$$

By using $a_n = x_n = (\omega - 1/\omega_n)/(1 - \omega/\omega_n)$ and $b_n = \sqrt{x_n^2 - 1}$ as given in Equation 2.15 and 2.16, Equation 2.18 can be expressed in its final form as in Equation 2.19, where $c_n = \omega - 1/\omega_n$, $\omega' = \sqrt{\omega^2 - 1}$ and $d_n = \omega'\sqrt{1 - 1/\omega_n^2}$.

$$C_N(\omega) = \frac{1}{2}\left[\frac{\prod_{n=1}^{N}(c_n+d_n) + \prod_{n=1}^{N}(c_n-d_n)}{\prod_{n=1}^{N}\left(1 - \frac{\omega}{\omega_n}\right)}\right] \qquad\qquad 2.19$$

Now $C_N(\omega)$ is arranged in the form of numerator and denominator, so by comparing equations 2.19 and 2.14 it can be seen that the numerator of $C_N(\omega)$ is $F_N(\omega)$, the numerator of the reflection function $S_{11}(\omega)$ whose zeros correspond to the reflection zeros and the denominator of $C_N(\omega)$ is $P_N(\omega)$ whose zeros correspond to the prescribed transmission zeros. The numerator of Equation 2.19 is rewritten as follows:

$$\text{num}[C_N(\omega)] = \frac{1}{2}\left[G_N(\omega) + G_N'(\omega)\right] = F_N(\omega) \qquad\qquad 2.20$$

Where

$$G_N(\omega) = \prod_{n=1}^{N}[c_n+d_n] = \prod_{n=1}^{N}\left[\left(\omega - \frac{1}{\omega_n}\right) + \omega'\sqrt{\left(1 - \frac{1}{\omega_n^2}\right)}\right] \qquad\qquad 2.21$$

$$G_N'(\omega) = \prod_{n=1}^{N}[c_n-d_n] = \prod_{n=1}^{N}\left[\left(\omega - \frac{1}{\omega_n}\right) - \omega'\sqrt{\left(1 - \frac{1}{\omega_n^2}\right)}\right] \qquad\qquad 2.22$$

19

The polynomial $G_N(\omega)$ is rewritten as the sum of the two polynomials $U_N(\omega)$ and $V_N(\omega)$, where $U_N(\omega)$ contains coefficients in terms of ω only, while $V_N(\omega)$ contains coefficients that are multiplied by the transformed variable frequency ω' as follows.

$$G_N(\omega)=U_N(\omega)+V_N(\omega) \tag{2.23}$$

$$U_N(\omega)=u_0+u_1\omega+u_2\omega^2+\ldots+u_N\omega^N \tag{2.24}$$

$$V_N(\omega)=\omega'\left(v_0+v_1\omega+v_2\omega^2+\ldots+v_N\omega^N\right) \tag{2.25}$$

The recursive process starts by setting $n=1$ which corresponds to the first prescribed transmission zero, ω_1, in Equations 2.21 to 2.23 as illustrated below.

$$G_1(\omega)=\left(\omega-\frac{1}{\omega_1}\right)+\omega'\sqrt{\left(1-\frac{1}{\omega_1^2}\right)}=U_1(\omega)+V_1(\omega) \tag{2.26}$$

With the reference to Equation 2.21, $G_1(\omega)$ from the previous equation has to be multiplied by the terms corresponding to the second prescribed transmission zero, ω_2, to compute $G_2(\omega)$.

$$G_2(\omega)=G_1(\omega)(c_2+d_2)=[U_1(\omega)+V_1(\omega)]\left[\left(\omega-\frac{1}{\omega_2}\right)+\omega'\sqrt{\left(1-\frac{1}{\omega_2^2}\right)}\right]$$
$$=U_2(\omega)+V_2(\omega) \tag{2.27}$$

Then the equations for $U_2(\omega)$ and $V_2(\omega)$ are given below.

$$U_2(\omega)=\omega U_1(\omega)-\left(\frac{1}{\omega_2}\right)U_1(\omega)+\sqrt{\left(1-\frac{1}{\omega_2^2}\right)}\,\omega'V_1(\omega) \tag{2.28}$$

$$V_2(\omega)=\omega V_1(\omega)-\left(\frac{1}{\omega_2}\right)V_1(\omega)+\sqrt{\left(1-\frac{1}{\omega_2^2}\right)}\,\omega'U_1(\omega) \tag{2.29}$$

The process is repeated with the 3rd prescribed transmission zero, ω_3, up to all the prescribed transmission zeros (including the transmission zeros at infinity) by multiplying [c_n+d_n] by $G_{n-1}(\omega)$ to find $G_n(\omega)=U_N(\omega)+V_N(\omega)$. From Equation 2.26, the equations that can be used to compute $U_1(\omega)$ and $V_1(\omega)$ are as follows:

.

$$U_1=\omega-\frac{1}{\omega_1} \qquad\qquad 2.30$$

$$V_1=\omega'\sqrt{\left(1-\frac{1}{\omega_1^2}\right)} \qquad\qquad 2.31$$

The general equations for $U_N(\omega)$ and $V_N(\omega)$ for $n=2\ldots,N$ are given below by equations 2.32 and 2.33 respectively, where $\omega'=\sqrt{\omega^2-1}$.

$$U_N(\omega)=\omega U_{N-1}(\omega)-\frac{1}{\omega_N}U_{N-1}(\omega)+\sqrt{\left(1-\frac{1}{\omega_N^2}\right)}\omega'V_{N-1}(\omega) \qquad\qquad 2.32$$

$$V_N(\omega)=\omega V_{N-1}(\omega)-\frac{1}{\omega_N}V_{N-1}(\omega)+\sqrt{\left(1-\frac{1}{\omega_N^2}\right)}\omega'U_{N-1}(\omega) \qquad\qquad 2.33$$

When the same process is repeated for $G_N'(\omega)=U_N'(\omega)+V_N'(\omega)$, it is found that $U_N'(\omega)=U_N(\omega)$ and $V_N'(\omega)=-V_N(\omega)$, then from Equation 2.20 it is also found that $F_N(\omega)=U_N(\omega)$. Thus equations 2.20 and 2.24 shows that the numerator of $C_N(\omega)$ which has the same zeros as $F_N(\omega)$, is $U_N(\omega)$ after N-1 cycles of this recursion process and the reflection zeros can be found by rooting $U_N(\omega)$ while rooting $V_N(\omega)$ will give the N-1 in band reflection maxima. The prescribed set of transmission zeros will make up the polynomial $P_N(\omega)$. It remains to determine the polynomial $E_N(\omega)$, to complete the characteristic polynomials. The $S_{11}(\omega)$ and $S_{21}(\omega)$ denominator polynomial $E_N(w)$ can be found using Equation 2.34 which is derived by Cameron et al. (2018:186-188), from the conversation energy formula $S_{11}(\omega)S_{11}^*(\omega)+S_{21}(\omega)S_{21}^*(\omega)=1$ or $F(\omega)F^*(\omega)/\varepsilon_r^2+P(\omega)P^*(\omega)/\varepsilon^2=E(\omega)E^*(\omega)$.

$$\varepsilon^2\varepsilon_r^2E(\omega)E^*(\omega)=[\varepsilon_rP(\omega)-j\varepsilon F(\omega)][\varepsilon_rP(\omega)+j\varepsilon F(\omega)] \qquad\qquad 2.34$$

With polynomials $P_N(\omega)$ and $F_N(\omega)$ normalised to their respective highest order coefficients in Equation 2.34, by rooting one of the two terms on the right-hand side will result in a pattern of singularities alternating between left half and right half planes. Rooting the other term will give the complementary set of singularities. All the roots that have a negative real part will be used to construct the polynomial $E_N(\omega)$, since Polynomial $E_N(\omega)$ is known to be strict Hurwitz polynomial.

2.5   Coupling matrix synthesis

The first step in the synthesis procedure, which is to derive the transfer and reflection polynomials, is presented in the previous section. The second step in the synthesis

procedure is to calculate the values of the coupling elements of a canonical coupling matrix from the transfer and reflection polynomials. The three commonly used forms of the canonical matrix are folded, arrow or transversal. In this section, the synthesis of the rational polynomials for the short-circuit admittance parameters $y_{21}(=y_{12})$ and y_{22} from the transfer/reflection polynomials is outlined, as described by Cameron et al. (1999:436-442). For a two-port lossless filter network with a voltage source of internal impedance R_1 and load impedance R_N normalised to 1Ω as illustrated in Figure 2.8, the following Equations 2.35 to 2.38 are obtained.
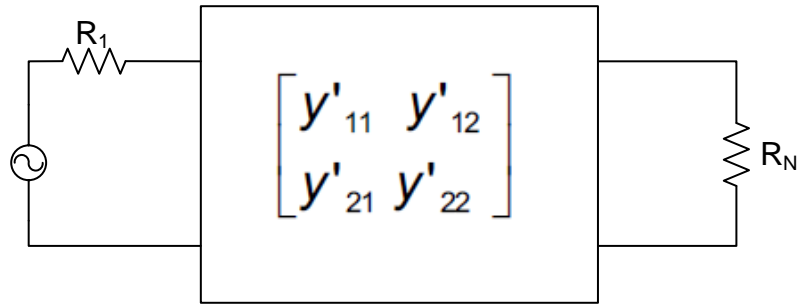
Figure 2.8: General two port lossless filter network

For N even:

$$y_{21}(s)=\frac{y_{21n}(s)}{y_d(s)}=\frac{P(s)/\varepsilon}{m_1(s)}$$

$$y_{22}(s)=\frac{y_{22n}}{y_d(s)}=\frac{n_1(s)}{m_1(s)} \qquad 2.35$$

For N odd

$$y_{21}(s)=\frac{y_{21n}(s)}{y_d(s)}=\frac{P(s)/\varepsilon}{n_1(s)}$$

$$y_{22}(s)=\frac{y_{22n}}{y_d(s)}=\frac{m_1(s)}{n_1(s)} \qquad 2.36$$

Where the complex-even and complex-odd polynomial m_1 and n_1 are given by Equation 2.37 and 2.38 respectively, and e_i and f_i, $i=0,1,2,3…N$ are complex coefficients of $E(s)$ and $F(s)$.

$$m_1(s)=\text{Re}(e_0+f_0)+j\text{Im}(e_1+f_1)s+\text{Re}(e_2+f_2)s^2+… \qquad 2.37$$

$$n_1(s)=j\text{Im}(e_0+f_0)+\text{Re}(e_1+f_1)s+j\text{Im}(e_2+f_2)s^2+… \qquad 2.38$$

After determining the numerator and denominator polynomials for $y_{21}(s)$ and $y_{22}(s)$, the associated residues r_{21k} and r_{22k}, $k=1, 2, \ldots N$ of the network may be found using partial fraction expansion or equations 2.40 and 2.41 respectively, where $y_d'(s)$ denotes the differentiation of denominator polynomial $y_d(s)$ with respect to s. The purely imaginary eigenvalues λ_k of the network is found by rooting the denominator polynomial $y_d(s)$ common to both $y_{21}(s)$ and $y_{22}(s)$ as shown in Equations 2.35 and 2.36 above. The expression for the admittance matrix $[Y_N]$ for the overall network leads up to Equation 2.39 (Cameron 2003:3). The Nth degree polynomial $y_d(s)$ has purely imaginary roots equal to $j\lambda_k$.

$$[Y_N] = \begin{bmatrix} y_{11}(s) & y_{12}(s) \\ y_{21}(s) & y_{22}(s) \end{bmatrix} = \frac{1}{y_d(s)} \begin{bmatrix} y_{11n}(s) & y_{12n}(s) \\ y_{21n}(s) & y_{22n}(s) \end{bmatrix}$$

$$= j \begin{bmatrix} 0 & K_0 \\ K_0 & 0 \end{bmatrix} + \sum_{k=1}^{N} \frac{1}{(s-j\lambda_k)} \begin{bmatrix} r_{11k} & r_{12k} \\ r_{21k} & r_{22k} \end{bmatrix} \qquad \qquad 2.39$$

$$r_{21k} = \frac{y_{21n}(s)}{y_d'(s)} \bigg|_{s=j\lambda_k} \qquad \qquad 2.40$$

$$r_{22k} = \frac{y_{22n}(s)}{y_d'(s)} \bigg|_{s=j\lambda_k} \qquad \qquad 2.41$$

The real constant K_0 is equal to zero except for fully canonical case where the number of transmission zeros (n_{fz}) in the filtering function is equal to the filtering degree N. In the case of the degree of the numerator $y_{21n}(s) = jP(s)/\varepsilon$, equal to its denominator $y_d(s)$, the factor K_0 has to be extracted first to reduce $y_{21n}(s)$ in degree by one before finding its associated residue r_{21k}. The factor K_0 may be evaluated at $s=j\infty$ as illustrated in equation 2.42. When ($N-n_{fz}$) is equal to an even number it is necessary to multiply polynomial $P(s)$ by j to ensure that unitary conditions for scattering matrix is satisfied.

$$jK_0 = \frac{y_{21n}(s)}{y_d(s)} \bigg|_{s=j\infty} = \frac{jP(s)/\varepsilon}{y_d(s)} \bigg|_{s=j\infty} \qquad \qquad 2.42$$

Since the highest degree coefficient of $P(s)$ is 1 and the highest degree of coefficient of y_d has a value of $1 + 1/\varepsilon_r$ due to its building process in equations 2.37 and 2.38, the value of K_0 may alternatively be found using Equation 2.43.

$$K_0 = \frac{\varepsilon_r}{\varepsilon(\varepsilon_r+1)} \qquad \qquad 2.43$$

The new numerator polynomial $y'_{21n}(s)$ that will be of degree $N-1$ for fully canonical case may be determined using Equation 2.44 and the residue r_{21k} of $y'_{21n}(s) = y'_{21n}(s)/y_d(s)$ may be found as normal.

$$y'_{21n}(s) = y_{21n}(s) - jK_0 y_d(s) \qquad\qquad 2.44$$

Cameron (2003:3-4) added that the two port short circuit admittance parameter matrix [Y_N] for the overall network can be synthesised directly from the fully canonical transversal network. The general form of the canonical transversal array is depicted in Figure 2.9. The circuit consists of a series of N individual first degree lowpass sections connected in parallel between the source and the load terminations, but not to each other.
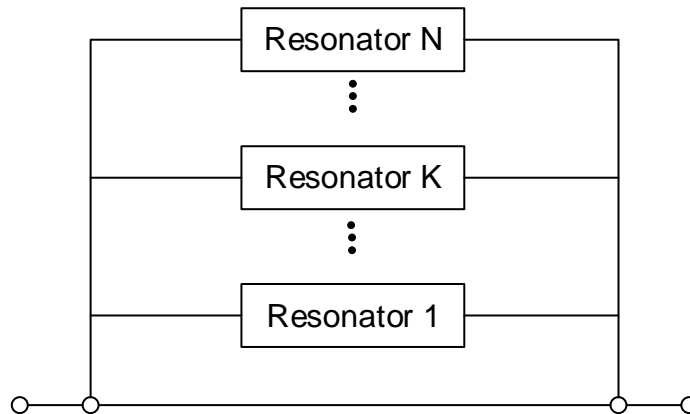
Figure 2.9: Transversal array of coupled resonator microwave filter

The equivalent circuit model for each resonator in Figure 2.9 is depicted in Figure 2.10. The [*ABCD*] transfer matrix of the cascaded elements in Figure 2.10 is derived by Cameron (2003:3-4) as in Equation 2.45 which is transformed to the individual y-parameters and adding them to form the overall admittance matrix [Y_N], given in Equation 2.46.
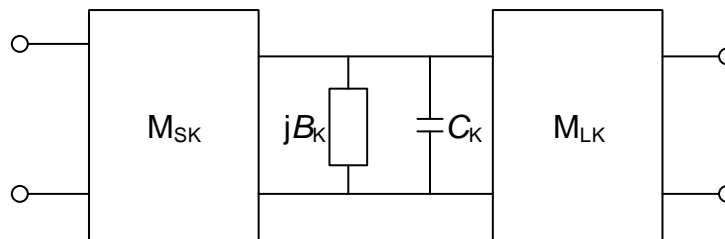
Figure 2.10: Equivalent circuit of each resonator

$$[ABCD]_k = - \begin{bmatrix} \dfrac{M_{Lk}}{M_{Sk}} & \dfrac{(sC_k+jB_k)}{M_{Sk}M_{Lk}} \\ 0 & \dfrac{M_{Sk}}{M_{Lk}} \end{bmatrix} \qquad 2.45$$

$$[Y_N]=j \begin{bmatrix} 0 & M_{SL} \\ M_{SL} & 0 \end{bmatrix} + \sum_{k=1}^{N} \frac{1}{sC_k+jB_k} \begin{bmatrix} M_{Sk}^2 & M_{Sk}M_{Lk} \\ M_{Sk}M_{Lk} & M_{Lk}^2 \end{bmatrix} \qquad 2.46$$

Comparing equations 2.46 and 2.39, it can be seen that $M_{SL}=K_0$ and the elements in the matrices on the right-hand sides in both equations can be related to each other as follows:

$$C_k=1 \qquad , \qquad B_k=M_{kk}=-\lambda_k \qquad 2.47$$

$$M_{Lk}=\sqrt{r_{22}} \quad , \quad M_{Sk}=\frac{r_{21k}}{\sqrt{r_{22k}}} \quad , \quad M_{SL}=K_0 \quad k=1,2,...N \qquad 2.48$$

The frequency-invariant susceptances $B_k=\lambda_k$ represents the self-couplings M_{11} to M_{NN}, M_{Sk} is the input couplings, M_{Lk} is the output couplings and M_{SL} is the direct source to load couplings. With all these defined, the reciprocal $N+2$ transversal coupling matrix representing the network in Figure 2.9 can now be constructed. The N input couplings M_{Sk} occupies the first row and column of the matrix from position 1 to N, and the N output couplings M_{LK} occupies the last row and column of matrix from position 1 to N as depicted in Figure 2.11. All others entries are zero.

	S	1	2	3	. .	k	. .	N-1	N	L
S	0	M_{S1}	M_{S2}	M_{S3}	. .	M_{Sk}	. .	$M_{S\,N-1}$	M_{SN}	M_{SL}
1	M_{1S}	M_{11}	0	0	0	0	0	0	0	M_{1L}
2	M_{2S}	0	M_{22}	0	0	0	0	0	0	M_{2L}
3	M_{3S}	0	0	M_{33}	0	0	0	0	0	M_{3L}
. .	. .	0	0	0	.	0	0	0	0	. .
k	M_{kS}	0	0		0	M_{kk}	0	0	0	M_{kL}
. .	. .	0	0	0	0	0	.	0	0	. .
N-1	M_{N-1S}	0	0	0	0	0	0	$M_{N-1,N-1}$	0	M_{N-1L}
N	M_{NS}	0	0	0	0	0	0	0	M_{NN}	M_{NL}
L	M_{LS}	M_{L1}	M_{L2}	M_{L3}	. .	M_{Lk}	. .	M_{LN-1}	M_{LN}	0

Figure 2.11: N+2 coupling matrix for the transversal array

For most coupled resonator technologies, the transversal topology is physically impractical or impossible to realize and it becomes necessary to transform it to a more suitable topology. There are several practical canonical forms for transformed coupling matrices of which two of the more convenient forms are the folded and arrow forms. Either of these canonical forms may be used directly if it is convenient to realize the couplings or be used as a starting point for the application of further transforms to create an alternative resonator intercoupling topology.

The procedure to reduce the transversal matrix to the folded form is described by Cameron et.al (2018: 261-268). This procedure involves applying a series of similarity transforms sometimes called rotations, which eliminate unwanted coupling matrix entries alternately right to left along rows and top to bottom down columns and working inwards toward the centre of the matrix, until the only remaining couplings are those that can be realized by filter resonators in a folded structure. The nonzero values in the coupling matrix means that in the network that it represents, coupling exists between every resonator node and every other resonator node. This is impossible to realise, therefore coupling elements are zeroed and others created with a series of rotations until a more convenient form with a minimal number of coupling is obtained. The pivot $[\,i\,,j\,]$ ($i{\neq}j$) of the resultant rotation matrix R_r means that $R_{ii}=R_{jj}=\mathrm{Cos}\ \theta_r$, $R_{ji}=-R_{ij}=\mathrm{Sin}\ \theta_r$, ($i, j{\neq}1\ or\ N$) and θ_r is the angle of rotation. When the rotations of pivot $[\,i, j]$ and angle $\theta_r\,({\neq}0)$ is applied to a coupling matrix, the elements in rows i and j, and columns i and j of the resultant matrix change in value from the corresponding element values in the original coupling matrix. The value of the kth element in the row or column i or j of the resultant matrix will change according to the formulas in equations 2.49 to 2.52, where $k\ ({\neq}i, j) = 1\ ,2\ ,3\ …N$, $c_r = \mathrm{Cos}\ \theta_r$ and $s_r= \mathrm{Sin}\ \theta_r$.

For an element in row i

$$M_{ik}^{'}=c_rM_{ik}-\ s_rM_{jk} \qquad\qquad 2.49$$

For an element in row j,

$$M_{jk}^{'}=s_rM_{ik}+\ c_rM_{jk} \qquad\qquad 2.50$$

For an element in column i,

$$M_{ki}^{'}=c_rM_{ki}-\ s_rM_{kj} \qquad\qquad 2.51$$

For an element in column j,

$$M_{kj}^{'}=s_rM_{ki}+\ c_rM_{kj} \qquad\qquad 2.52$$

The value of elements on the cross-points of pivot [M_{ii}, M_{jj}, $M_{ij}=M_{ji}$], will change according to the following formulas:

$$M_{ii}^{'}=c_r^2 M_{ii}-2s_r c_r M_{ij}+s_r^2 M_{jj}$$

$$M_{jj}^{'}=s_r^2 M_{ii}+2s_r c_r M_{ij}+c_r^2 M_{jj} \quad\quad 2.53$$

$$M_{ij}^{'}=M_{ij}(c_r^2-s_r^2)+s_r c_r(M_{ii}-M_{jj})$$

The angle formulas for annihilating specific elements in the coupling matrix with a rotation at pivot [i, j] are given below.

For the kth element in row i (M_{ik}),

$$\theta_r= \tan^{-1}\left(\frac{M_{ik}}{M_{jk}}\right) \quad\quad 2.54$$

For the kth element in row j (M_{jk}),

$$\theta_r= -\tan^{-1}\left(\frac{M_{jk}}{M_{ik}}\right) \qu\quad 2.55$$

For the kth element in column i (M_{ki}),

$$\theta_r= \tan^{-1}\left(\frac{M_{ki}}{M_{kj}}\right) \quad\quad 2.56$$

For the kth element in column j (M_{kj}),

$$\theta_r = -\tan^{-1}\left(\frac{M_{kj}}{M_{ki}}\right) \quad\quad 2.57$$

For cross-pivot (M_{ii}),

$$\theta_r= \tan^{-1}\left(\frac{M_{ij}\pm\sqrt{M_{ij}^2-M_{ii}M_{jj}}}{M_{jj}}\right) \quad\quad 2.58$$

For cross-pivot (M_{jj}),

$$\theta_r=\tan^{-1}\left(\frac{-M_{ij}\pm\sqrt{M_{ij}^2-M_{ii}M_{jj}}}{M_{ii}}\right) \quad\quad 2.59$$

For cross-pivot (M_{ij}),

$$\theta_r= \frac{1}{2}\tan^{-1}\left(\frac{2M_{ij}}{M_{jj} - M_{ii}}\right) \quad\quad 2.60$$

The matrix reduction process described above utilise the following two properties of a similarity transform:

1. The transform will affect only the elements in the rows and columns i and j of the pivot [i, j] provided its angle θ_r is not equal to zero. All others will remain at the previous values.

2. If two elements facing each other across rows and columns of the pivot are both zero before the transform, they will still be zero after transform regardless of the transform angle θ_r.

With an analytically calculated angle θ_r and the transforms applied in a certain order, coupling elements may be zeroed, and other coupling elements are created to arrive at a coupling matrix whose non-zero entries correspond to the available inter-resonator coupling elements of the intended filter structure. An example matrix of the folded form for a sixth order filter is shown in Table 2.3.

Table 2.3: An example matrix of the folded form

	S	1	2	3	4	5	6	L
S	0	M_{S1}	0	0	0	0	0	M_{SL}
1	M_{1S}	M_{11}	M_{12}	0	0	0	M_{16}	0
2	0	M_{21}	M_{22}	M_{23}	0	M_{25}	0	0
3	0	0	M_{32}	M_{33}	M_{34}	0	0	0
4	0	0	0	M_{43}	M_{44}	M_{45}	0	0
5	0	0	M_{52}	0	M_{54}	M_{55}	M_{56}	0
6	0	M_{61}	0	0	0	M_{65}	M_{66}	M_{6L}
L	M_{LS}	0	0	0	0	0	M_{L6}	0

2.6 Impedance and admittance inverters

According to Matthaei et al. (1980:144), it is difficult to implement bandpass or bandstop filters because there is a big discrepancy between the values of the components in the shunt and series resonators. As the values of inductors and capacitors are only available for limited ranges, it is necessary to convert prototypes that use series resonators alternating with shunt resonators to an equivalent form that uses resonators of the same type. This can be done by using impedance (K) or admittance (J) inverters. Impedance and admittance inverters operate like a quarter-wavelength line of characteristic impedance K and characteristic admittance J, respectively. Figures 2.12(a) and 2.12(b) show impedance and admittance inverters, respectively.

$Z_{in} = K^2/Z_L$ (a) $Y_{in} = J^2/Y_L$ (b)
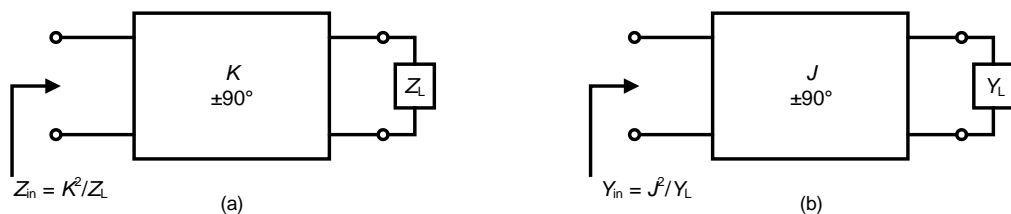
Figure 2.12: (a) Impedance inverter and (b) admittance inverter (Pozar, 2012:422)

2.6.1 Impedance inverter

The bandpass filter that uses only series resonators as in Figure 2.13 can be designed from the low-pass prototype as in Figure 2.6(a) as long as Equations 2.61 to 2.63 are used to calculate impedance inverter parameters $K_{j,j+1}$ (Matthaei et al., 1980:429-431). The components of series resonators (L_N and C_N) may be selected randomly to ease the design by taking note of Equation 2.61. Matthaei et al. (1980:431-432) also note that the desired response of the filter will depend on impedance inverter parameters as given in Equations 2.61 to 2.63.
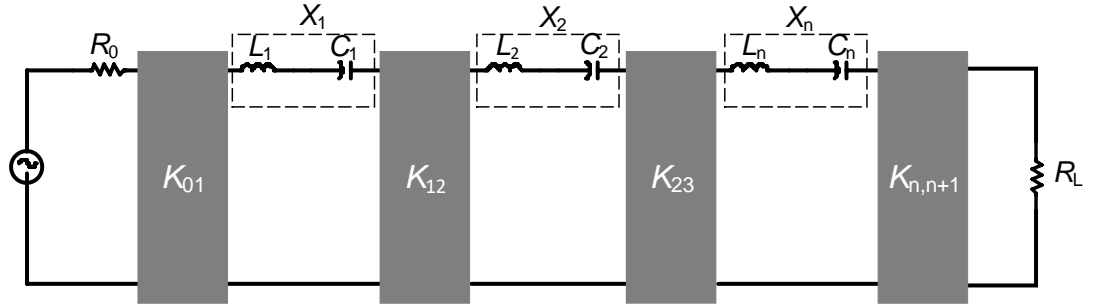
Figure 2.13: Bandpass filter using series resonators and impedance inverters

$$X_N = \omega_0 L_N = \frac{1}{\omega_0 C_N} \, [\Omega], \text{ for series resonators} \Rightarrow \omega_0 = \frac{1}{\sqrt{L_N C_N}} \qquad 2.61$$

$$K_{01} = \sqrt{\frac{R_0 X_1 \Delta}{\Omega_c g_0 g_1}} = \sqrt{\frac{R_0 L_1 BW}{\Omega_c g_0 g_1}}, K_{N,N+1} = \sqrt{\frac{R_L X_N \Delta}{\Omega_c g_N g_{N+1}}} = \sqrt{\frac{R_L L_N BW}{\Omega_c g_N g_{N+1}}} \qquad 2.62$$

$$K_{J,J+1} = \frac{\Delta}{\Omega_c} \sqrt{\frac{X_j X_{j+1}}{g_j g_{j+1}}} = \frac{BW}{\Omega_c} \sqrt{\frac{L_j L_{j+1}}{g_j g_{j+1}}}, \text{ for } 1 \le j \le N-1 \qquad 2.63$$

The external quality factor (Q_{ext}) and the internal coupling coefficient ($k_{j,j+1}$) are given by equations 2.64 and 2.65, respectively.

$$Q_{ext} = \frac{g_0 g_1 \Omega_c}{\Delta} \qquad 2.64$$

$$k_{j,j+1} = \frac{K_{j,j+1}}{\sqrt{X_J X_{J+1}}} = \frac{\Delta}{\Omega_c \sqrt{g_j g_{j+1}}}, \text{ for } 1 \le j \le N-1 \qquad 2.65$$

In the above equations, the fractional bandwidth is $\Delta = \frac{\omega_2 - \omega_1}{\omega_0}$, bandwidth is $BW = \omega_2 - \omega_1$ the centre frequency is given by $\omega_0 = \sqrt{\omega_2 \omega_1}$ and g is an element value of a low-pass filter prototype. When the normalised cut-off frequency is $\Omega_c = 1$ and $R_0 = R_L = 1 \, \Omega$,

Equations 2.62 and 2.63 above can be reduced to Equations 2.66 and 2.67 below, using Equation 2.61.

$$K_{01}=\sqrt{\frac{BWL_1}{g_0g_1}}, \; K_{n,n+1}=\sqrt{\frac{BWL_N}{g_Ng_{N+1}}} \qquad\qquad 2.66$$

$$K_{J,J+1}=BW\sqrt{\frac{L_jL_{j+1}}{g_jg_{j+1}}}, \text{ for } 1 \leq j \leq N\text{-}1 \qquad\qquad 2.67$$

The external quality factor (Q_{ext}) and internal coupling coefficient ($k_{j,j+1}$) are given by Equations 2.68 and 2.69, respectively.

$$Q_{(ext)O}=\frac{g_0g_1}{\Delta}, \; Q_{(ext)L}=\frac{g_Ng_{N+1}}{\Delta} \qquad\qquad 2.68$$

$$k_{j,j+1}=\frac{\Delta}{\sqrt{g_jg_{j+1}}}, \text{for } 1 \leq j \leq N\text{-}1 \qquad\qquad 2.69$$

Matthaei et al. (1980:450-451) gives the following design equations for K inverter coupled filter, which have shunt inductance coupling between resonators.

$$\frac{K_{01}}{Z_0}=\sqrt{\left(\frac{\pi}{2}\right)\left(\frac{\Delta_\lambda}{g_0g_1}\right)} \quad , \quad \frac{K_{n,n+1}}{Z_0}=\sqrt{\left(\frac{\pi}{2}\right)\left(\frac{\Delta_\lambda}{g_ng_{n+1}}\right)} \qquad\qquad 2.70$$

$$\frac{K_{J,J+1}}{Z_0}=\frac{\pi\Delta_\lambda}{2\sqrt{g_jg_{j+1}}} \quad , \qquad 1 \leq j \leq N\text{-}1 \qquad\qquad 2.71$$

The guide wavelength fractional bandwidth Δ_λ is given by $\Delta_\lambda=(\lambda_{g1}\text{-}\lambda_{g2})/\lambda_{g0}$, the guide wavelength at the centre frequency is $\lambda_{g0}=(\lambda_{g1}\text{-}\lambda_{g2})/2$ and λ_{g1} and λ_{g2} are the guide wavelengths at the band-edge frequencies.

2.6.2 Admittance inverter

The bandpass filter as in Figure 2.14 that uses shunt resonators and admittance inverters can be designed from the low-pass filter prototype as in Figure 2.6 by using design equations given below from Matthaei et al. (1980:433-434).
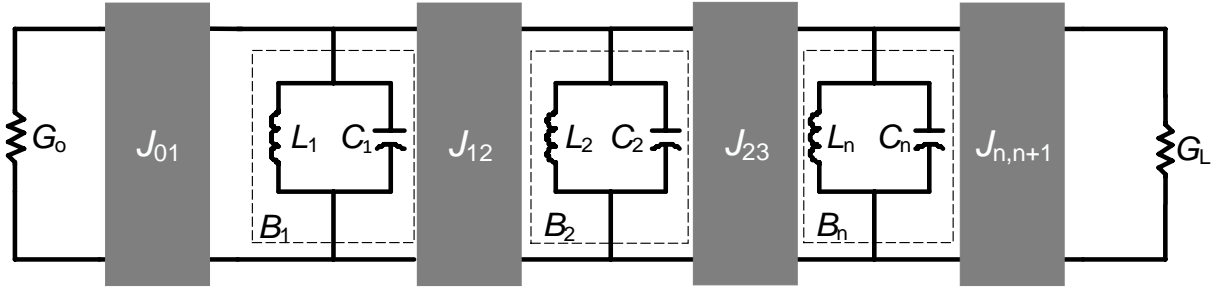
Figure 2.14: Bandpass filter using shunt resonators and admittance inverters

$$B_N = \omega_0 C_N = \frac{1}{\omega_0 L_N}[S], \text{ for shunt resonators} \Rightarrow \omega_0 = \frac{1}{\sqrt{L_N C_N}} \qquad 2.72$$

$$J_{01} = \sqrt{\frac{G_0 B_1 \Delta}{\Omega_c g_0 g_1}} = \sqrt{\frac{G_0 C_1 BW}{\Omega_c g_0 g_1}}, J_{N,N+1} = \sqrt{\frac{G_L B_N \Delta}{\Omega_c g_N g_{N+1}}} = \sqrt{\frac{G_L C_N BW}{\Omega_c g_N g_{N+1}}} \qquad 2.73$$

$$J_{J,J+1} = \frac{\Delta}{\Omega_c}\sqrt{\frac{B_j B_{j+1}}{g_j g_{j+1}}} = \frac{BW}{\Omega_C}\sqrt{\frac{C_j C_{j+1}}{g_j g_{j+1}}}, \text{for } 1 \leq j \leq N\text{-}1 \qquad 2.74$$

The external quality factor (Q_{ext}) and internal coupling coefficient ($k_{j,j+1}$) are given by Equations 2.75 and 2.76 respectively.

$$Q_{(ext)O} = \frac{g_0 g_1 \Omega_c}{\Delta}, Q_{(ext)L} = \frac{g_N g_{N+1} \Omega_c}{\Delta} \qquad 2.75$$

$$k_{j,j+1} = \frac{J_{j,j+1}}{\sqrt{B_J B_{J+1}}} = \frac{\Delta}{\Omega_c \sqrt{g_j g_{j+1}}}, \text{for } 1 \leq j \leq N\text{-}1 \qquad 2.76$$

The fractional bandwidth is given by $\Delta = \frac{\omega_2 - \omega_1}{\omega_0}$, the centre frequency is given by $\omega_0 = \sqrt{\omega_2 \omega_1}$ and bandwidth is $BW = \omega_2 - \omega_1$.

When the normalised cut-off frequency is $\Omega_c = 1$ and $G_0 = G_L = 1\ \Omega^{-1}$, equations 2.73 and 2.74 can be reduced to equations 2.77 and 2.78 below, using Equation 2.72.

$$J_{01} = \sqrt{\frac{C_1 BW}{g_0 g_1}}, J_{N,N+1} = \sqrt{\frac{C_N BW}{g_N g_{N+1}}} \qquad 2.77$$

$$J_{J,J+1} = BW\sqrt{\frac{C_j C_{j+1}}{g_j g_{j+1}}}, \text{for } 1 \leq j \leq N\text{-}1 \qquad 2.78$$

The external quality factor (Q_{ext}) and internal coupling coefficient ($k_{j,j+1}$) are given by Equations 2.79 and 2.80 respectively.

$$Q_{(ext)O}=\frac{g_0 g_1}{\Delta}, Q_{(ext)L}=\frac{g_N g_{N+1}}{\Delta} \qquad\qquad 2.79$$

$$k_{j,j+1}=\frac{\Delta}{\sqrt{g_j g_{j+1}}}, \text{ for } 1 \leq j \leq N\text{-}1 \qquad\qquad 2.80$$

The design equations for J inverter coupled filters which have series capacitance coupling between resonators are given by Matthaei et al. (1980:440-441) as follows:

$$\frac{J_{01}}{Y_0}=\sqrt{\left(\frac{\pi}{2}\right)\left(\frac{\Delta_\lambda}{g_0 g_1}\right)} \quad , \quad \frac{J_{n,n+1}}{Y_0}=\sqrt{\left(\frac{\pi}{2}\right)\left(\frac{\Delta_\lambda}{g_n g_{n+1}}\right)} \qquad 2.81$$

$$\frac{J_{J,J+1}}{Y_0}=\frac{\pi \Delta_\lambda}{2\sqrt{g_j g_{j+1}}} \quad , \qquad 1 \leq j \leq N\text{-}1$$

2.82

The guide wavelength fractional bandwidth Δ_λ is given by $\Delta_\lambda=(\lambda_{g1}-\lambda_{g2})/\lambda_{g0}$, the guide wavelength at the centre frequency is $\lambda_{g0}=(\lambda_{g1}-\lambda_{g2})/2$ and λ_{g1} and λg2 are the guide wavelengths at the band-edge frequencies.

In the above equations, it has been noted that the admittance and impedance inverters lead to the identical equations to calculate the external quality factor (Q_{ext}) and internal coupling coefficient ($k_{j,j+1}$).

Martin and Ness (1999:87) state that there is another way, known as coupling bandwidths (CBWs), that can be used to express the admittance or impedance inverter values. Coupling bandwidths can be used to eliminate either the inductive or capacitive elements in the low-pass prototype and have the advantage of being measured directly in the filter using a Vector Network Analyser (Martin & Ness, 1999:87-89). The coupling bandwidth for bandpass filters can be calculated from the low-pass prototype *g* values using the following equations from Martin and Ness (1999:87-88). The normalised external coupling and internal coupling is given by equations 2.83 and 284, respectively.

$$M_{S1}=\frac{1}{\sqrt{g_0 g_1}}, M_{NL}=\frac{1}{\sqrt{g_N g_{N+1}}} \qquad\qquad 2.83$$

$$M_{i,i+1}=\frac{1}{\sqrt{g_i g_{i+1}}}, \text{ for } 1 \leq i \leq N\text{ -}1 \qquad\qquad 2.84$$

The coupling bandwidth for both external coupling and internal coupling is given by equations 2.85 and 2.86, respectively.

$$K_{S1}=K_{0,1}=M_{S1}^2 BW \text{ and } K_{NL}=K_{N,N+1}=M_{NL}^2 BW \qquad 2.85$$

$$K_{i,j}=M_{i,j}BW \qquad 2.86$$

Ness (1998:343-351) has presented another technique which uses group delay of the reflection coefficient to design and tune coupled-resonator filters. The technique extends the theory of filter design using low-pass prototypes and low-pass to bandpass transformation to include the group delay of the input reflected signal. The derivation of equations that relate the group delay at the centre frequency to the low-pass prototype g values and the coupling parameters is also presented in the paper. The group delay of the reflection coefficient, which is the time taken for energy to get in and out of the coupled resonators, is defined by equation 2.87, where ϕ is the phase of S_{11} and ω is the angular frequency.

$$\Gamma_d(\omega) = -\frac{\partial\phi}{\partial\omega} \qquad 2.87$$

Using the standard low-pass to bandpass transformation given in equation 2.88, where ω^1 is the angular frequency of the low-pass prototype, ω_0 is the centre frequency of the bandpass filter, ω_1 and ω_2 are the lower edge and upper edge of the bandpass filter, respectively. Then Equation 2.87 is rewritten as in Equation 2.89.

$$\omega^1 \rightarrow \frac{\omega_0}{\omega_2 - \omega_1}\left(\frac{\omega}{\omega_0} - \frac{\omega_0}{\omega}\right) \qquad 2.88$$

$$\Gamma_d(\omega) = -\frac{\partial\phi}{\partial\omega^1}\left(\frac{\partial\omega^1}{\partial\omega}\right) = -\frac{\omega^2 + \omega_0^2}{\omega^2(\omega_2 - \omega_1)}\left(\frac{\partial\phi}{\partial\omega^1}\right) \qquad 2.89$$

The table below shows group delay equations and phase of the reflection signal as derived by Ness (1998:343-346).

Table 2.4: Group delay values at ω_0 in term of low-pass prototype and inverter coupled filter (Ness, 1998: 345)

N	Low-pass prototype	Inverter coupled filter $\left(\Delta=\dfrac{\omega_2-\omega_1}{\omega_0}\right)$	Phase
1	$\Gamma_{d1}=\dfrac{4g_0g_1}{\omega_2-\omega_1}$	$\Gamma_{d1}=\dfrac{4Q_e}{\omega_0};\quad Q_e=\dfrac{g_0g_1}{\Delta}$	$\phi\to\pm180^0$
2	$\Gamma_{d2}=\dfrac{4g_2}{g_0(\omega_2-\omega_1)}$	$\Gamma_{d2}=\dfrac{4}{\omega_0Q_ek_{12}^2};\quad k_{12}=\dfrac{\Delta}{\sqrt{g_1g_2}}$	$\phi\to0$
3	$\Gamma_{d3}=\dfrac{4g_0(g_1+g_3)}{\omega_2-\omega_1}$	$\Gamma_{d3}=\Gamma_{d1}+\dfrac{4Q_ek_{12}^2}{\omega_0k_{23}^2};\quad k_{23}=\dfrac{\Delta}{\sqrt{g_2g_3}}$	$\phi\to\pm180^0$
4	$\Gamma_{d4}=\dfrac{4(g_2+g_4)}{g_0(\omega_2-\omega_1)}$	$\Gamma_{d4}=\Gamma_{d2}+\dfrac{4k_{23}^2}{\omega_0Q_ek_{12}^2k_{34}^2};\quad k_{34}=\dfrac{\Delta}{\sqrt{g_3g_4}}$	$\phi\to0$
5	$\Gamma_{d5}=\dfrac{4g_0(g_1+g_3+g_5)}{\omega_2-\omega_1}$	$\Gamma_{d5}=\Gamma_{d3}+\dfrac{4Q_ek_{12}^2k_{34}^2}{\omega_0k_{23}^2k_{45}^2};\quad k_{45}=\dfrac{\Delta}{\sqrt{g_4g_5}}$	$\phi\to\pm180^0$
6	$\Gamma_{d6}=\dfrac{4(g_2+g_4+g_6)}{g_0(\omega_2-\omega_1)}$	$\Gamma_{d6}=\Gamma_{d4}+\dfrac{4k_{23}^2k_{45}^2}{\omega_0Q_ek_{12}^2k_{34}^2k_{56}^2};k_{56}=\dfrac{\Delta}{\sqrt{g_5g_6}}$	$\phi\to0$

$\Gamma_{d1}(\omega_0)$ is defined as the group delay at the centre frequency ω_0, when all other elements are disconnected from g_1 in Figure 2.6. Therefore, the input impedance Z_{in} is $Z_{in}=-j/(\omega^1g_1)$ and $Z_0=g_0$.

Then the reflection coefficient S_{11} and the phase of S_{11} are given as follows:

$$S_{11}=\frac{Z_{in}-Z_0}{Z_{in}+Z_0}=\frac{\omega^1g_0g_1+j}{j-\omega^1g_0g_1}\qquad\qquad 2.90$$

$$\phi=-2\tan^{-1}\left(\frac{1}{\omega^1g_0g_1}\right)\qquad\qquad 2.91$$

Using Equations 2.89 and 2.91, $\Gamma_{d1}(\omega_0)$ is written as in Equation 2.92.

$$\Gamma_{d1}(\omega_0)=\frac{4g_0g_1}{\omega_2-\omega_1}\qquad\qquad 2.92$$

For the inverter coupled filter in Figure 2.13, the equation of $\Gamma_{d1}(\omega_0)$ can be written as follows:

$$\Gamma_{d1}(\omega_0)=\frac{4Q_e}{\omega_0}\qquad\qquad 2.93$$

This process is repeated as each element or resonator circuit is added into the network to determine the group delay values as in Table 2.4 above.

The tuning basic steps using group delay as given by Ness (1998:347) and Cameron et al. (2018:612-613) are as follows:

1. Calculate group delay value Γ_{d1}, Γ_{d2}, . . .,Γ_{dn} at the filter centre frequency in terms of the low-pass g values or coupling values (k_{ij}) for the given filter specifications.
2. Short (detune) all resonators except resonator 1 and adjust resonance frequency of resonator 1 to set the group delay to the calculated value $\Gamma_{d1}(\omega_0)$.
3. Short all resonators except resonator 1 and 2 and tune the resonance frequency of the second resonator and coupling between resonators to get a symmetric group delay response about the filter centre frequency and with the specified value $\Gamma_{d2}(\omega_0)$. To maintain symmetry, it can be necessary to readjust resonator 1, if the coupling between resonator 1 and 2 is so strong to the extent that it detunes resonator 1.
4. Progress through the filter by tuning each resonator as in step 3 to maintain group delay symmetry and to set group delay to the calculated values.
5. When the last resonator is reached and the filter output is properly terminated, observe the amplitude response of S_{11} and tune the last resonator and the output coupling to obtain the specified return loss.

2.7 Summary

At microwave frequencies, lumped components become impractical for filter design, as the lumped components are only available in a limited range of values. Lumped elements are converted into transmission lines using Richards' transformation, whereby the inductor is replaced with a short-circuit stub and the capacitor is replaced with an open stub. The shunt and series resonators in the bandpass and bandstop filters give impractical component values, thus J and K inverters are used to convert series and shunt resonators to resonators of the same type. The recursive technique shows that with transmission zeros and the return loss in the passband given, the characteristic polynomials can be analytically evaluated. The transversal topology is impossible to realise and it becomes necessary to transform it to a more suitable topology. With a series of similarity transforms applied in a certain order, coupling elements are zeroed and other couplings are created to arrive at a coupling matrix that correspond to the available inter-resonator coupling element of the intended filter structure.

CHAPTER 3. TECHNICAL STUDY OF WAVEGUIDES AND RESONATORS

3.1   Introduction

The basic filter theory was presented in the previous chapter. This chapter covers the study of waveguides, concentrating more on rectangular waveguides, since an SIW has similar propagating modes to a rectangular waveguide. The chapter begins by defining waveguides and explains types of mode propagation in the waveguide. It further addresses the requirements for propagation to occur in the waveguide, and discusses the properties of Transverse Electric (TE) and Transverse Magnetic (TM) modes, ending by presenting the characteristics of the cavity resonator.

3.2   Waveguides

The waveguide is a single metallic conductor usually in the shape of a rectangular box or hollow cylinder as shown in Figure 3.1, which directs the propagation of an electromagnetic wave in a particular direction by confining the energy (Connor, 1986:8). Owing to its single conductor, only TE and TM modes can propagate, not Transverse Electromagnetic (TEM) waves. According to Connor (1986:8), rectangular waveguides are mostly used because they have lower losses compared to circular waveguides. The electric and magnetic fields in the waveguide are perpendicular to each other and frequencies below the cut-off frequency cannot propagate, thus it behaves like a high-pass filter (Srivastava & Gupta, 2006:221). The cut-off frequency of the waveguide is defined by its dimension, as illustrated in Equation 3.3. Gowri (2008:41) notes that the waveguide can be analysed by defining wave equation, boundary conditions and resultant equations in the form of partial differential equations.
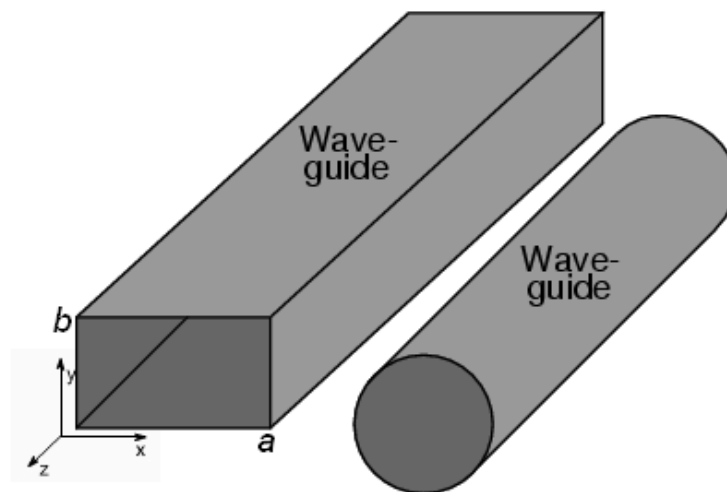
Figure 3.1: Rectangular and circular waveguides

3.3   Rectangular waveguide

The rectangular waveguide is a metallic pipe with a rectangular cross-section that is usually filled with air (Gowri, 2008:41). The electromagnetic waves travelling in the z-direction bounce from wall to wall of the rectangular waveguide shown in Figure 3.1, resulting in the H and E fields in the direction of propagation. The EM waves are guided and confined by the conducting walls, as shown in Figure 3.2. When the waves are propagating, the wavenumber (k) reveals the longitudinal and transverse components, which are the guided wavenumber (k_g) and cut-off wavenumber (k_c) respectively, as shown in Figure 3.2 with the dispersion relation given by Equation 3.1 that corresponds to Pythagoras' theorem.
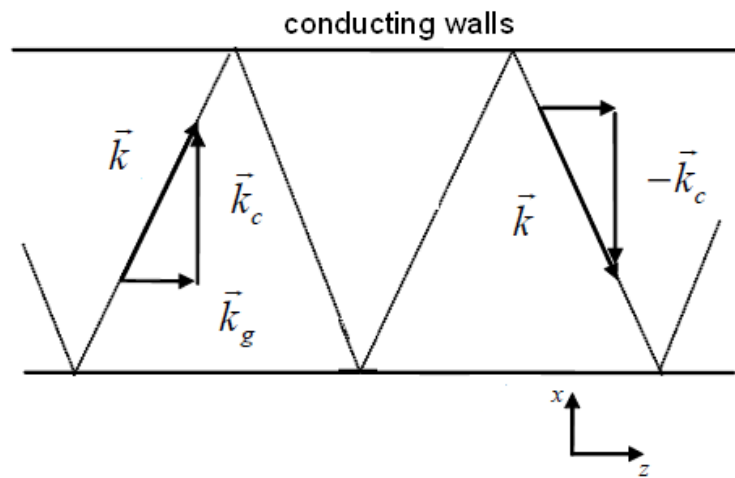
Figure 3.2: Guided waves

$$k^2 = k_c^2 + k_g^2 \qquad\qquad 3.1$$

$$k_c = \sqrt{\left(\frac{m\pi}{a}\right)^2 + \left(\frac{n\pi}{b}\right)^2} \qquad\qquad 3.2$$

Equation 3.2 shows that the cut-off wavenumber of the waveguide is dependent on its dimension, where a and b are the waveguide dimensions, with a being the longest as shown in Figure 3.1. In Equation 3.2, m is the number of half-cycle variations along the wider dimension and n is the number of half-cycle along the narrow dimension as illustrated in Figure 3.3 overleaf.
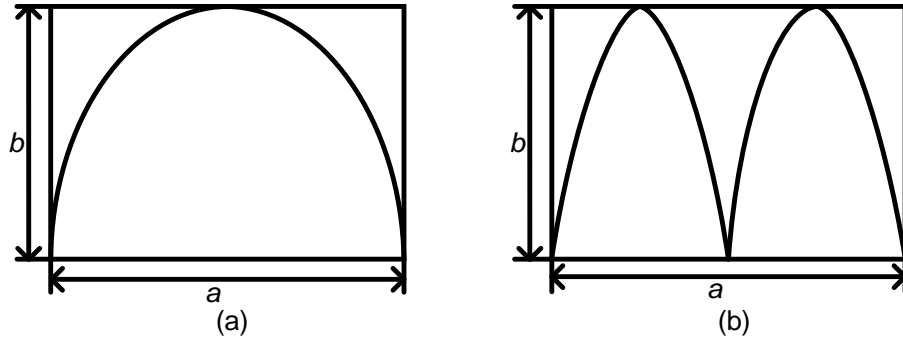
Figure 3.3: Modes in a waveguide (a) TE$_{10}$ (b) TE$_{20}$

The cut-off frequency is given by Equation 3.3, which is derived from equations 3.1 and 3.2 under the condition of the guided wavenumber equal to zero (k_g=0).

$$f_{cmn} = \frac{c}{2\pi}\sqrt{\left(\frac{m\,\pi}{a}\right)^2 + \left(\frac{n\,\pi}{b}\right)^2} \qquad 3.3$$

The guided wave number and guided wavelength are given by Equation 3.4 and 3.5, respectively. The cut-off wavelength is given by Equation 3.6.

$$k_g = \sqrt{k^2 - k_c^2} = k\sqrt{1 - \frac{k_c^2}{k^2}} = k\sqrt{1 - \left(\frac{f_c}{f}\right)^2} \qquad 3.4$$

$$\lambda_g = \frac{2\pi}{k_g} = \frac{\lambda}{\sqrt{1 - \left(\frac{\lambda}{\lambda_c}\right)^2}} = \frac{\lambda}{\sqrt{1 - \left(\frac{f_c}{f}\right)^2}} \qquad 3.5$$

$$\lambda_c = \frac{c}{f_c} = \frac{2\pi}{\sqrt{\left(\frac{m\pi}{a}\right)^2 + \left(\frac{n\pi}{b}\right)^2}} \qquad 3.6$$

Equations 3.3 and 3.6 illustrate that the cut-off frequency and cut-off wavelength are directly dependent on the dimensions of the waveguide.
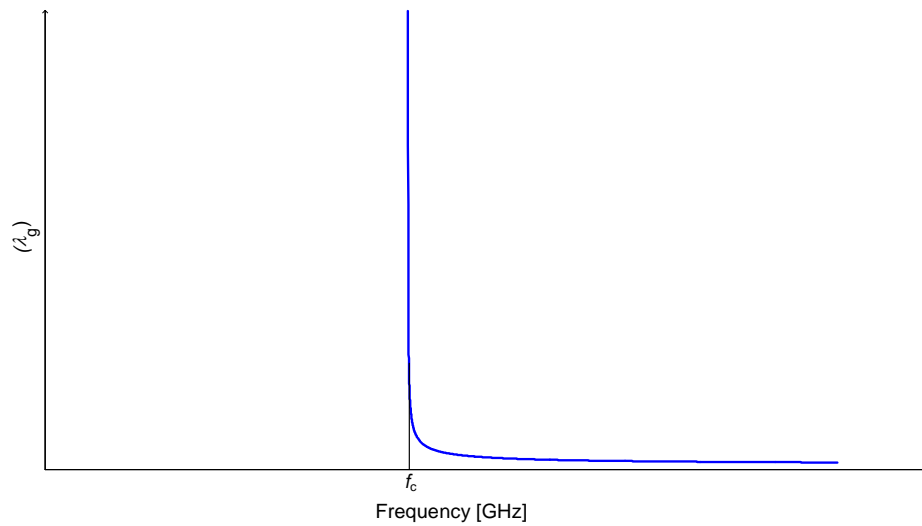
Figure 3.4: TE/TM mode guided wavelength as a function of frequency

The graph in Figure 3.4, which represents the guided wavelength as a function of frequency, is plotted in Matlab using Equation 3.5. Figure 3.4 shows that propagation will only occur when f is greater than f_c. Similarly, Equation 3.5 shows that f must be greater than f_c as the guided wavenumber needs to be a real number for the propagation to occur. When both the TE_{mn} and TM_{mn} modes have the same cut-off frequency, they are referred to as the degenerate modes (Gowri, 2008:53). TM_{m0} and TM_{0n} modes are not possible to propagate in the rectangular waveguide. The dominant mode is the one that has the lowest cut-off frequency.

Operating frequency band

Equation 3.3 can be used to determine the mode cut-off frequencies in a rectangular waveguide.

$$f_{c10} = \frac{c}{2a}, \; f_{c20} = \frac{c}{a}, \; f_{c01} = \frac{c}{2b}$$

The dimension, a, is the longest side, therefore $f_{c01} > f_{c10}$. When $b < \frac{a}{2}$ it will result in $f_{c01} > f_{c20}$, which means that f_{c01} will be higher than the other two cut-off frequencies as illustrated in Figure 3.5 below.
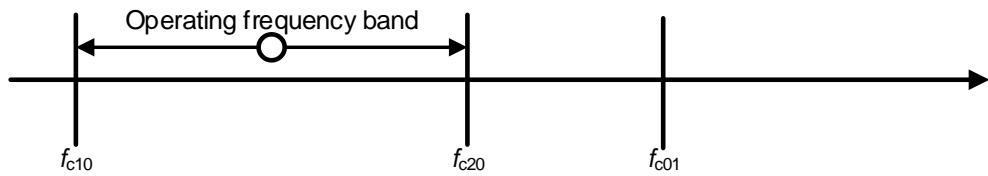
Figure 3.5: Cut-off frequencies of a waveguide when a>2b

The diagram in Figure 3.5 shows that for frequencies between f_{c10} and f_{c20}, the waveguide is monomode (dominant mode propagating alone). If $\frac{a}{2} < b < a$, then $f_{c01} < f_{c20}$, which means f_{c20} is the highest cutoff, compared with other cut-off frequencies as illustrated in Figure 3.6 below.
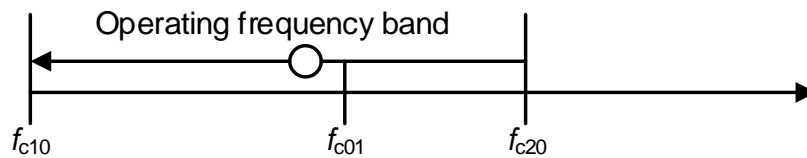
Figure 3.6: Cut-off frequencies of a waveguide when a/2<b<a

The diagram in Figure 3.6 shows that for frequencies between f_{c10} and f_{c20}, there will be two modes propagating the waveguide. The conditions for the wave to propagate in the waveguide are given by Equation 3.5, where the cut-off wavelength must be greater than the operating wavelength, or the cut-off frequency smaller than the operating frequency.

3.3.1 TE mode

The TE mode in a rectangular waveguide is characterised by the *E* field being normal to the direction of propagation. The cut-off frequency (f_c), guided wavenumber (k_g), guided wavelength (λ_g) and cut-off wavelength (λ_c) for TE modes is given by Equations 3.3, 3.4, 3.5 and 3.6, respectively. The wave impedance for TE mode is then given by Equation 3.7.

$$Z_{TE} = \frac{k}{k_g}\eta = \frac{\eta}{\sqrt{1 - \left(\frac{f_c}{f}\right)^2}} \qquad 3.7$$

The response of the wave impedance of the travelling wave for TE mode with respect to the frequency is illustrated in Figure 3.7. The graph in Figure 3.7 illustrates that when $f > f_c$, the wave carries energy and wave impedance in Equation 3.7 gives a real

number, but when $f < f_c$, the wave is evanescent and wave impedance in Equation 3.7 gives an imaginary number.
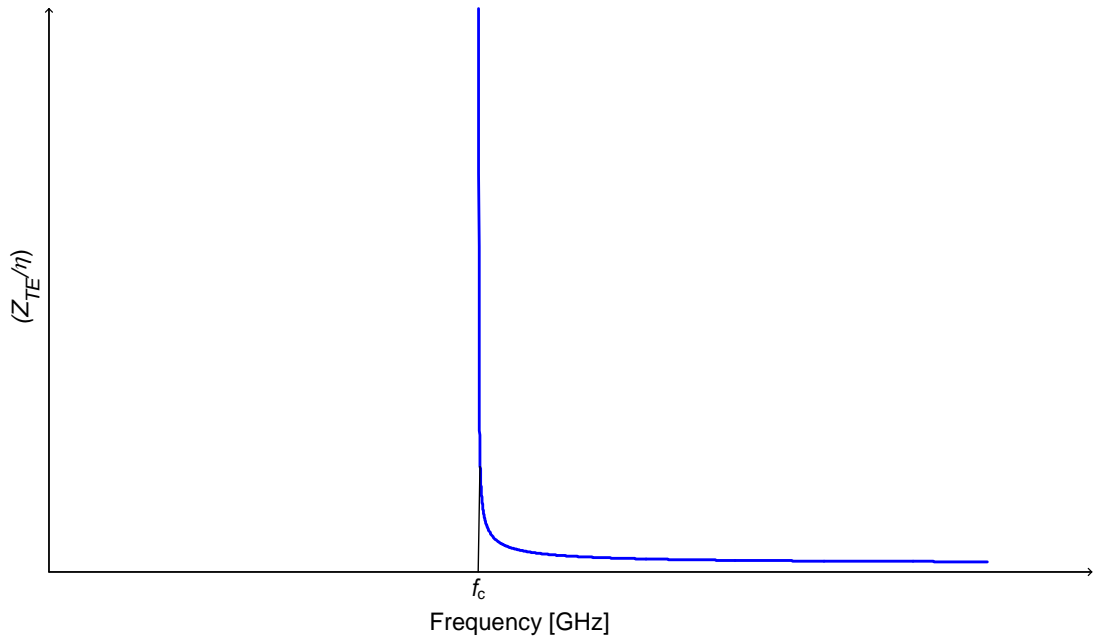
Figure 3.7: Wave impedance of the TE mode as a function of frequency

Boundary equation

In TE mode, the *B* field must be parallel to the perfect conducting walls, therefore $B_z.\vec{n} = 0$ where $\vec{n}$ is a unit vector normal to the perfect conducting walls. Therefore, the boundary condition is $\frac{\partial B_z}{\partial \vec{n}} = 0$, called the Neumann boundary condition, which means B_z must be extremal to the boundary.

3.3.2 TM mode

The TM mode is characterised by the *B* field being normal to the direction of propagation. The cut-off frequency (f_c), guided wavenumber (k_g), guided wavelength (λ_g) and cut-off wavelength (λ_c) for TM modes is given by equations 3.3, 3.4, 3.5 and 3.6, respectively. The wave impedance for TM mode is given by Equation 3.8.

$$Z_{TM} = \frac{k_g}{k}\eta = \eta\sqrt{1 - \left(\frac{f_c}{f}\right)^2} \qquad\qquad 3.8$$
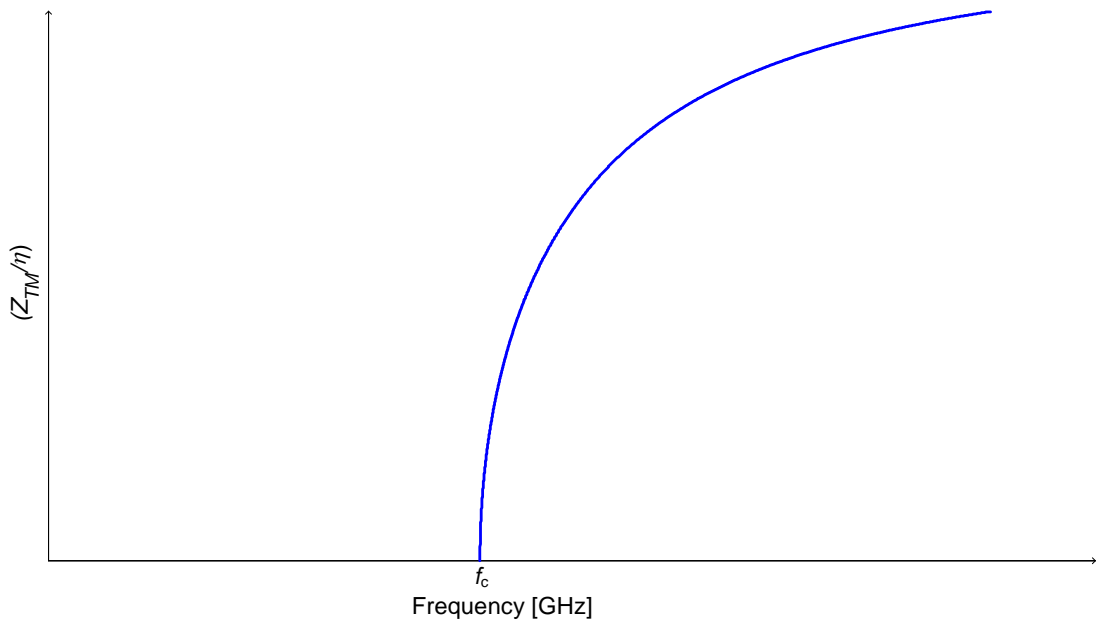
Figure 3.8: Wave impedance of the TM mode as function of frequency

Figure 3.8 above illustrates the response of the wave impedance of the travelling wave for TM mode as function of frequency. The graph in Figure 3.8 illustrates that when $f > f_c$, the wave carries energy and wave impedance in Equation 3.8 gives a real number, but when $f < f_c$, the wave is evanescent and wave impedance in Equation 3.8 gives an imaginary number.

Boundary equation

In TM mode the E field must be tangent to the perfect conducting walls, knowing $E_Z = -dV = -\vec{\nabla}V.d\vec{r}$. For the equipotential surface, $dV = 0$, therefore the boundary condition is $E_Z = 0$, called the Dirichlet boundary condition, which means E_z must be zero on the boundary.

3.4   Cavity resonator

The cavity resonator can be seen as a waveguide with both ends enclosed (Gowri 2008:112), as shown in Figure 3.9. According to Hunter (2001:209), when TE_{10} mode is propagating along z, the E field must be zero at $z = 0$ and at $z = d$. The side d of the cavity is a multiple of the half-guided wavelength ($\frac{\lambda_g}{2}$) at the frequency of operation.
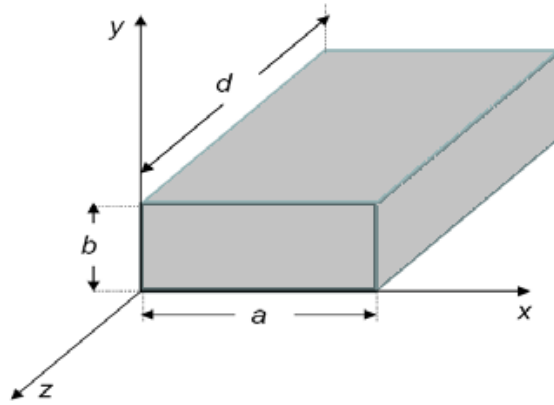
Figure 3.9: Rectangular cavity resonator.

The cut-off wavenumber and resonance frequency for a rectangular cavity are given by equations 3.9 and 3.10, respectively. For TE_{101}, the resonance frequency is given by Equation 3.11.

$$k_c = \sqrt{\left(\frac{m\pi}{a}\right)^2 + \left(\frac{n\pi}{b}\right)^2 + \left(\frac{p\pi}{d}\right)^2} \qquad 3.9$$

$$f_0 = \frac{c}{2\pi\sqrt{\varepsilon_r}} \sqrt{\left(\frac{m\pi}{a}\right)^2 + \left(\frac{n\pi}{b}\right)^2 + \left(\frac{p\pi}{d}\right)^2} \qquad 3.10$$

$$f_0 = \frac{c}{2\sqrt{\varepsilon_r}} \sqrt{\left(\frac{1}{a}\right)^2 + \left(\frac{1}{d}\right)^2} = \frac{c}{2\sqrt{\varepsilon_r}ad} \sqrt{a^2 + d^2} \qquad 3.11$$

Equations 3.10 and 3.11 state that the resonant frequency of a cavity is dependent on its dimensions. TE_{mnp} and TM_{mnp} degenerate modes as they have the same resonant frequency but different patterns. TE_{mn0} modes do not exist, but TM_{mn0} modes exist if $mn \neq 0$.

3.5   Summary

The waveguide only allows TE and TM modes to propagate, not TEM. The cut-off frequency of the waveguide is determined strictly by its dimensions; thus the number of modes that will propagate depends on the waveguide dimensions. The propagation in the waveguides only occurs when the frequency is greater than the cut-off frequency.

CHAPTER 4. TECHNICAL LITERATURE REVIEW OF SIW TECHNOLOGY

4.1   Introduction

This chapter presents a technical review of SIW technology. The chapter commences by giving an overview of the SIW, followed by a discussion on factors related to substrate selection that affect the quality of the SIW filter. The chapter outlines the design guidelines of the SIW, and compares the quality of the SIW resonators with that of various other RF resonators such as the metallic waveguide. The two methods that can also be used to excite SIW filters, which involve the transition from the transmission line (microstrip line or coplanar) to SIW, are also presented.

4.2   Substrate Integrated Waveguide

The SIW is a synthetic rectangular waveguide formed in a planar substrate with two rows of metallised via holes drilled in a dielectric substrate, sitting between two parallel metal plates as shown in Figure 4.1. They provide a low-cost and low-loss solution to planar structures on the same substrate. The performance of SIW filters is closely related to the substrate characteristics.
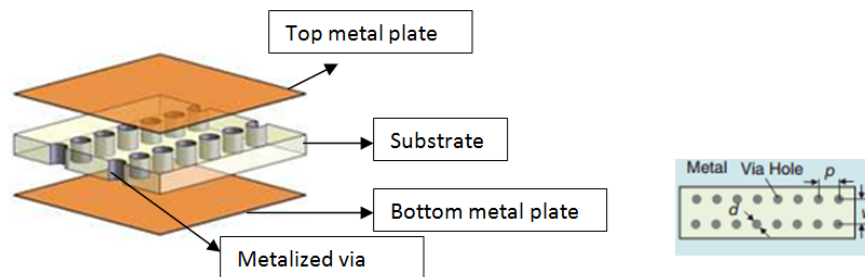
Figure 4.1: Basic substrate integrated waveguide
(Chen & Wu, 2014a:110)

The thickness of the substrate is much smaller than the SIW width. The SIW width (w), the diameter of via holes (d) and spacing between via holes (p) in Figure 4.1 describe the geometry of the SIW. The SIW structure resembles the rectangular waveguide with a series of via holes on both sides of the narrow walls. According to Xu and Wu (2005:67), the TM modes do not exist in SIW structures, since the perforated side walls will not support the longitudinal currents produced by TM modes and via holes will cause a large amount of radiation. Similarly, when the TE_{mn} modes (n not equal to zero) are excited in the SIW, via holes will present significant radiation loss due to discontinuities in the side walls. Xu and Wu (2005:67) conclude that since the via holes will not intercept the surface current produced by the propagation of the TE_{10} as the

current will flow vertically along the metallised via holes as shown in Figure 4.2, only TE$_{m0}$ modes will propagate in the SIW. The gap between via holes should be small to provide perfect shielding to avoid radiation leakage, and the electromagnetic field will be confined inside the SIW.
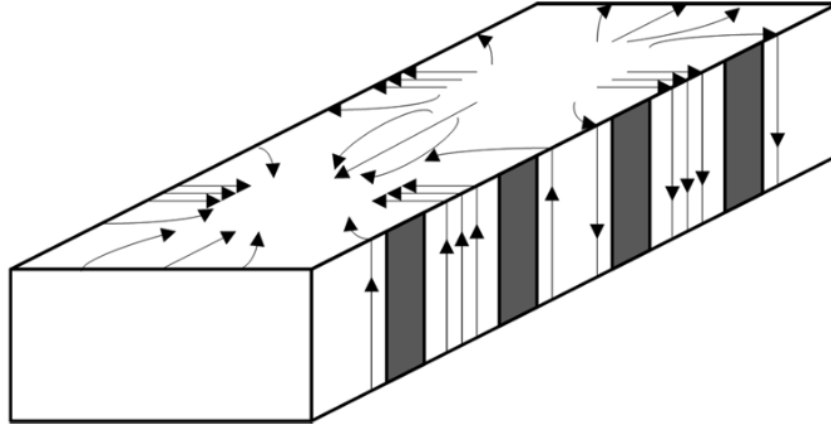
Figure 4.2: TE$_{10}$ surface current's distribution of SIW
(Xu &Wu, 2005:67).

4.3 Substrate selection

The substrate selection process is pertinent to the performance of the SIW filter. The size, insertion loss, temperature stability and power handling of an SIW filter can be directly related to the quality of the substrate used.

4.3.1 Size

In an equivalent dielectric-filled rectangular waveguide, the cut-off frequency of the TE$_{10}$ mode can be calculated using Equation 4.1, where c is the speed of light in free space and ε_r is the substrate permittivity.

$$f_c = \frac{c}{2w_{eff}\sqrt{\varepsilon_r}} \Rightarrow w_{eff} = \frac{c}{2f_c\sqrt{\varepsilon_r}} \qquad\qquad 4.1$$

The width of an SIW can be determined by using the dielectric-filled rectangular waveguide equation through the equivalent width w_{eff} as given in Equation 4.2 or 4.3 overleaf. The equivalent width of an SIW is calculated in such a manner that the SIW and its equivalent rectangular waveguide have the same cut-off frequency for the TE$_{10}$ mode. Cassivi, Perregrini, Arcioni et al. (2002:334) compared the dispersion characteristics of the SIW to those of an equivalent rectangular waveguide filled with the same dielectric material as illustrated in Figure 4.3 overleaf. They concluded that both waveguides have the same dispersion characteristics. Thus Cassivi, Perregrini, Arcioni et al. (2002:334) state that the width w (centre to centre between via holes of

both rows) of an SIW is given by Equation 4.2 below, where *d* is a diameter and *p* is a pitch between adjacent via holes.

$$w = w_{eff} + \frac{d^2}{0.95p}$$
$$\qquad 4.2$$
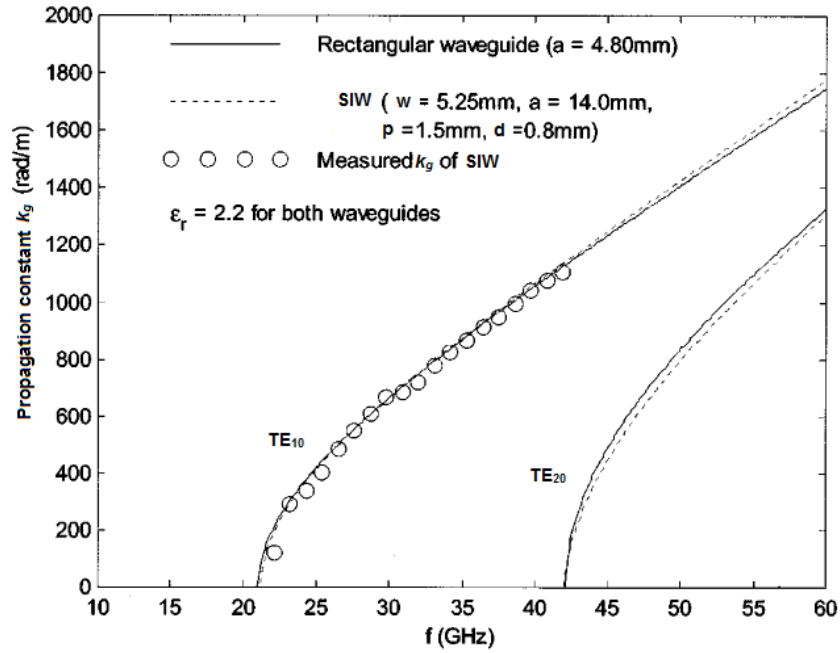
Figure 4.3: Comparison of dispersion curves of an SIW with an equivalent rectangular waveguide (Cassivi, Perregrini, Arcioni et al., 2002:334).

Equation 4.2 is valid for $p < 4d$ with a precision of ± 5% (Cassivi, Perregrini, Arcioni et al., 2002:334). Xu and Wu (2005:68) propose Equation 4.3 as a more accurate estimate, as Equation 4.2 does not include the effect of $\frac{d}{w}$ that causes an error when *d* is increased. Equation 4.3 is more accurate when $p < 3d$ and $d < \frac{w}{5}$.

$$w = w_{eff} + 1.08\frac{d^2}{p} - 0.1\frac{d^2}{w}$$
$$\qquad 4.3$$

Equation 4.1 shows that the width of an SIW is inversely proportional to the square root of a substrate permittivity. Thus, choosing a substrate with a high permittivity will lead to an SIW that will occupy less space.

4.3.2 Losses

Rectangular structures exhibit two mechanisms of losses, the conductor loss, due to the conductivity of metal walls, and dielectric loss, due to the loss tangent of the dielectric material. Bozzi et al. (2008a:3153) state that in SIW structures, there are three

mechanisms of losses, namely, conduction loss, dielectric loss and radiation leakage loss through the gaps between via holes. According to Deslandes and Wu (2006:2523), the leakage loss is negligible when the design rules given in section 4.3.5 (page 56 to 57), under SIW design guidelines, are satisfied at the operating frequency, resulting in the other two being the major contributors of losses in SIW filters.

In a rectangular waveguide, attenuation due to conductor loss for the TE_{10} mode is given by Equation 4.4, where R_s is the surface resistivity of the conductor, h is the height, and σ is the conductivity of the metal. Pozar (2012:101-102) notes that dielectric loss is given by Equation 4.6, with loss tangent given by $\tan\delta = \frac{\varepsilon_{im}}{\varepsilon_{real}}$.

$$\alpha_c = \frac{R_S}{w_{eff}^3 h k_g k \eta}\left(2h\pi^2 + w_{eff}^3 k^2\right) \ [Np/m] \qquad\qquad 4.4$$

$$R_s = \sqrt{\frac{\omega\mu_0}{2\sigma}} = \sqrt{\frac{\pi f \mu_0}{\sigma}} \qquad\qquad 4.5$$

$$\alpha_d = \frac{k^2 \tan\delta}{2k_g} \qquad\qquad 4.6$$

Insertion loss in SIW filters can be caused by the dielectric loss and conductor loss. Since a rectangular waveguide can be used as an equivalent to SIW, Equation 4.7 can be deduced from Equation 4.4 for an SIW filter using $k_g = \sqrt{k^2 - k_c^2}$ and $k_c = \frac{\pi}{a}$ for TE_{10}, where a is width w_{eff} (Kumari & Srivastava, 2013:54).

$$\alpha_c = \frac{R_S}{w_{eff}\eta\sqrt{1-\frac{k_c^2}{k^2}}}\left(\frac{2k_c^2}{k^2} + \frac{w_{eff}}{h}\right) \ [Np/m] \qquad\qquad 4.7$$

Conductor loss in the SIW is due to the conductivity of the top and bottom metal walls as well as metallic via holes. Equation 4.7 shows that the attenuation due to conductor loss is inversely proportional to the substrate thickness. Increasing substrate thickness will reduce the magnitude of the electric current flowing in the top and bottom metal walls of the SIW, thus reducing the power dissipated by the Joule effect. Therefore, the conductor loss can be reduced in the SIW by increasing substrate thickness.

Using Equation 4.5 and $\eta = \sqrt{\frac{\mu_0}{\varepsilon_0 \varepsilon_r}}$, Equation 4.7 of the attenuation constant α_c can be deduced to Equation 4.8 below.

$$\alpha_c = \frac{\sqrt{\pi f \varepsilon_0 \varepsilon_r}}{w_{eff}\sqrt{\sigma}\sqrt{1 - \frac{f_c^2}{f^2}}}\left(\frac{2f_c^2}{f^2} + \frac{w_{eff}}{h}\right) \ [Np/m] \qquad\qquad 4.8$$

Equation 4.8 above shows that the attenuation due to conductor loss is directly proportional to $\sqrt{f}$. For the Joule effect $\alpha_c \sim R_s \sim \sqrt{f}$ as shown by Equations 4.7 and 4.8. Bozzi et al. (2009:398) established that the dominant source of loss was dielectric loss, and there was no need to try to reduce conductor loss contribution by changing via holes and spacing between via holes.

According to Bozzi et al. (2009:395), SIW and rectangular waveguides have similar field propagation; therefore Equation 4.6 of the rectangular waveguide can be used to determine attenuation due to dielectric loss (α_d) of the fundamental mode in SIW. Equation 4.6 can be rewritten as Equation 4.9 for SIW.

$$\alpha_d = \frac{k^2 \tan\delta}{2k\sqrt{1 - \frac{k_c^2}{k^2}}} = \frac{\pi f \sqrt{\varepsilon_r}}{c\sqrt{1 - \frac{f_c^2}{f^2}}}\tan\delta \qquad\qquad 4.9$$

Equation 4.9 above shows that the attenuation due to dielectric loss is proportional to frequency (*f*) and to the loss tangent. Figure 4.4 illustrates the behaviour of the attenuation due to dielectric loss, and attenuation due to conductor loss, as function of frequency.
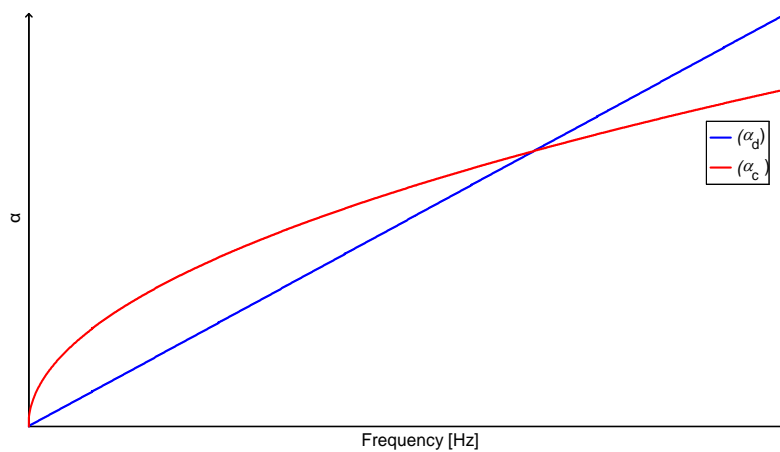
Figure 4.4: Attenuation response to the frequency

According to Deslandes and Wu (2006:2519), when the space between via holes increases, the field propagating in the SIW may no longer be confined within the waveguide, as some of the energy may propagate outside through spaces between

vias, resulting in radiation leakage loss. Deslandes and Wu (2006:2523) conclude that the space between via holes must be less than twice the diameter of the via holes in order to minimise radiation leakage loss.

Bozzi et al. (2008a:3157-3158) conducted a parametric investigation of losses in SIW interconnected with a substrate thickness $h = 0.254$ mm, $d = 0.635$ mm, $p = 1.016$ mm. The results from Bozzi et al. (2008a:3158) are shown on page 50 to 51 in figures 4.5, 4.6 and 4.7. Figure 4.5 shows that an increase of substrate thickness will reduce conductor loss, and the substrate thickness has no effect on dielectric loss. Figure 4.6 illustrates that when the diameter is made smaller while the spacing between vias is kept constant, this causes an increase in radiation loss. When the diameter increases, the attenuation due to radiation leakage decreases to negligible levels. Varying of the diameter does not have a significant effect on conductor loss or dielectric loss, thus radiation leakage is the major contributor to total loss when varying the diameter. The increase of spacing between vias while the diameter is kept constant will also give an increase in radiation leakage loss as shown in Figure 4.7. Varying the spacing between vias with the diameter kept constant contributes less dielectric and conductor loss compared with radiation leakage loss.

In Figure 4.6, the radiation leakage loss is low and constant for $d > 0.5$ mm, while the spacing is kept unchanged at $p = 1.016$ mm; however, when $d < 0.5$ mm, radiation loss increases significantly. Similarly, in Figure 4.7, the radiation loss is low and constant for p < 1.5 mm, but for larger values of p, the radiation loss increases. Thus figures 4.6 and 4.7 show that radiation loss is practically negligible for low values of the ratio $\frac{p}{d}$ and the radiation leakage loss increases when $\frac{p}{d} > 2$, as reported by Deslandes and Wu (2006:2523) using Equation 4.13 on page 56.
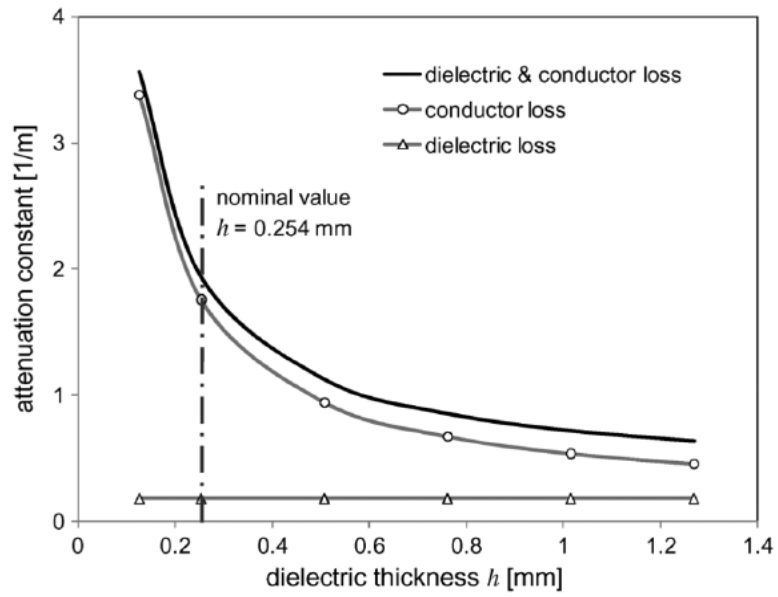
**Figure 4.5: Attenuation constant vs dielectric thickness
(Bozzi et al., 2008a:3158)**
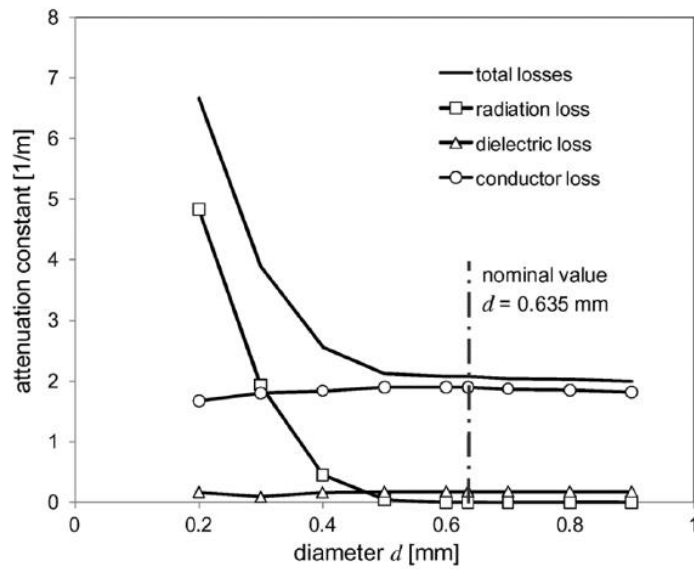
**Figure 4.6: Attenuation constant vs diameter
(Bozzi et al., 2008a:3158)**
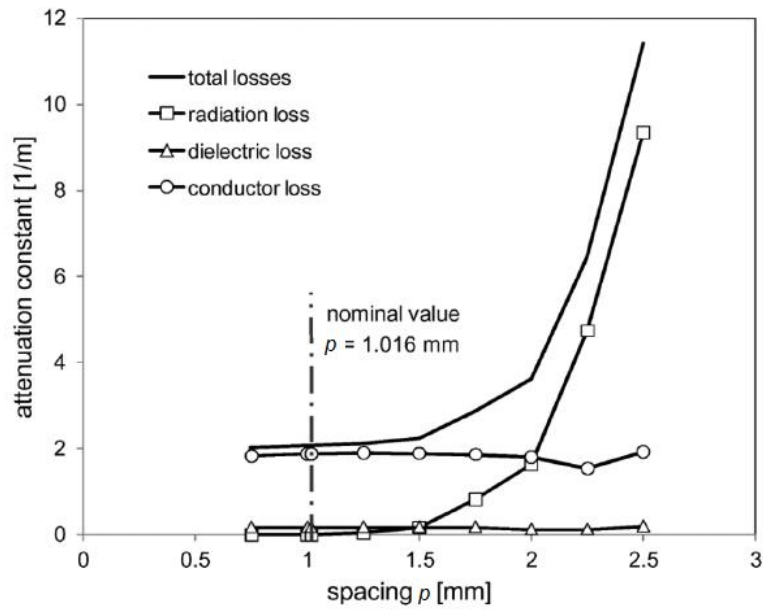
**Figure 4.7: Attenuation constant vs spacing
(Bozzi et al., 2008a:3158)**

Bozzi et al. (2008b:517) performed a comparison of losses in SIW, microstrip and coplanar waveguide built on the same substrate with the same thickness (h=0.245 mm). Microstrip and coplanar waveguide were dimensioned in order to exhibit a characteristic impedance of 50 Ω with the same width (w =0.24 mm). The SIW exhibits high losses close to the cut-off frequency and low losses as the frequency increases, as illustrated in Figure 4.8. Thus SIW has better performance in terms of losses in the upper part of the operation frequency band as illustrated in Figure 4.8 below.
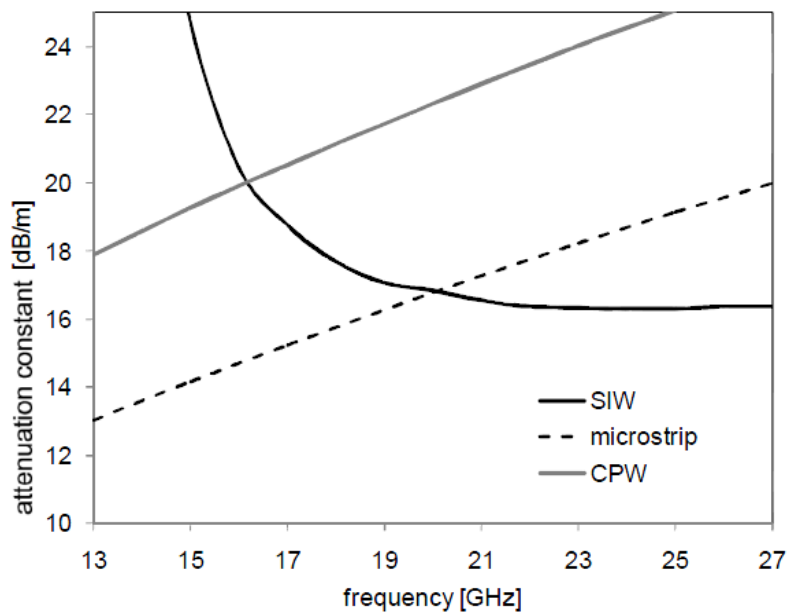
**Figure 4.8: Comparison of the attenuation in SIW, microstrip and coplanar waveguide
(Bozzi et al., 2008b:518)**

51

4.3.3 Thermal stability

Temperature stability is one of the essential criteria of a high-quality SIW filter. According to Chen and Wu (2014b:78), the temperature coefficient of the TE_{101} mode at resonant frequency f_0 can be calculated using Equation 4.10, where ε_r is the substrate permittivity, T is the temperature, and α is the thermal expansion coefficient along the width.

$$\tau_f(TE_{101}) = \frac{1}{f_o}\frac{\Delta f}{\Delta T}\frac{1}{10^{-6}}\left[\text{ppm}/\,^0 C\right] = -\left(\frac{1}{2}\frac{1}{\varepsilon_r}\frac{\Delta\varepsilon_r}{\Delta T} + \frac{1}{\alpha}\frac{\Delta\alpha}{\Delta T}\right) \qquad 4.10$$

Temperature variation will lead to the change of substrate permittivity and dimensions of an SIW filter. From Equation 4.1, the cut-off frequency is dependent on the dimensions of the SIW filter as well as the substrate permittivity. This temperature variation can lead to the cut-off frequency of the SIW filter to shift, as the dimensions and substrate permittivity are modified. The coefficients of thermal expansion (CTE) along the x-axis and y-axis are usually the same. When the CTE (τ_{xy}) in x and y are almost 50% less than the temperature coefficient of the permittivity (τ_ε), and have an opposite sign as given by Equation 4.11, it can reduce temperature coefficients of a resonant frequency (Djerafi et al., 2012a:2449).

$$\tau_\varepsilon \approx -2\tau_x \qquad 4.11$$

An SIW filter fabricated with the substrate having the material properties that meet the requirements of Equation 4.11 can have a good thermal stability. Djerafi et al. (2012a:2449-2450) conducted a temperature analysis over a temperature range from −40 to 80 degree Celsius on three SIW cavities designed to operate at the same frequency and fabricated with the materials in Table 4.1 overleaf. The temperature coefficients calculated using Equation 4.10 of the materials in Table 4.1 are plotted by Djerafi et al. (2012a:2450) as in Figure 4.9. The substrate material TMM10 has thermal characteristics that meet the requirements of Equation 4.11, that is, the temperature coefficient of the permittivity is twice the CTE of x and y with an opposite sign.

Table 4.1: Material properties (Djerafi et al. (2012a:2449)

Material	Relative Dielectric Constant (ε_r)	Loss tangent	Temperature Coefficient of Permittivity (τ_ε) (ppm/°C)	Coefficient of thermal expansion (τ_{xyz}) (ppm/°C) *x/y/z*
6010	10.2 ± 0.25	0.0023	−425	24/24/47
6002	2.94 ± 0.04	0.0012	+12	16/16/24
TMM10	9.20± 0.230	0.0022	−38	21/21/20
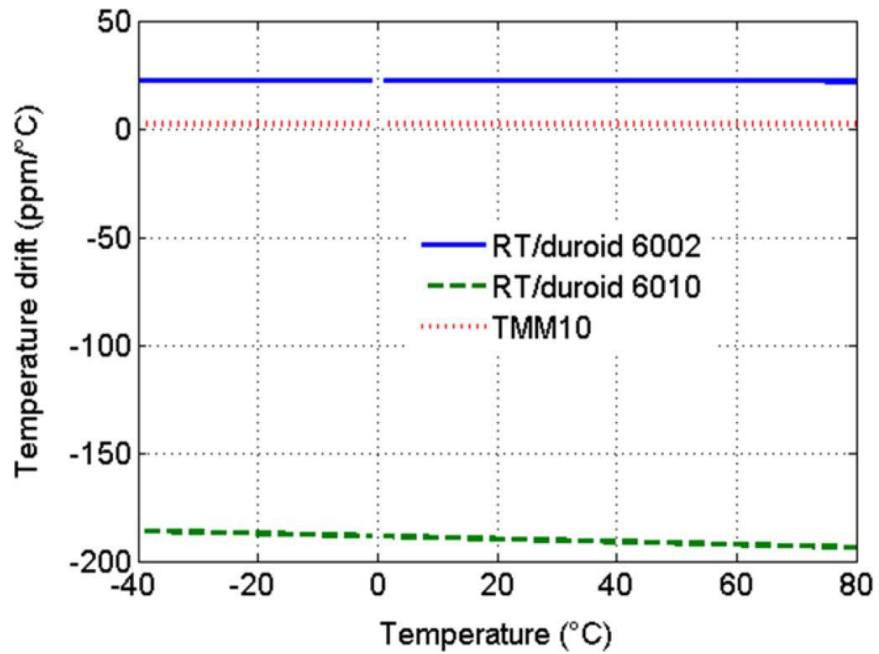
Figure 4.9: Calculated temperature coefficient of frequency versus temperature (Djerafi et al., 2012a:2450)

The measured reflection coefficients of the three cavities fabricated with materials in Table 4.1 are presented by Djerafi et al.(2012a:2451) in Figure 4.10 to Figure 4.12.
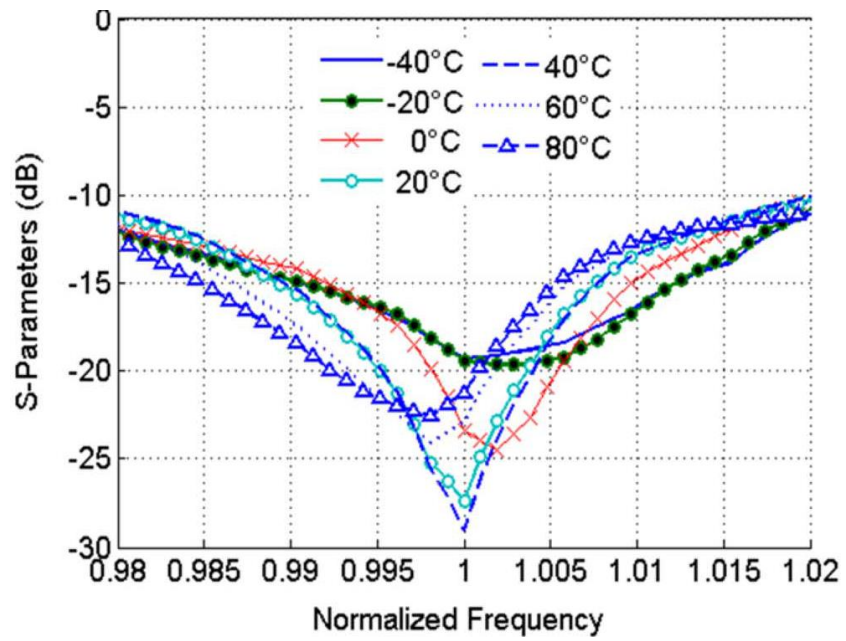
**Figure 4.10: Reflection coefficients for RT/Duroid 6002 cavity
(Djerafi et al., 2012a:2451)**
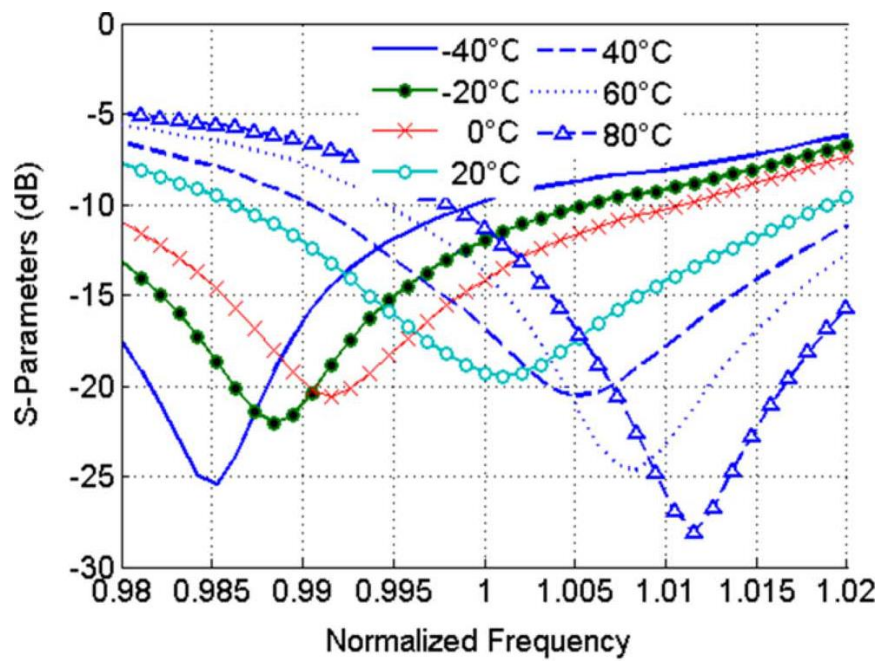
**Figure 4.11: Reflection coefficients for RT/Duroid 6010 cavity
(Djerafi et al., 2012a:2451)**
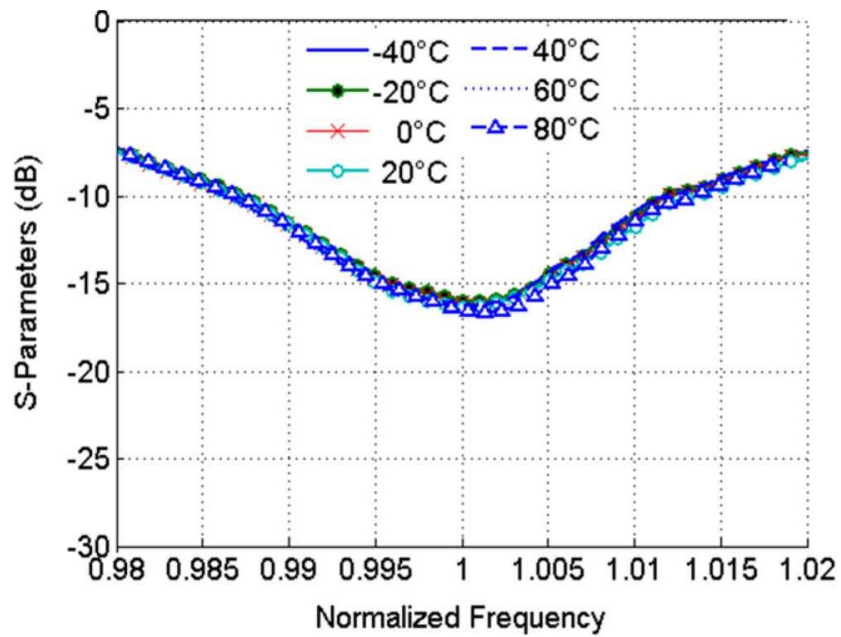
Figure 4.12: Reflection coefficients for TMM10 cavity
(Djerafi et al., 2012a:2451)

The figures above illustrate that TMM10 presents good temperature stability compared to RT/Duroid 6010 and RT/Duroid 6002 as predicted by Figure 4.9. For a high-quality SIW filter design, it is important to conduct a thermal stability analysis.

4.3.4 Power handling

The amount of power dissipated in transmission will result in an increase in temperature. The rise in temperature due to the power dissipated will also lead to changes in material properties like substrate permittivity, thus resulting in frequency shift in the SIW filter. The average power-handling capacity of an SIW filter is determined by the choice of material, its bandwidth and geometry. For high power filters, the power-handling capacity is an important factor in the design of a quality filter. That is why the average power handling capacity should be scrutinised. An ideal substrate would be one with a small thermal coefficient of permittivity, large thermal conductivity, and low dimensional coefficient of thermal expansion. Chen and Wu (2014b:77) conclude that the substrate Rogers RT/Duroid 6002 has the best overall properties compared with the other two substrates shown in Table 4.2 overleaf, and it may be the suitable substrate for SIW filter design.

Table 4.2: Properties of a typical substrate material (Chen &Wu, 2014b: 77)

Properties	Rogers RT/Duroid 5880	Rogers RT/Duroid 6002	Rogers RO 3003
Permittivity	2.20±0.02	2.94±0.04	3.00±0.04
Dielectric loss	0.0009	0.0012	0.0013
Thermal coefficient of permittivity (ppm/°C)	-125	12	13
Coefficient of thermal expansion ($x/y/z$, ppm/°C)	31/48/237	16/16/24	17/17/24
Thermal conductivity (W/m/k)	0.22	0.6	0.5
*IL(dB)/inch	0.082	0.101	0.104
* Pin (W)	81	164	131

*Program Rogers MWI, Microstrip, Zo = 50 Ω, Fr = 5 GHz, thickness = 0.020 Cu, oz ED, Pin for 100 °C rise

4.3.5 SIW design guidelines

The SIW only supports the propagation of TE modes as the metallised via holes do not allow the propagation of TM modes. The pair of parallel metallised via holes creates two parallel fences that disallow the flow of the longitudinal current. In the design of the SIW component, the losses must be minimised in its operating frequency range. When the distance between adjacent via holes increases, it may lead to the energy propagating through the gaps, resulting in increased leakage loss. For SIW, to have minimum leakage losses and not present any band gap at its operating bandwidth, the following design rules must be met (Deslandes & Wu, 2006:2520-2523).

$$d < p \qquad\qquad 4.12$$

Equation 4.12 states that via diameter, d, must be less than via spacing, p, for the structure to be physically realisable, otherwise the via holes will intersect.

$$p \leq 2d \qquad\qquad 4.13$$

Equation 4.13 specifies that the spacing, p, should be not more than twice the diameter, d, in order to minimise the radiation leakage loss.

$$p < \frac{1}{4}\lambda_c \qquad\qquad\qquad 4.14$$

SIW is a periodic structure; that is why it is also subjected to electromagnetic band effects. It is vital to avoid a band gap in the operating frequency band of the SIW, therefore the spacing, *p*, should be less than one-quarter of the cut-off wavelength as stated in Equation 4.14.

$$\lambda_c < 20p \qquad\qquad\qquad 4.15$$

Via holes are drilled and the production time is directly proportional to the number of via holes; hence Equation 4.15 states that the number of via holes should be less than 20 per wavelength in order to reduce manufacturing lead time. Equation 4.15 also avoids over-perforated substrates. Figure 4.13 shows the frequency region of interest for the design of an SIW structure.
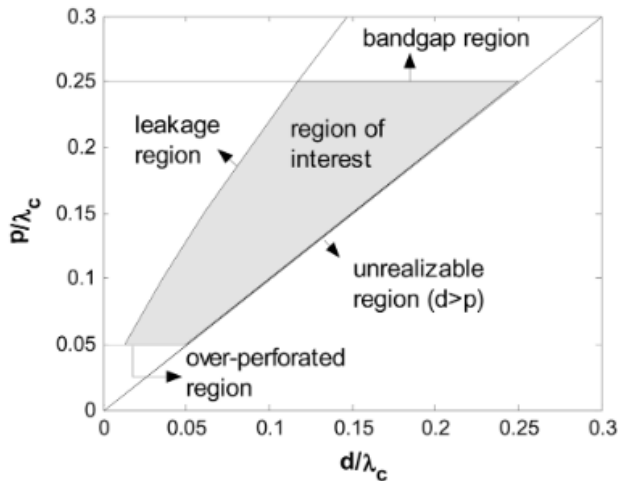
Figure 4.13: Region of interest for SIW in the plane of p/λc and d/λc (Deslandes& Wu, 2006:2521)

The cut-off frequencies of the SIW for TE_{10}, TE_{20} and TE_{30} given below are derived from Equation 3.3, with w_{eff} being the equivalent width defined in Equation 4.2 or 4.3.

$$f_{c10} = \frac{c}{2w_{eff}\sqrt{\varepsilon_r}}, \; f_{c20} = \frac{c}{w_{eff}\sqrt{\varepsilon_r}}, \; f_{c30} = \frac{3}{2}\frac{c}{w_{eff}\sqrt{\varepsilon_r}}$$

Because of the substrate thickness that is much smaller than the width in the SIW, the SIW is monomode (only TE_{10} will propagate) for frequencies between f_{c10} and f_{c20} as illustrated in Figure 4.14. The cut-off frequency is directly proportional to the width; thus, the width can be selected to allow only the fundamental mode to propagate for frequencies between f_{c10} and f_{c20}.
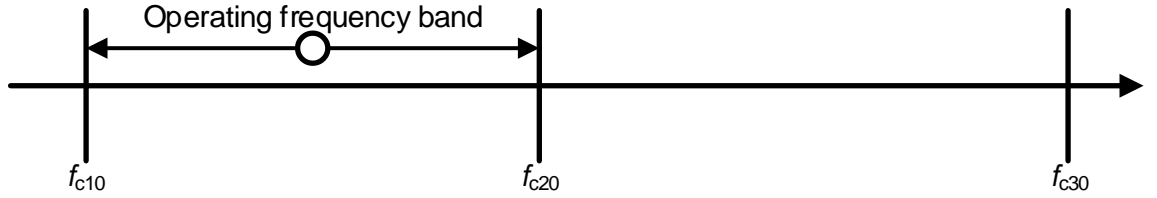
Figure 4.14: Cut-off frequencies of the SIW

Since the field propagation in the SIW is similar to that of the rectangular waveguide, the guided wavenumber, guided wavelength, and cut-off wavelength are given by Equations 3.4, 3.5 and 3.6, respectively. The conditions for the wave to propagate in SIW are the same as in the rectangular waveguide, where the cut-off wavelength must be greater than the operating wavelength, or the cut-off frequency must be smaller than the operating frequency, as shown by Equation 3.5.

4.3.6 Quality factor of SIW cavity resonator

The quality factor, denoted by Q, is the unit of measure for the losses of a cavity resonator. A high Q implies lower losses (Pozar, 2012:274). Metallic waveguides offer a very high, unloaded quality factor Q_u, which makes them preferable when high selectivity is required, but their drawback is their size and weight in most cases. Microstrip line resonators have low Q_u, due to high losses, thus making them unsuitable for many applications, although they are low cost (Mansour, 2009:85). Shen et al.(2013:256) state that the Q_u of an SIW filter is highly dependent on the conduction quality factor Q_c, dielectric loss quality factor Q_d and leakage quality factor Q_l. Q_c is related to the conduction loss and Q_l relates to leakage losses through the gap between adjacent via holes from the periodic structure.

$$\frac{1}{Q_u} = \frac{1}{Q_c} + \frac{1}{Q_d} + \frac{1}{Q_l}$$ 4.16

The leakage loss is negligible when the design rule in Equation 4.13 is satisfied at the operating frequency, making Q_u to depend on Q_c and Q_d as in Equation 4.17. (Tang et al., 2015:1314).

$$Q_u = \frac{Q_c Q_d}{Q_c + Q_d}, \text{ with } Q_c = \frac{k_g}{2\alpha_c}, Q_d = \frac{k_g}{2\alpha_d}$$ 4.17

From Equations 4.8 and 4.17, high Q_u can be achieved by increasing the thickness of a substrate, which may reduce its conduction loss. It can also be noted from Equation 4.9 that dielectric loss is directly proportional to the frequency. In most cases especially at high frequencies, dielectric loss is the main contribution to losses. Figure 4.15 shows

58

the relative insertion loss, size and cost of typical microwave resonators and SIW resonator with an estimated range of Q_u values for each resonator category (Chen & Wu, 2014a:112). Figure 4.15 shows that SIW outperforms the others as it offers the combination of high Q factor, low cost and low losses.
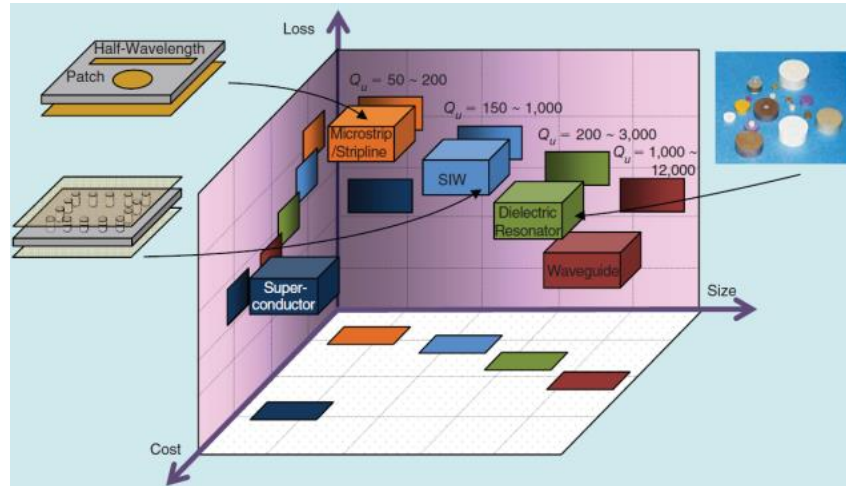
Figure 4.15: Relative insertion loss, size and cost of various RF resonators
(Chen & Wu, 2014a:112)

4.4   Planar transmission line to SIW transition

The SIW filters are measured by using a Vector Network Analyser (VNA), which needs to be connected to a 50 Ω transmission line. Thus, SIW structures need a transition to a planar transmission line. Since SIW is a rectangular waveguide in planar form in a dielectric substrate, it makes it easy to fabricate the transition as both the SIW and transmission line can be realised on the same dielectric substrate.

4.4.1 Microstrip to SIW transition

The microstrip to waveguide transition is presented by Deslandes and Wu (2001b:68-69), where the transition uses a tapered microstrip line to excite the SIW as illustrated in Figure 4.16.
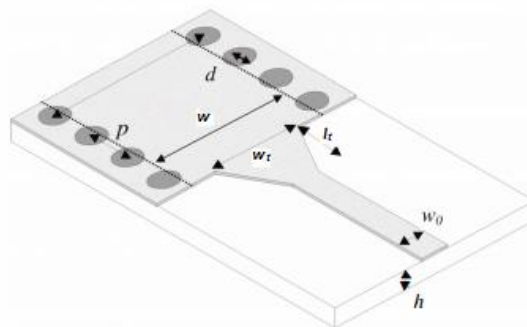
Figure 4.16: Microstrip to SIW configuration
(Deslandes, 2010:704)

The tapered microstrip line connects the 50 Ω microstrip line to an SIW structure. The electric field in the microstrip line is in the same direction as in the SIW, as illustrated in Figure 4.17, which makes the design of the microstrip to SIW transition easy (Deslandes & Wu, 2001b:68). The linear tapered microstrip line is used as it reduces the discontinuity effects and ensures the field matching between the microstrip and SIW over a broad bandwidth.

a) SIW
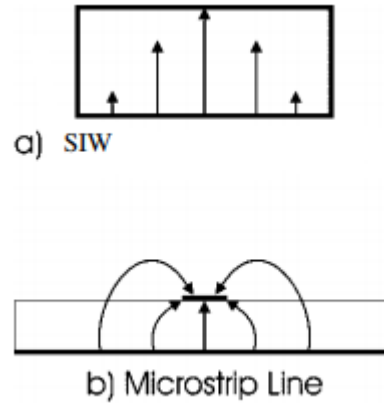
b) Microstrip Line

Figure 4.17(a): Electric field lines in an SIW, 4.17(b) Electric field lines in a microstrip line (Deslandes & Wu, 2001b:68)

Kumar et al. (2012:36-40) discuss the design technique for microstrip to SIW transition using a taper method with taper length and taper width being the two essential parameters. According to Kumar et al. (2012:38), the initial values of the taper width, w_t, and the taper length, l_t, in Figure 4.16, can be determined by using Equations 4.18 and 4.19, respectively. Then the dimensions of the taper can be optimised to obtain the field match between microstrip and SIW.

$$\frac{w_t}{w} \approx 0.4 \qquad\qquad 4.18$$

$$\frac{\lambda_g}{2} < l_t < \lambda_g \qquad\qquad 4.19$$

Deslandes (2010:705-706) derives an equation relating optimum taper width to SIW width. The optimum taper width can be found by equating Equations 4.20 to 4.21 (Deslandes, 2010:706-707).

$$\frac{1}{w_e} = \left\{ \begin{array}{c} \frac{60}{\eta h} \ln\left(8\frac{h}{w_t} + 0.25\frac{w_t}{h}\right) \\ \frac{120\pi}{\eta h[\frac{w_t}{h} + 1.393 + 0.667 \ln(\frac{w_t}{h} + 1.444)]} \end{array} \right\} \qquad 4.20$$

$$\frac{1}{w_e} = \frac{4.38}{w}e^{\left(-0.627\frac{\varepsilon_r+1}{2}+\frac{\varepsilon_r-1}{2\sqrt{1+12\frac{h}{w_t}}}\right)}$$ 4.21

Huang et al. (2010:233-244) propose methods that can be used to excite an SIW when its thickness is different from the microstrip line. The methods are probe feeding with a via hole and probe feeding with an open slot as shown in Figure 4.18. The reflection coefficient plots for the feeds below are given in Huang et al. (2010:236-244).
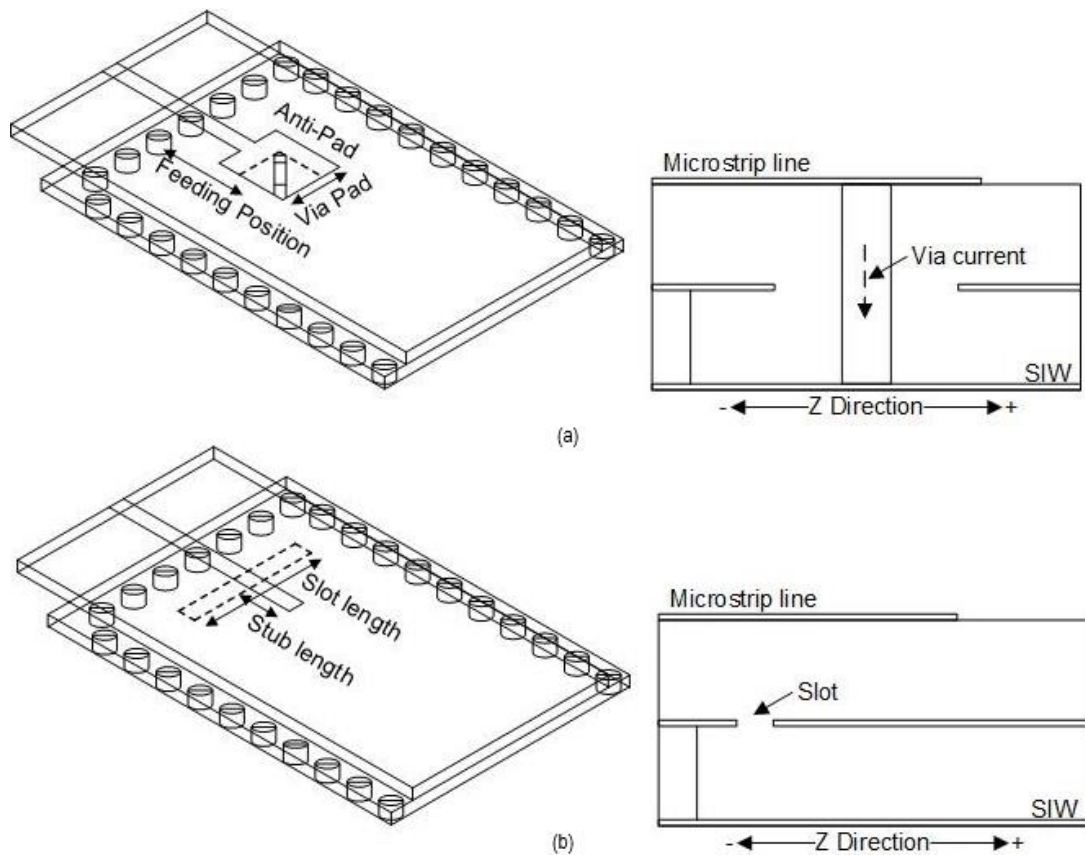
Figure 4.18: Microstrip to SIW transition by probe feeding with (a) via hole and its side view, (b) open slot and its side view (Huang et al., 2010:228)

Cassivi, Perregrini, Wu et al. (2002:1-4) presented four different coupling topologies shown in Figure 4.19 to connect an SIW structure to a microstrip transmission line, allowing easy integration.
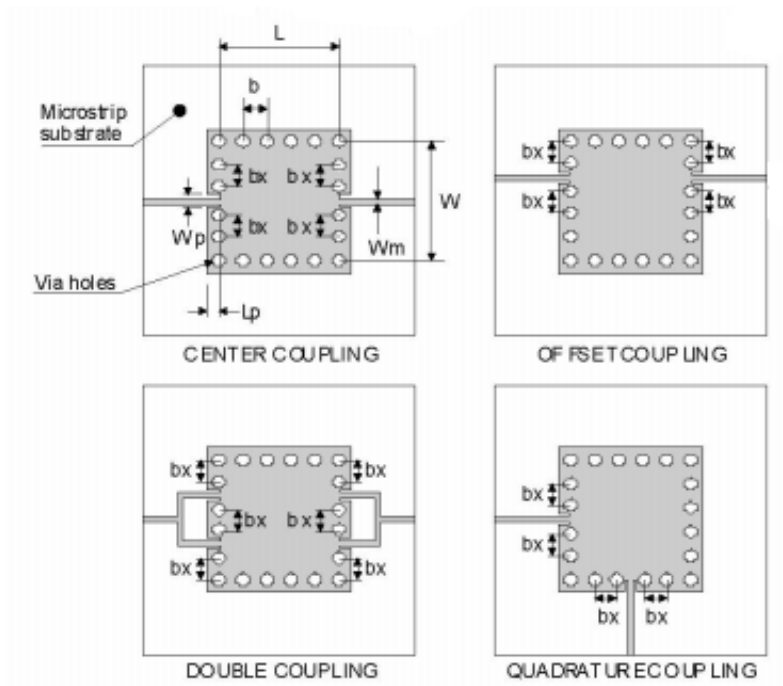
Figure 4.19: Coupling topologies between SIW cavities and microstrip line (Cassivi,Perregrini, Wu et al., 2002:1)

Cassivi, Perregrini, Wu et al. (2002:3) conclude that the offset coupling allows the cavity to be excited with almost all possible modes, while the centre and double coupling topology allows the SIW cavity to be excited with odd *m* modes with the double coupling giving the strongest coupling. The quadrature coupling topology can be combined with the centre or double coupling, allowing the SIW cavity to be excited with odd *m* and *p* modes only.

4.4.2 Coplanar waveguide to SIW transition

Deslandes and Wu (2001a:619-622) developed a coplanar waveguide (CPW) and an SIW integrated on the same substrate as shown in Figure 4.20. A stub is added on the CPW to match the transition in order to obtain a low insertion loss. The length of each bend slot on the CPW is approximately a quarter of the guided wavelength, which allows an electric field to be minimum at the end and maximum at the other end.
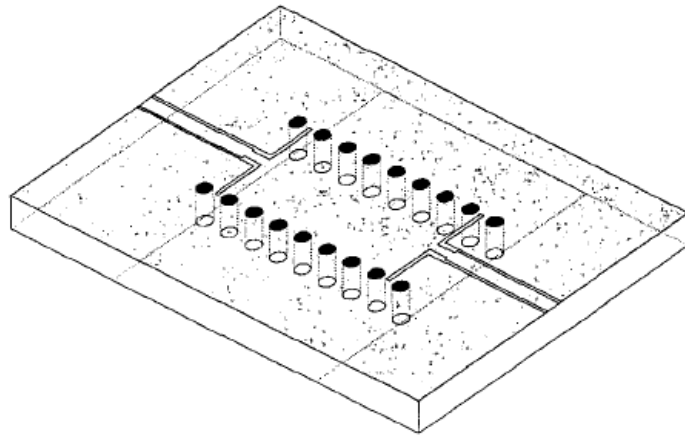
Figure 4.20: SIW and coplanar waveguide (Deslandes& Wu, 2001a:619)

Chen and Wu (2009a:349-352) propose a conductor-backed coplanar waveguide (CBCPW) to SIW transition arranged back to back as shown in Figure 4.21. The slot width is determined using the 50 Ω impedance CBCPW, thus the strip width that looks like a microstrip line had to be chosen wider than the 50 Ω CBCPW. This type of transition provides both field and impedance matching. According to Chen and Wu (2009a:350), the spurious modes that are normally present in the CBCPW can be suppressed by shorting the two ground conductors on either sides of 50Ω conductor strip with the backside ground using metallised via holes.
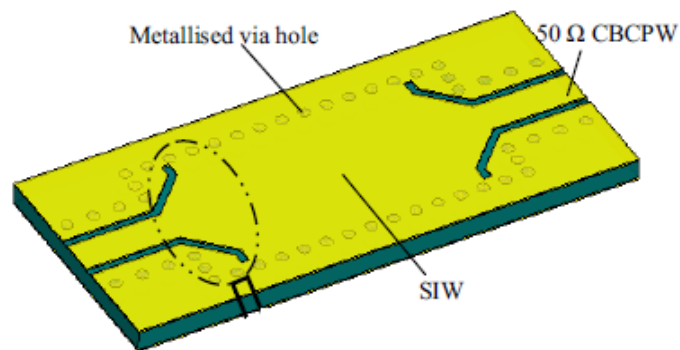
Figure 4.21: CBCPW to SIW transition (Chen & Wu, 2009a:350)

According to Cassivi, Perregrini, Wu et al. (2002:3), the coupling topologies illustrated in Figure 4.19 can also be used to link the SIW cavities to the CPW. Cassivi, Perregrini, Wu et al. (2002:2) illustrate an SIW cavity made up of two rows of via holes coupled to a CPW, as illustrated in Figure 4.22 overleaf.
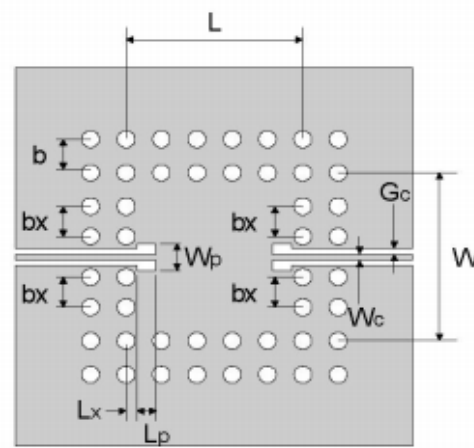
Figure 4.22: SIW cavity made up of two rows of via holes coupled to coplanar waveguide (Cassivi, Perregrini, Wu et al., 2002:2)

4.5 Summary

The SIW exhibits higher losses than a hollow rectangular waveguide operating at the same frequency, owing to the dielectric losses that are present in the SIW and not present in the hollow rectangular waveguide. The attenuation due to conductor loss is inversely proportional to the thickness of the waveguide; therefore in the SIW, the conductor losses are more than in the rectangular waveguide, because the thickness in the SIW is much thinner than in the rectangular waveguide. The metallic waveguides are bulky and heavier than the SIW, thus they do not meet nanosatellite limitations (size and mass). They are also not suitable for low-cost applications. The comparison done by Bozzi et al.(2008b:517-518) concludes that the SIW exhibits better performance in terms of losses in the upper part of the operating frequency when compared with microstrip and coplanar waveguides built on the same dielectric substrate. The attenuation of the microstrip and the coplanar waveguide increases monotonically with frequency, while attenuation decreases with frequency in the SIW as illustrated in Figure 4.8. Thus, SIW technology achieve a balance between performance and SWaP-C solution than metallic waveguide and planar structures.

CHAPTER 5. FILTER THEORY TO SUBSTRATE INTERGRATED WAVEGUIDES

5.1 Introduction

The basic design guidelines of SIW was presented in the previous chapter. This chapter presents application of the filter theory to substrate integrated waveguides. The chapter commences by discussing miniaturisation techniques of SIW and shapes of SIW cavities. The techniques used to create transmission zeros at finite frequencies and synthesis of coupled resonator filters are also presented in this chapter.

5.2 Miniaturisation techniques of SIW

SIW is still too wide for some practical applications. With the aim at a reduction of the size of an SIW, several techniques to miniaturise the SIW size with limited impact on the performance have been proposed and investigated. Such techniques as half mode substrate integrated waveguide (HMSIW) and substrate integrated folded waveguides (SIFW).

5.2.1 Half mode substrate integrated waveguide

Half mode substrate integrated waveguide (HMSIW) is introduced by Hong et al. (2006:219). It incorporates a cutting of the SIW along planes of symmetry in the transmission direction as depicted in Figure 5.1. From HMSIW structure as shown in Figure 5.1, it can be observed that the metallic surface area and the width of the waveguide is reduced by nearly half. Due to the low width to height ratio of the SIW, the open side aperture of the HMSIW is nearly equivalent to the perfect magnetic wall, thus in Figure 5.2, it can be observed that the field distribution of the fundamental mode in the HMSIW is similar to half the field distribution of the fundamental mode in the SIW.
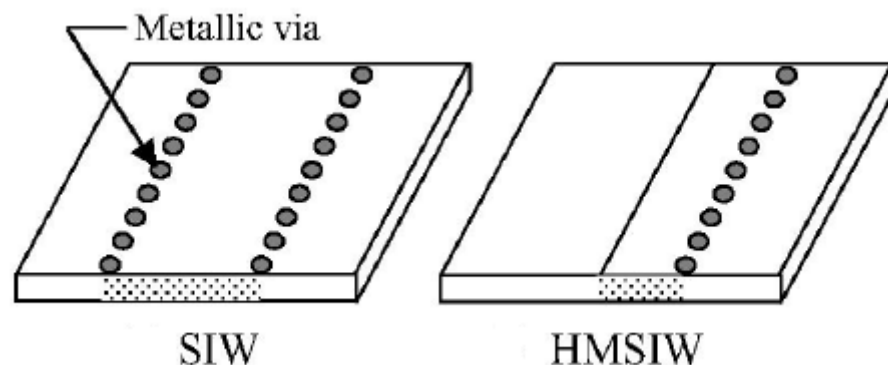
Figure 5.1: The structure of SIW and HMSIW (Hong et al., 2006:219)
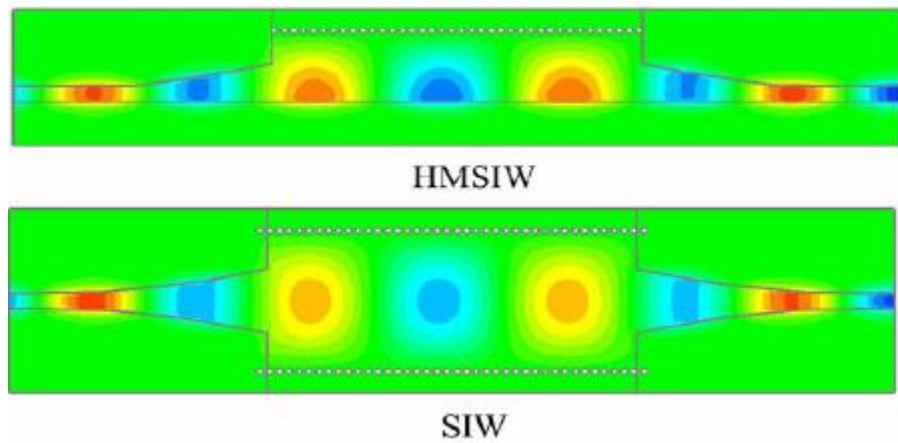
Figure 5.2: Fundamental mode field distribution in HMSIW and SIW (Hong et al., 2006:219)

Lai et al. (2009:1996-2004) investigated the propagation properties of HMSIW using theoretical and experimental methods. The field distribution inside and outside HMSIW is analysed using two equivalent models, first HMSIW model designed to operate in the *X*-band and second HMSIW prototype is designed to operate in the *Ka*-band (20-60 GHz). The equation to calculate an electric field component E_y inside the HMSIW and the normalised electric filed outside the HMSIW are derived by Lai et al. (2009:1997-1999) from the equivalent model of the HMSIW depicted in Figure 5.3. The normalised electric field inside the HMSIW and outside the HMSIW can be determined using Equation 5.1 and Equation 5.2, respectively (Lai et al., 2009:1998-1999).
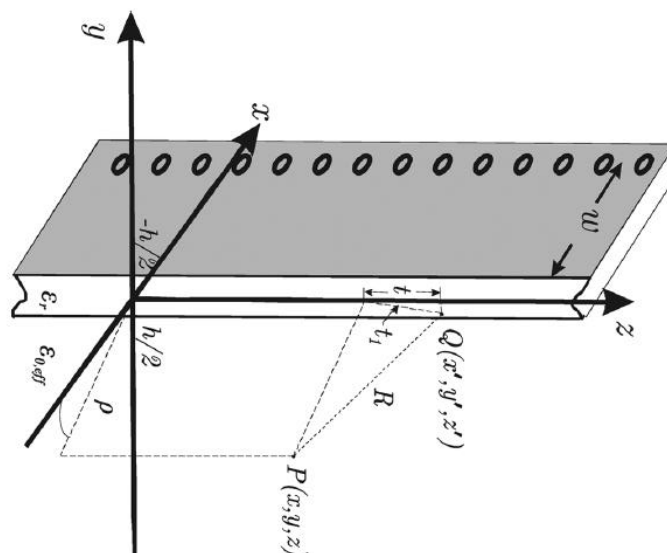
Figure 5.3: Equivalent model of the HMSIW for the calculation of the field distribution (Lai et al., 2009:1997)

$$\overline{E}_\varphi = \sin k_x\,(w\text{-}x)e^{-jk_zz} \qquad\qquad 5.1$$

$$\overline{E}_\varphi = \frac{h\sin(k_xw)}{2\pi}\,e^{-jk_zz} \times \int_{-\Delta l}^{\Delta l} \frac{\left(1 + jk_{0,eff}\sqrt{\rho^2 + t^2}\right)\rho e^{-jk_{0,eff}\sqrt{\rho^2 + t^2}-jk_zt}}{\left(\rho^2 + t^2\right)^{3/2}}\,dt \qquad 5.2$$

Lai et al. (2009:1997) compared the calculated and simulated normalised electric field in the two HMSIW prototypes by plotting them in the same graph as shown in Figure 5.4, which shows a good agreement between calculated and simulated results. In Figure 5.4, the normalised electric field outside the HMSIW is represented by the plots where $x/w < 0$ while the normalised electric field inside the HMSIW is plotted where $0 < x/w < 1$.
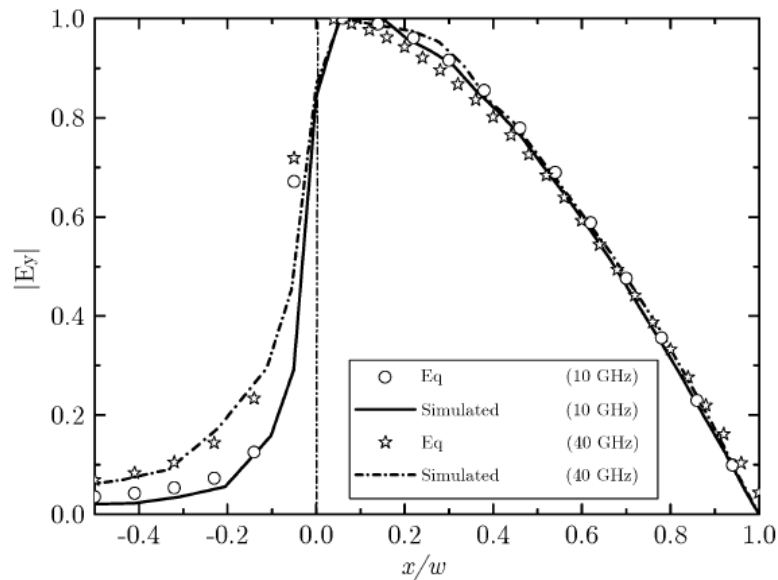
Figure 5.4: Normalized electric field in cross section for two HMSIW prototypes operating in *X*- and *Ka*-band (Lai et al.,2009:1997)

5.2.2 Folded substrate integrated waveguide

Folded substrate integrated waveguide (FSIW) technique is the technique that is mainly obtained by folding the SIW around a conductor septum as depicted in Figure 5.5 (Grigoropoulos et al., 2005:829-831). The cross section view of the FSIW which is categorised into two types, namely C-type and T-type depending on the way they are folded is shown in Figure 5.5.
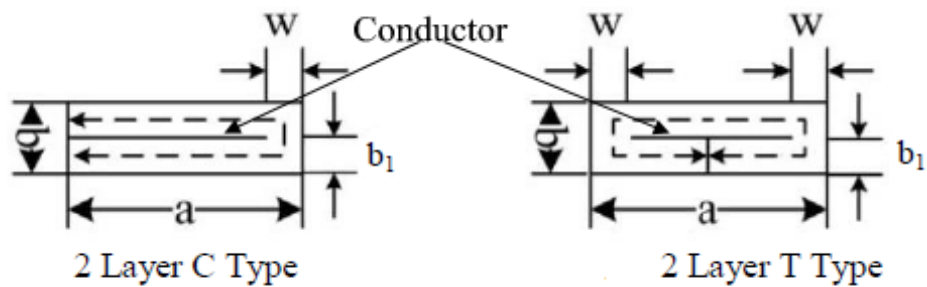
Figure 5.5: Cross section of FSIW (Ding & Wu, 2009:705, Grigoropoulos et al., 2005:829)

Ding and Wu (2009:705:708) designed and fabricated a T-type folded substrate integrated waveguide (TFSIW) hybrid ring in a double layered substrate. The design procedure of a TFSIW hybrid ring is introduced and basic characteristic parameters of TSFSIW, such as attenuation constant and phase constant are also analysed. The total size of the hybrid ring based on TFSIW is then much smaller than its counterpart based on the SIW technique. Cheng et al. (2011:45-58) proposed a multilayer folded substrate integrated waveguide butler matrix with a single layer SIW based butler matrix folded thrice to construct miniaturised four lay structure. This allowed an efficient method to miniaturise the circuit area of SIW butler matrix without worsening its excellent characteristics. The multilayer folded SIW butler matrix achieved miniaturisation of more than 60% compared to the single-layer structure.

Shen et al. (2011:418-420) presented a design of a quadruple folded SIW to miniaturised a dual band filter. They compared the fabricated quadruple FSIW to other dual band filters and were able to achieve a size reduction of 50%. Jones and Daneshmand (2017:528-531) proposed and designed a folded ridge half mode SIW (FRHMSIW) technique for extreme miniaturisation of the SIW structure by combining the benefits of folded and ridge half mode techniques. Figure 5.6 shows 3D and cross section view of HMSIW, ridge HMSIW (RHMSIW) and FRHMSIW. For FRHMSIW, the standard SIW is cut half along the propagation direction as shown in Figure 5.6(a) giving 50% miniaturisation but still maintains the propagation characteristic of the standard SIW due to its low width to height ratio. RHMSIW further miniaturises the HMSIW by introducing a capacitive ridge along the open side as shown in Figure 4.6(b). Then the ridge structure is moved inside the waveguide channel which further miniaturised the waveguide by 25% more without an increase in design complexity or reduction in performance.
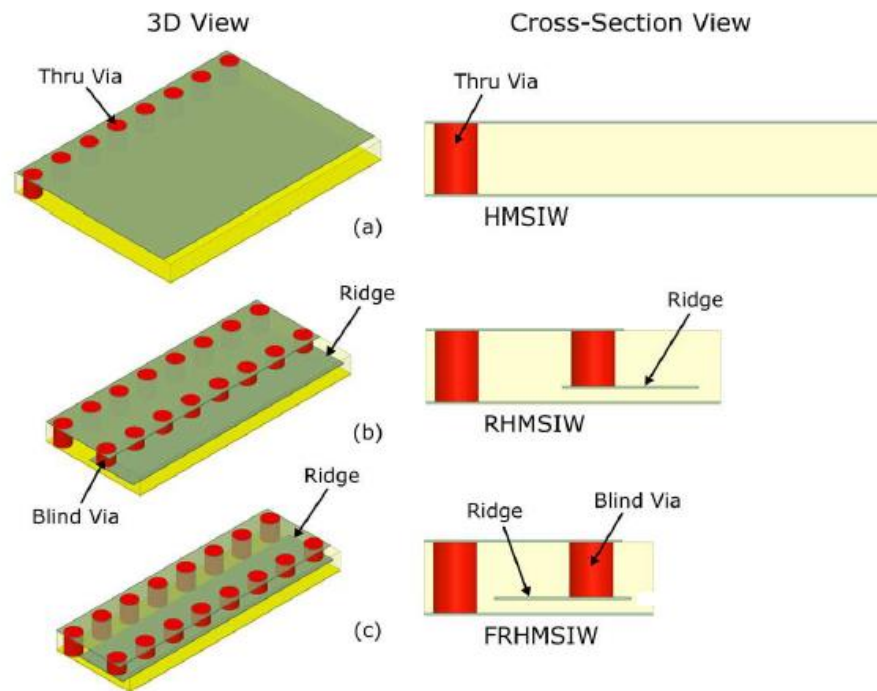
Figure 5.6: 3D configuration and cross-section view of the (a) half mode SIW, (b) ridged half mode SIW and (c) folded ridged half mode SIW (Jones & Daneshmand, 2017:528)

5.3 SIW filters

A simplest form of SIW filter is the inline structure, which is made up of two rows of metallised via holes with other metallised via holes inside the SIW structure, which are used to define SIW filter cavities. These SIW filter cavities are either defined by iris window or inductive posts.

5.3.1 SIW cavity shapes

An SIW cavity with different sizes and shapes, such as rectangular and circular forms often allow the control of the position of the transmission zero outside the passband to improve filter selectivity. Chen et al. (2005:787-789) have designed the fourth order SIW filter that composed of rectangular cavities, and the passband that is centred at 10 GHz. The geometry of this filter is illustrated in Figure 5.7 where the length and width of the SIW cavity were determined using Equation 4.2. The higher quality factor for this filter geometry can be achieved when the length and width of the cavity are equal. Chen et al. (2005:788) uses the single SIW cavity first to determine the external quality factor then two coupled SIW cavities to determine internal coupling. Then the modes are tuned using electromagnetic simulation software by adjusting the geometry until the model response matches the prototype requirements. The frequency response is shown in Figure 5.18 on page 80.
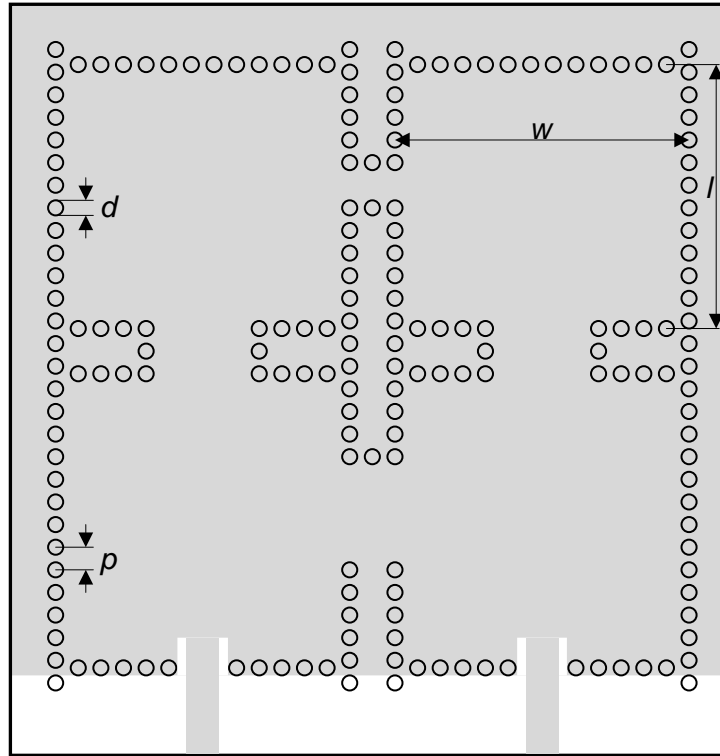
Figure 5.7: Geometry of SIW filter with rectangular cavities (Chen et al., 2005:788)

Tang et al. (2005:1-2) designed a set of millimetre-wave SIW filters with two circular cavities, and investigated the influence of the angle between the input and output on an SIW circular cavity as shown in Figure 5.8. By locating the position of the transmission zero which affect the steepness of the transition region (passband to stopband region), they found that the angle between the input and output on an SIW circular cavity is more sensitive to the upper stopband rejection response but not sensitive to the passband. The simulated and measured frequency responses of the designed SIW filters are presented in Tang et al. (2005:1-2), which showed a very steep response to the upper stopband region. Figure 5.8 shows a configuration of the SIW filter with circular cavity and its ideal frequency response that exhibit a very steep transition region to the upper stopband with the frequency normalised using Equation 2.10.
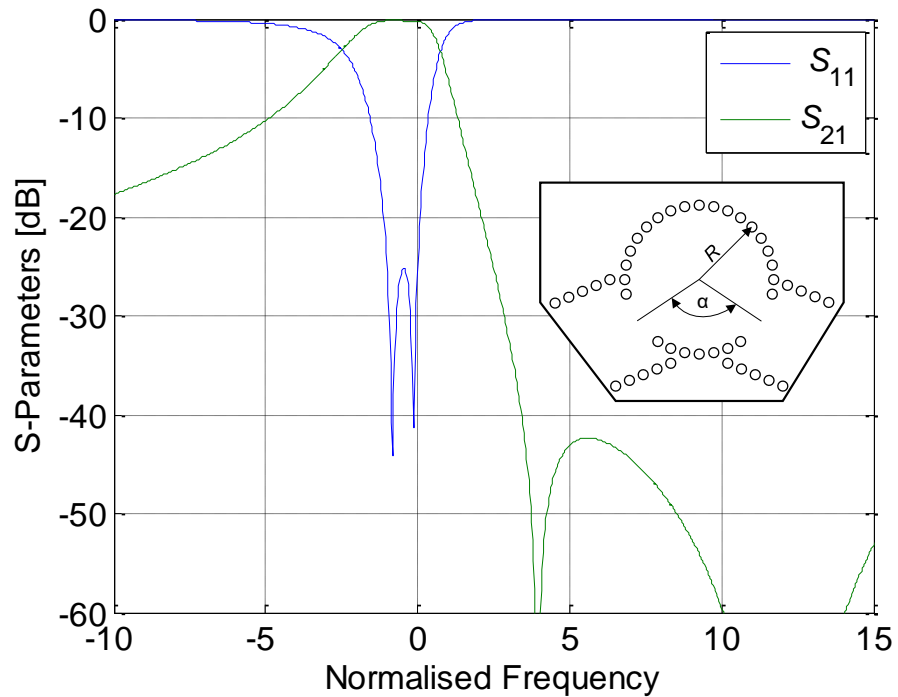
Figure 5.8: Configuration of the SIW filter with circular cavity and its ideal frequency response (Tang et al., (2005:1)

The angle between the input and output port of the SIW circular cavity investigated by Tang et al. (2005:1-2) is found to be optimal at 75°, thus they conclude that SIW filters can be also realised by cascading the circular SIW circular cavities with an optimal angle as illustrated in Figure 5.9.
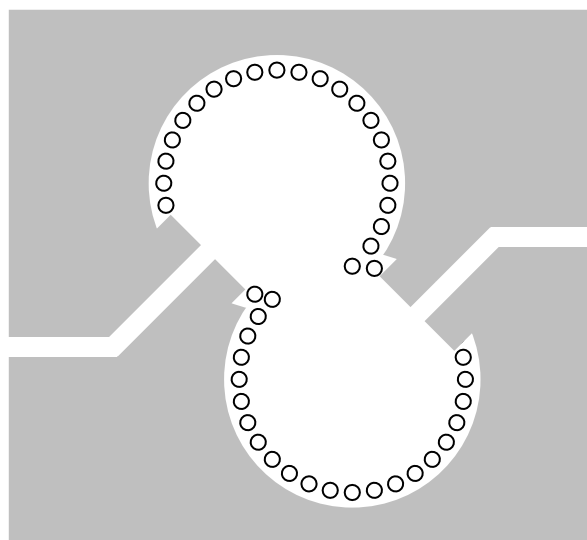
Figure 5.9: Cascaded SIW circular cavities with optimal angle (Tang et al., 2005:1)

Tang et al. (2007:778) studies the characteristics of a dual mode filter with a single cavity as illustrated in Figure 5.10. They found that the SIW elliptic cavity exhibit a very

steep transition region to the lower stopband which is complimentary to the SIW circular cavity. The configuration of the SIW filter with elliptic cavity and its frequency response is illustrated in Figure 5.10, which shows that it exhibits a very steep transition region to the lower stopband.
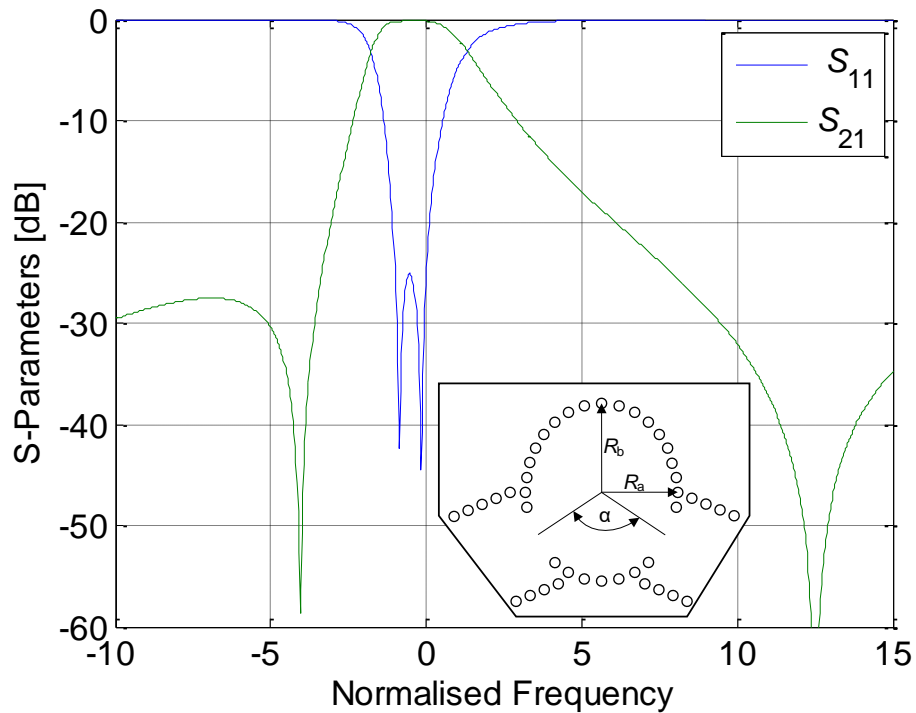
Figure 5.10: Configuration of the SIW filter with elliptic cavity and its ideal frequency response (Tang et al.,2007:778)

Based on the complementary characteristics of the SIW filter with circular and elliptic cavities, Tang et al. (2007: 776-782) proposed a diplexer with two dual mode SIW circular and elliptic cavities which has a T-junction as shown in Figure 5.11. The filter is constructed by cascading two circular and two elliptic SIW cavities to get a steeper roll off slope. In the ideal frequency response in Figure 5.11, the upper channel response is produced by the SIW elliptic cavities while the lower channel response is produced by the SIW circular cavities. The measured frequency response is presented in Tang et al. (2007: 776-782).
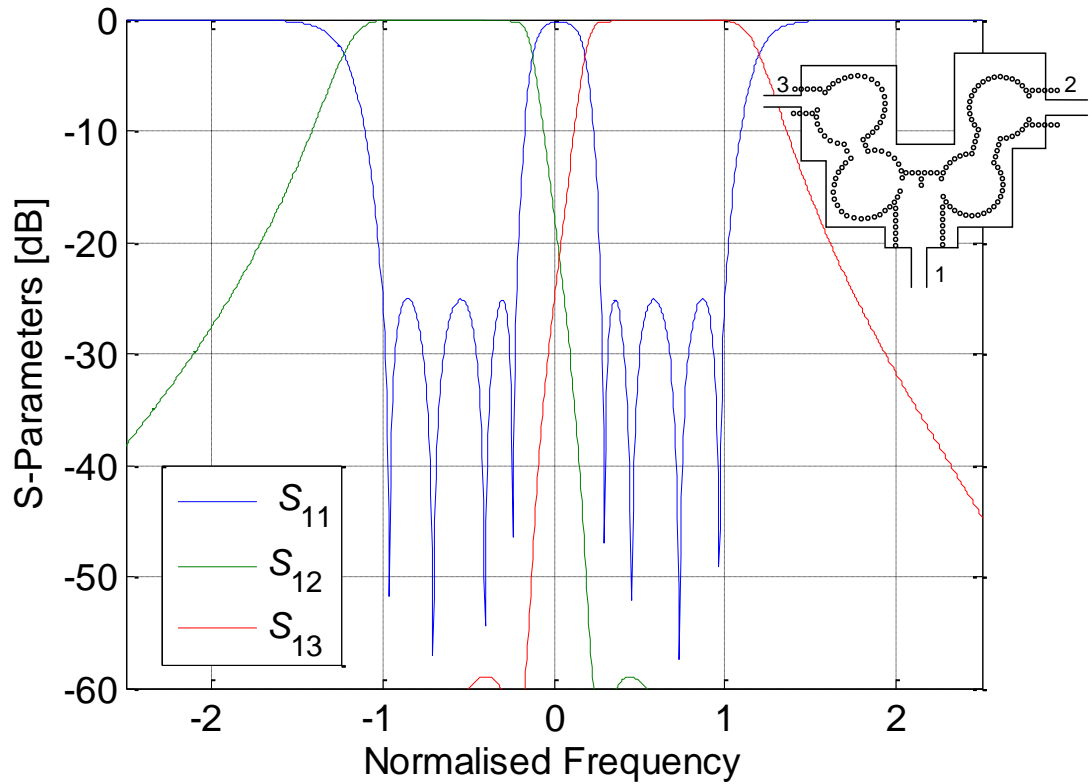
Figure 5.11: SIW diplexer and its ideal frequency response (Tang et al., 2007:779)

Tang et al. (2007:777) also estimated by simulation the unloaded quality factor of different SIW cavities as tabulated in Table 5.1, which show that the circular and elliptic cavity have a slightly higher quality factor than that of the square cavity.

Table 5.1: Unloaded quality factor

Cavity shape	Eigen mode	Q_0 and frequency
Square	Fundamental mode TE_{102} and TE_{201}	270 @ 17.41 GHz 317 @ 27.53 GHz
Circular	Fundamental mode TE_{110}	274 @ 17.41 GHz 324 @ 27.53 GHz
Elliptic	Fundamental mode quasi TE_{110}	274 @ 17.29 GHz 319 @ 26.72 GHz 327 @ 28.35 GHz

With many various types of SIW rectangular cavity filters with flexible structures that are designed such as FSIW, HMSIW and etc, and SIW circular cavity which exhibit high quality factor, Xu et al. (2012: 1521-1527) proposed a hexagonal SIW cavity as illustrated in Figure 5.12 which will combine the flexibility of rectangular cavity with the performance of circular cavity. They also give Equation 5.3 as an approximate formula

that can be used to determine the initial dimensions of a hexagonal SIW cavity before the electromagnetic simulation software is used to optimise the final dimensions. The sides of a hexagonal SIW cavity can be used for coupling as shown in Figure 5.12.
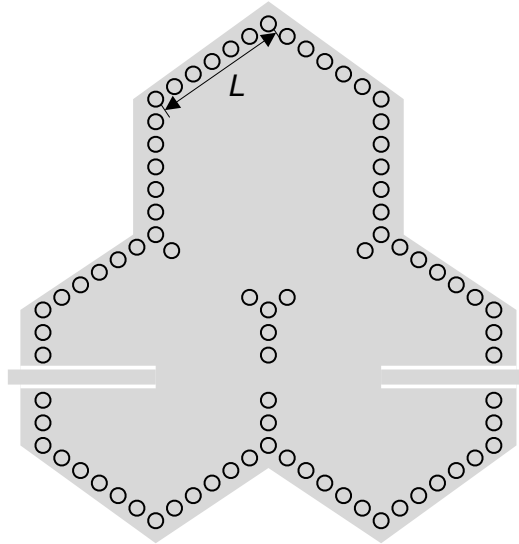
Figure 5.12: Geometry of a hexagonal SIW filter (Xu et al., 2012:1524)

$$L = \frac{C_0}{\sqrt{\varepsilon_r}} \frac{\mu'}{2\pi f_r} \qquad 5.3$$

In Equation 5.3, C_0, ε_r and f_r are speed of light, dielectric constant of the substrate and fundamental resonant frequency of the hexagonal SIW cavity, respectively. The $\mu' = 2.75$ is the modified root coefficient base on the Bessel function.

5.3.2 Iris window SIW filter

Hao et al. (2005:598-601) presented a method to designed an SIW filter that has its coupling between the adjacent cavity controlled by the size of the iris window as illustrated in Figure 5.13. The method starts with general filter theory as explained in Chapter 2, where the low pass prototype parameters are calculated from the specifications followed by the equivalent circuit for a bandpass SIW filter which is made up of resonators and impedance inverter. The values of an impedance inverter are calculated from the element values (g_0 to g_{N+1}) as discussed in Chapter 2, which can

be realised by iris window in the SIW. Then electromagnetic simulation software is used to optimise the SIW filter.
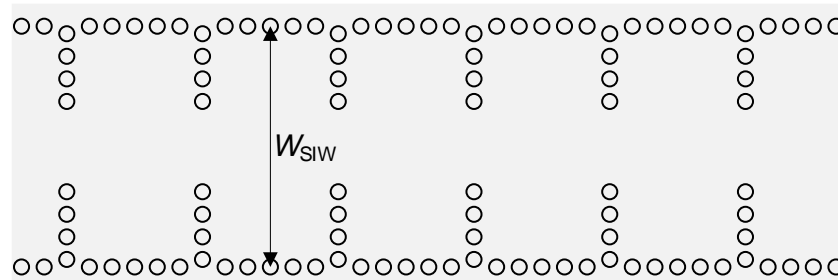
Figure 5.13: SIW filter with metallic via impedance window (Hao et al., 2005:599)

The determination of the opening of the iris window and cavity dimensions is one of the requirements in filter design. The opening of the iris window corresponds to the quality factor, that is for inner cavities that have higher quality factor the iris window is more closed compared to the ones for external cavities that have lower quality factor.

5.3.3 Inductive post SIW filter

In a simple inductive post SIW filter, cavities are defined by single metal via hole that is either placed centred or offset with respect to the vertical symmetry plane of the SIW structure as shown in Figure 5.14 (Deslands & Wu, 2003a:595). SIW filter with inductive posts normally use a number of posts of different diameter all centred in the waveguide, with first and last posts having a smaller diameter in order to achieve a good input matching. According to Deslands and Wu (2003a: 595), an SIW filter geometry of inductive post of different diameters centred in the waveguide can be set up by simulations that are made to extract the positions of an equivalent post having a same diameter in an offset arrangement.

(a)

(b)
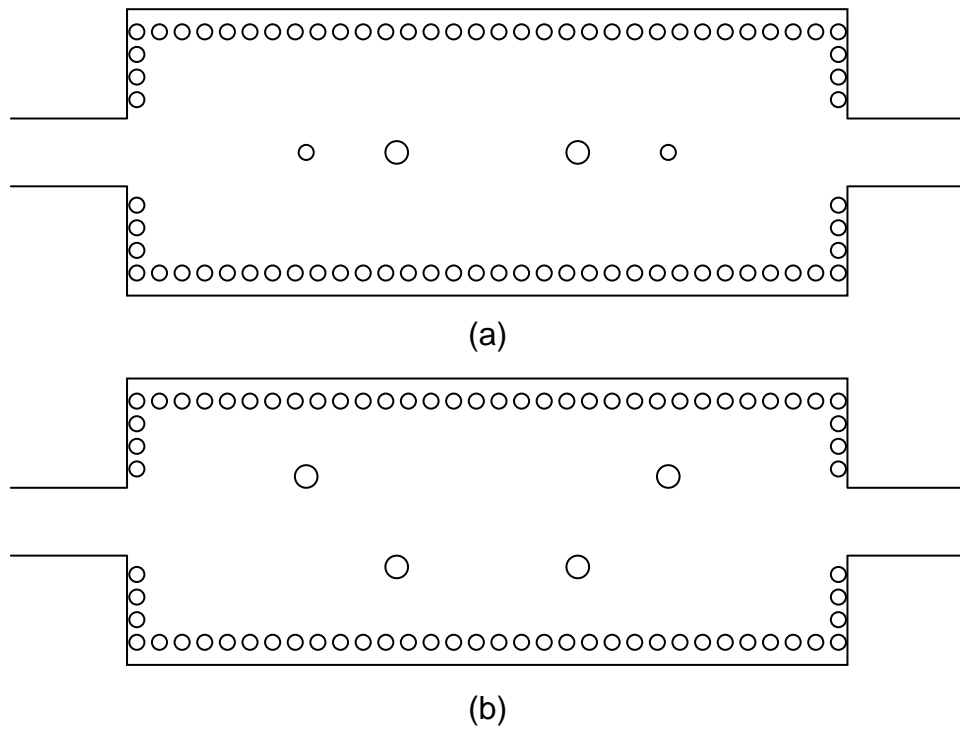
Figure 5.14: SIW filter with (a) centred post and (b) offset post (Deslands& Wu, 2003a:595)

Deslands and Wu (2003b:1917-1920) presented a design technique for an SIW filter that is based on inductive posts of the same diameter. The technique begins with the general filter theory discussed in Chapter 2 where the element values (g_0 to g_{N+1}) for all filter orders (N) are computed from the filter specifications (return loss or passband ripple). The stopband insertion loss is used to give the minimum order needed for the filter (N) using a chart similar to the one in Figure 2.5. Once the filter order is known, the calculated element values for the filter (g_0 to g_{N+1}) are converted to the impedance inverter using equations in Section 2.6. Then the dimensions of the waveguide are calculated using Equations 4.1 to 4.3 to obtain a single mode operation for the frequency of interest. According to Deslands and Wu (2003b:1918-1920), an equivalent network in Figure 5.15 can be used to model a post in a waveguide. The parameters of an equivalent network can be computed using Equation 5.4.
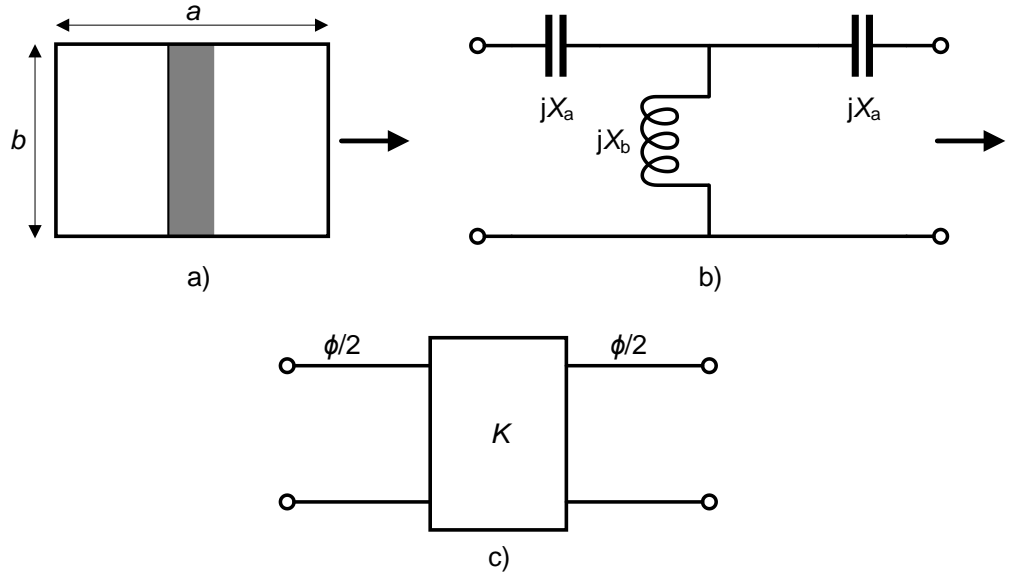
Figure 5.15: Design process of inductive post filter. (a) Post in waveguide (b) Equivalent network (c) Equivalent K-inverter network (Deslands & Wu, 2003b:1918)

$$\frac{jX_b}{Z_0} = \frac{2S_{21}}{(1 - S_{11})^2 - S_{21}^2} \quad , \quad \frac{jX_a}{Z_0} = \frac{1 + S_{11} - S_{21}}{1 - S_{11} + S_{21}} \tag{5.4}$$

An equivalent network of the post in the waveguide is then transformed to an impedance inverter using Equation 5.5.

$$\varnothing = -\tan^{-1}\left(\frac{2X_b}{Z_0} + \frac{X_a}{Z_0}\right) - \tan^{-1}\left(\frac{X_a}{Z_0}\right) \quad , \quad K = Z_0 \left| \tan\left(\frac{\varnothing}{2} + \tan^{-1}\left(\frac{X_a}{Z_0}\right)\right)\right| \tag{5.5}$$

With the calculated impedance inverter values for the post in the waveguide, an iterative method is used to find the required post diameter, according to Deslands and Wu(2003b:1919). They also give the equations to compute the distance between each post (I_N) as follows:

$$\theta_N = \pi + \frac{1}{2}(\varnothing_N + \varnothing_N) \quad , \quad I_N = \frac{\theta_N \lambda_{g0}}{2\pi} \tag{5.6}$$

With all the dimensions for an inductive post SIW filter calculated, an electromagnetic simulator can be used to optimise the structure. Deslands and Wu (2003b:1918-1920) presented in their paper a 3-pole inductive filter designed using this technique, with the simulated and measured results in good agreement.

5.3.4 SIW filters with transmission zeros

Transmission zeros are the frequencies where there is no power is transmitted, and there is a total reflection of power. Transmission zeros are created on the imaginary axis of the complex plane to improve selectivity or to achieve a wide stopband, or on the real axis or in all four quadrants to improve the phase and group delay response in the passband. Figure 5.16 illustrates permissible locations of transmission zeros.
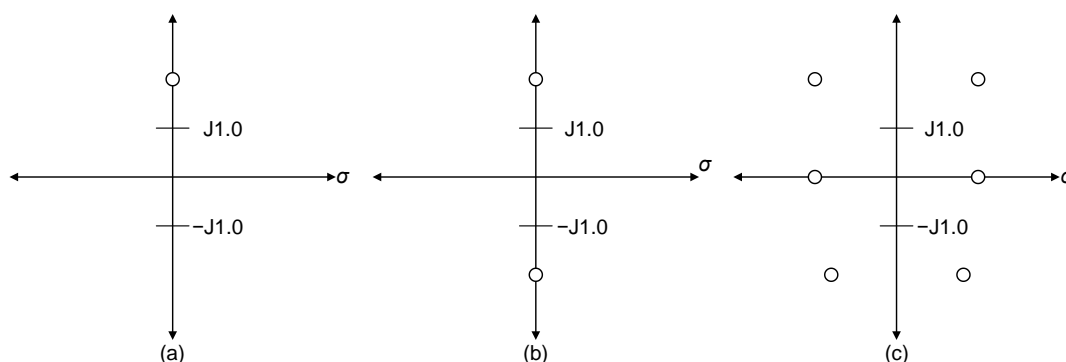
Figure 5.16: Permissible transmission zero location to realise filter response with transmission zero: (a) in the upper band, (b) in the upper and lower bands, and (c) to realize linear phase response

Cross coupling between adjacent cavities can be used to generate transmission zeros at finite frequencies. SIW filters with finite transmission zeros on the imaginary axis of the complex plane tends to have a better selectivity of the amplitude response while SIW filters with finite transmission zeros on the real axis or in all four quadrants realise a linear phase response in the passband.

There are two techniques that are normally used to create transmission zeros at finite frequencies. The first technique makes use of cross couplings with nonphysical couplings by high order modes or physical coupling structures to produce multi paths for signal flow. A finite transmission zero on the imaginary axis is produced when two different signal paths give the same magnitude but opposite phase to cancel each other out, with both positive and negative structures needed to be realised simultaneously for the opposite phases. An example of this case is the fourth order SIW cross coupled bandpass filters that are proposed and designed by Chen and Wu (2008: 142-149) using the negative coupling structures, and the filters are found to have very good selectivity. With the SIW filter exhibiting very good selectivity, they design the structure that provide both positive and negative coupling which cancel each other out and produce finite transmission zeros on the imaginary axis. Figure 5.17 shows the

geometric configuration, structural topology and ideal frequency response of one of their fourth order SIW cross coupled filters with transmission zeros at ± j2.65.
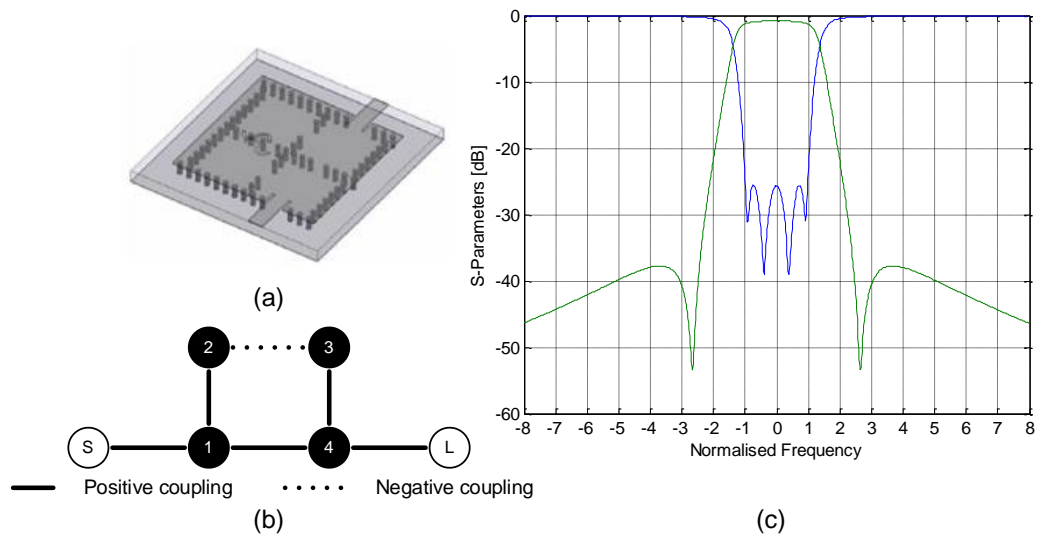
Figure 5.17: (a) The geometric configuration, (b) structural topology and (c) ideal frequency response of the fourth order SIW filter with transmission zeros at the imaginary frequencies. (Chen and Wu, 2008:146)

In Figure 5.17, all the couplings between the SIW cavity resonators are obtained by magnetic post-wall iris which provide positive coupling except for the coupling between SIW resonators 2 and 3. A structure using a balanced microstrip with a pair of metallised via holes is placed between SIW cavity 2 and 3 to invert the phase of the signal. Thus a mixed coupling is produced, of both positive and negative coupling which cancel each other out. The structure is optimised as such that negative coupling is stronger than the positive coupling for optimised dimensions and a small amount of negative coupling is cancelled out by tuning the width of the magnetic post-wall iris. The measured and simulated frequency responses are in good agreement, which showed that the filter has a very good selectivity, as presented by Chen and Wu (2008:146) in their paper.

A finite transmission zero on the real axis is produced when two signal paths yield the same magnitude and phase. All of the couplings can have the same sign for this case. A good example of an SIW filter with finite transmission zeros on the real axis is the fourth order SIW filter that was proposed and realised by Chen et al. (2005:787-789), with its geometric configuration shown in Figure 5.7. The SIW filter have three direct couplings and one cross coupling between the first and the fourth SIW cavity resonators

which are all magnetic or inductive. With finite transmission zeros on the real axis in this case, the SIW filter realise a linear phase response in the passband. An ideal frequency response and group delay of the fourth order SIW linear-phase filter (shown in Figure 5.7) that was proposed by Chen et al. (2005:787-789), with the centre frequency at 10 GHz, ripple bandwidth of 1% and two finite transmission zeros that are symmetrically located along the real axis are shown in Figure 5.18. In Figure 5.7, the cross coupling between SIW resonators 1 and 4 is responsible for the generation of two finite transmission zeros that are symmetrically located on the real axis. The simulated and measured frequency responses of the fourth order SIW linear phase which shows a good agreement are presented by Chen et al. (2005:789) with the in-band group time group delay variation smaller than 0.5% over 50% of the passband.
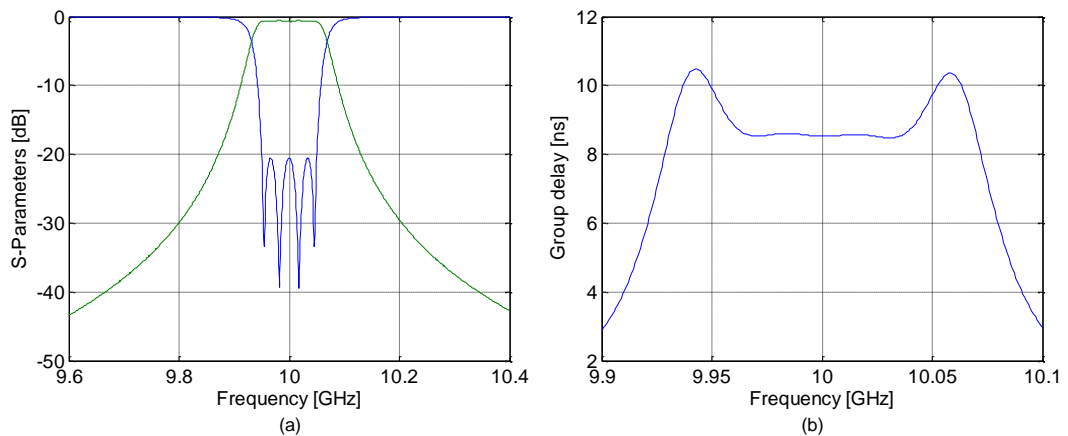
Figure 5.18: (a) Ideal frequency response and (b) Ideal group delay of fourth order SIW filter with transmission zeros at real axis (Chen et al., 2005:789)

Chen et al. (2009:674-683) proposed and analysed two different fourth order filters that uses cross couplings with nonphysical couplings, in which signal path is generated by high order modes. In this nonphysical method, cross couplings with nonphysical couplings are tuned by resonant frequencies of spurious resonance to generate finite transmission zeros far away from the passband for improved stopband performance. The geometric configurations of the two different fourth order filters are shown in Figure 5.19. The fourth order filter, with one oversized TE_{101}/TE_{201} SIW cavity and three oversized TE_{101}/TE_{301} SIW cavities, is shown in Figure 5.19(a), and one with two oversized TE_{101}/TE_{201} SIW cavities and two oversized TE_{101}/TE_{301} SIW cavities, is shown in Figure 5.19(b). The frequency responses of these SIW filters are presented in Chen et al. (2009:677-681). Each SIW cavity produce a transmission pole in the passband and a transmission zero at the desired location for producing sufficient stopband attenuation. In Chen et al. (2009:681), the frequency response of the SIW

filter with two oversized TE_{101}/TE_{201} SIW cavities and two oversized TE_{101}/TE_{301} SIW cavities shows the finite transmission zeros are generated far away from the passband and achieved a wide stopband attenuation that is better than 40 dB.

(a)   (b)
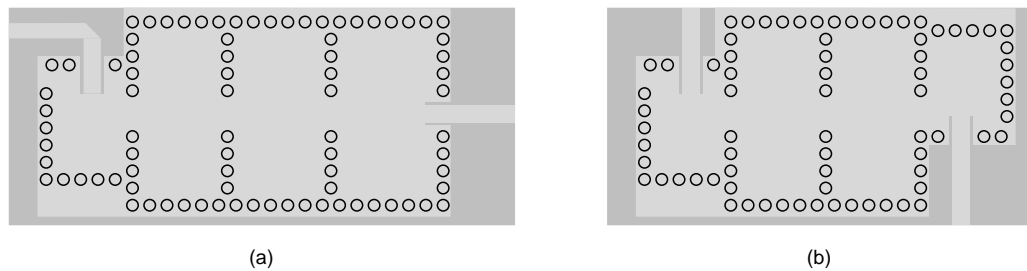
Figure 5.19: Fourth order filter with (a) three oversized TE $_{101}$/TE$_{301}$ cavities and one oversized TE$_{101}$/TE$_{201}$ SIW cavity, (b) two oversized TE$_{101}$/TE$_{201}$ SIW cavities and two oversized TE$_{101}$/TE$_{301}$ SIW cavities (Chen et al., 2009: 679-681)

The second technique makes use of the extracted pole technique to generate bandstop characteristics, where the finite transmission zeros on the imaginary axis is produced by bandstop resonant cavities that can also produce transmission poles in the passband. The bandstop resonant cavities are placed at intervals along the main transmission line carrying the signal but not in the signal path. A good example for this case is the SIW filter presented by Chen and Wu (2009b: 112-113), where extracted pole technique is used to synthesise a sixth order filter with non-resonating nodes (NRN).The two bandstop SIW cavity resonators which also produce transmission poles in the passband are used to generate two finite transmission zeros on the imaginary axis at ± j1.606 while other SIW cavities are used to generate two finite transmission zeros on the real axis at ± 1.0356 for flat in-band group delay. The geometric configuration and structural topology of the sixth order self-equalised pseudo-elliptical SIW filter which they have designed are shown in Figure 5.20. In Figure 5.20, SIW cavity resonators 1 and 6, which are not in the signal path, are bandstop SIW cavity resonators that are responsible for the generation of the two finite transmission zeros on the imaginary axis. The cross coupling between SIW resonators 2 and 5 is responsible for the generation of the two finite transmission zeros that are symmetrically located on the real axis to realise a linear phase response. The frequency responses of the measured and simulated results which show good agreement are presented in Chen and Wu (2009b:113).
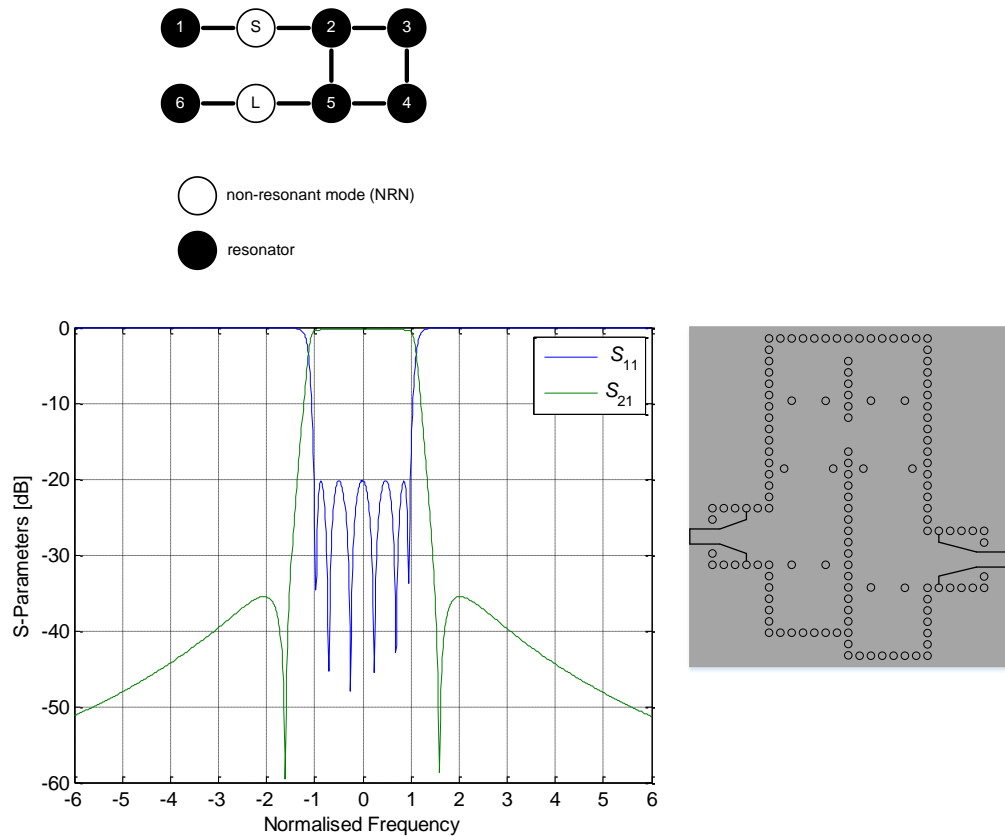
Figure 5.20: (a) Geometric configuration and structural topology of the sixth order self-equalised quasi-elliptic SIW filter (Chen & Wu, 2009b: 113)

Che et al. (2008:699-701) have proposed a SIW bandpass filter loaded with complementary split ring resonators (CSRRs) to produce sharp rejection stopband. Figure 5.21 illustrates the geometric configuration of the CSRRs on SIW filter with CSRR etched on the top surface. An CSRR provides a negative effective permittivity in the vicinity of its resonant frequency and produce a sharp rejection stopband, therefore the resonant frequency of CSRR can be set at the desired frequencies for transmission zeros. The resonant frequency of CSRR increases with the decrease of the inner radius (r) when the slit width is kept constant, while with the inner radius kept constant the resonant frequency of the CSRR will increase when the slit width (g) is increased thus the resonant frequency of the CSRR can be tuned to a defined location to produce sharp rejection stopband. They fabricated the proposed CSRR-SIW filter and its experimental results are presented in Che et al. (2008:701), which show the maximum rejection of 50 dB at the frequency band of 6.4 GHz to 7.8 GHz.
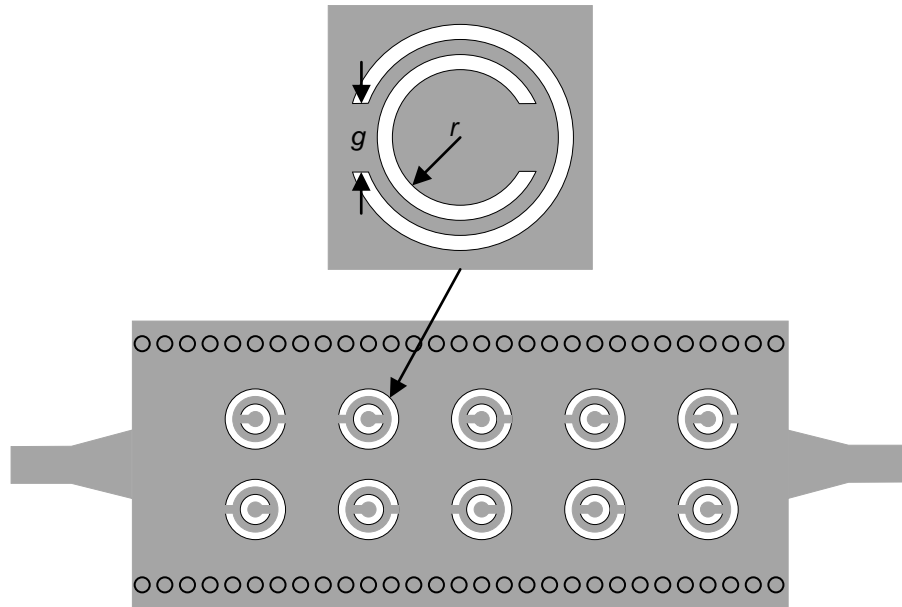
Figure 5.21: SIW bandpass filter loaded with complementary split ring resonators (Che et al. 2008 :700)

5.4   Coupled resonator filters

Coupled resonator circuits are suitable to design narrow band filters. The understanding of coupling and coupled mechanisms is very useful in the design of coupled resonator filters. The first step to design coupled resonator filters is to synthesize a low pass prototype which meets a given specification and also determine an appropriate coupling matrix M. Then the design parameters (coupling bandwidth, external quality factors and resonant frequencies of the resonators) are determined for dimensional synthesis. The coupling matrix that emerges from the synthesis procedure will have some entries that are non-zero and others with zero values. A non-zero entry in the coupling matrix M means coupling exists between those resonators.

The theory of the coupling matrixes and coupling coefficients has been presented in Chapter 2. The relation among the design parameters (normalised coupling coefficient M_{ij}, normal coupling coefficient k_{ij} and coupling bandwidths K_{ij}) discussed in Chapter 2 is given by equations in Table 5.2, where f_{0k} is the cavity resonance frequencies of the denormalised bandpass filter as given by Macchiarella and D'Oro (1998:181), f_0 is the passband centre frequency and BW is the bandwidth.

Table 5.2: Relation among design parameters

Normalised coupling coefficient M_{ij}	Normal coupling coefficient k_{ij}	Coupling bandwidth K_{ij}
$M_{S1}=\dfrac{1}{\sqrt{g_0 g_1}}$ $M_{i,i+1}=\dfrac{1}{\sqrt{g_i g_{i+1}}}, \quad \text{for } 1\leq i \leq N-1$ $M_{NL}=\dfrac{1}{\sqrt{g_N g_{N+1}}}$	$Q_{e(s)}=\dfrac{f_0}{M_{S1}^2 BW}=\dfrac{f_0}{K_{S1}}$ $k_{ij}=M_{ij}\dfrac{BW}{f_0}$ $Q_{e(L)}=\dfrac{f_0}{M_{NL}^2 BW}=\dfrac{f_0}{K_{NL}}$	$K_{S1}=M_{S1}^2 BW$ $K_{ij}=M_{ij}BW$ $K_{NL}=M_{NL}^2 BW$ $f_{0,k}=f_0\left\{\sqrt{\left(\dfrac{BW}{2f_0}M_{kk}\right)^2+1}-\left(\dfrac{BW}{2f_0}M_{kk}\right)\right\}$

5.4.1 External coupling

External couplings are couplings that connect the filter to the outside world and are usually expressed as external quality factors. The concept of an external quality factor is illustrated in Figure 5.22 with the single SIW cavity resonator coupled to the 50 Ω microstrip line as its input/output port. The external quality factor is determined by simulating the cavity resonator using an electromagnetic simulator. The coupling is controlled by changing the length and width of the coupling slot. The 50 Ω microstrip line coupled to the cavity resonator permit the measurement of the transmission characteristic S_{21} shown in Figure 5.22.
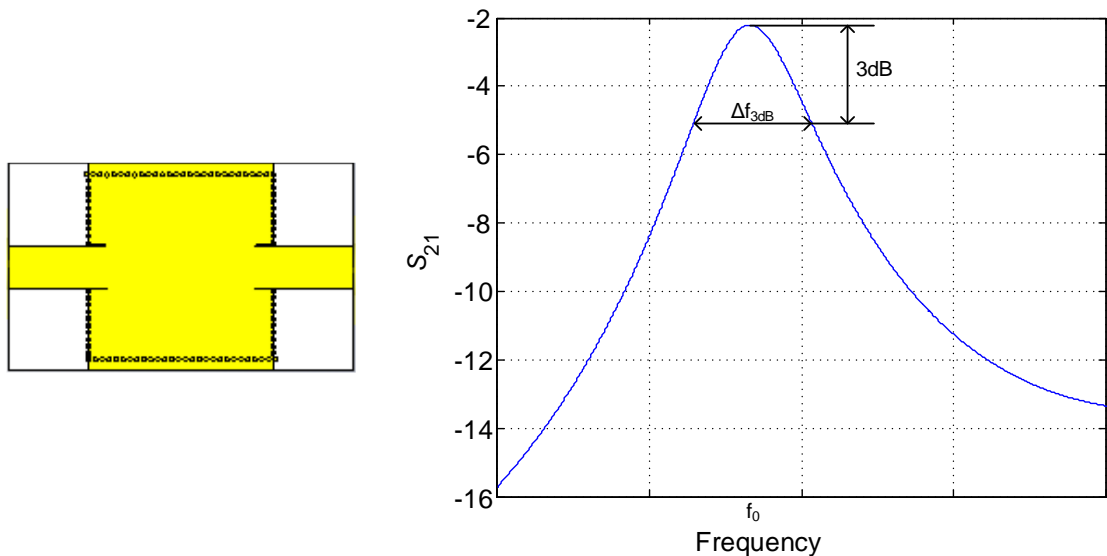
Figure 5.22: Single SIW cavity resonator and its transmission characteristic.

The external coupling is obtained by measuring the 3 dB bandwidth of the resonance curve for which S_{21} is reduced by 3 dB from its maximum value. The external quality factor is then calculated by $Q_e = f_0/\Delta_{3dB}$, where f_0 is the frequency at which S_{21} reaches its maximum value and Δ_{3dB} is the 3 dB bandwidth for which S_{21} is reduced by 3 dB from its maximum value. Alternatively, external quality factor can also be expressed by normalised coupling coefficient M_{S1} or coupling bandwidth K_{S1} as given in Table 5.2, where BW is the ripple bandwidth of the filter. From the equations in Table 5.2, it can be noted that wide bandwidth corresponds to low external quality factor and hence a strong coupling.

5.4.2 Internal coupling

The concept of coupling between adjacent cavity resonators is demonstrated in Figure 5.23 by a pair of coupled SIW cavity resonators with input and output ports simulated using an electromagnetic simulator. The corresponding transmission characteristic S_{21} is also shown in Figure 5.23 with two split resonant-mode frequencies that are identified by two resonant peaks.
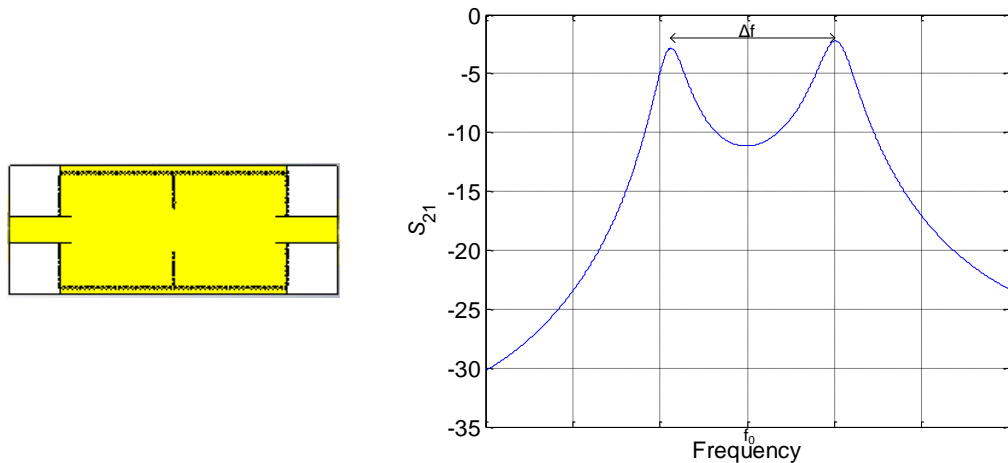
Figure 5.23: A pair of coupled SIW cavity resonators and its transmission characteristic

The coupling between the two SIW cavity resonators is controlled by the width of the post wall iris w_i. The coupling between the two identical SIW cavity resonators that are both resonating at frequency f_0, results in a displacement of the resonance frequency Δ_f referred to as coupling bandwidth K_{ij}. From the equations in Table 5.2, it can be noted that when the coupling bandwidth K_{ij} is divided by the ripple bandwidth BW of the filter, a normalised coupling coefficient M_{ij} is obtained.

5.4.3 Cross coupling

Cross coupling between non-adjacent cavity resonators are used to bring up transmission zeros from infinity to finite position in the complex plane. It is either used to introduce transmission zero in the stopband for increased skirt selectivity or to equalise the group delay in the passband. Couplings are either negative or positive and are usually schematically represented as shown in Figure 5.24.
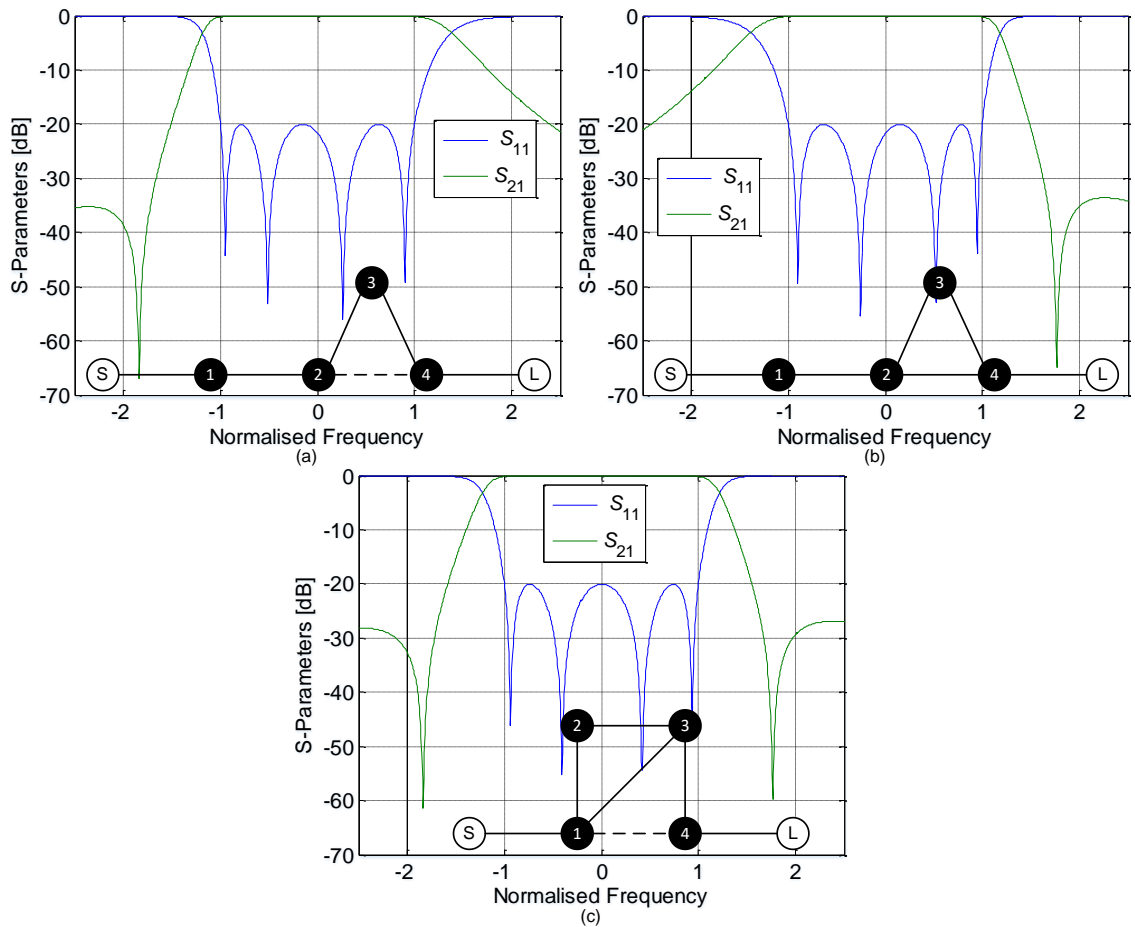
Figure 5.24: Frequency response and its topology with (a) negative cross coupling, (b) positive cross coupling and (c) negative and positive cross coupling

In the schematic topology in Figure 5.24, the black dots represent the resonators, the white circles represent source/load, the broken lines represent capacitive coupling and the solid lines represent inductive coupling. Capacitive couplings are negative while inductive couplings are positive. In Figure 5.24, it can be noted that negative coupling produces transmission zero below the passband while positive coupling produces transmission zero above the passband.

5.5   Summary

Several miniaturising techniques such as HMSIW and FSIW are used to reduce the size of an SIW with limited impact on the performance. Tang et al. (2007:777) studied the unloaded quality factor of the different shapes of SIW cavities and they concluded that the circular and elliptic cavity have a slightly higher quality factor than that of the square cavity. SIW filter cavities are either defined by iris window or inductive post. Cross coupling between non-adjacent cavity resonators are used to introduce transmission zeros in the stopband. Couplings are either positive or negative. Negative coupling produces transmission zeros below the passband and positive coupling produces transmission zeros above the passband.

CHAPTER 6. X-BAND FILTER DESIGN, MODELLING AND SIMULATED RESULTS

6.1 Introduction

The technical literature review was presented in the previous chapters. This chapter discusses the methods used to design the three SIW filters. There are two basic approaches used to design the SIW filters presented in this chapter: the first design method used is based on the calculations of the Chebyshev g values from the specifications, followed by the computation of the coupling bandwidth of the coupled resonator filter from the Chebyshev g values. The second method involves generation of the transfer and reflection polynomials from the prescribed transmission zeros, followed by the calculation of coupling element values from the transfer and reflection polynomials. Two SIW filters are designed and their simulated frequency response are presented in this chapter. The filters are simulated with Computer Simulation Technology (CST) Microwave Studio Suite®, then the simulated results presented in this chapter are compared with the measured results in Chapter 7.

6.2 First filter design method and modelling

The design approach used is based on the synthesis of the low pass prototype that meets the specifications and also determines an appropriate coupling matrix from the Chebyshev g values, and then calculates the design parameters by denormalising the coupling matrix. The eigenmode Solver in CST Microwave Studio is used to tune the single cavity for the required resonance frequency, then tune inter-resonator coupling for coupling bandwidth and external coupling for external quality factors. The complete structure is optimised and simulated using the frequency domain solver in CST Microwave Studio.

The design steps used to design the SIW filter are:

- **(a)** Obtain a low-pass prototype from the filter specification.
- **(b)** Determination of the coupling matrix from the low-pass prototype elements.
- **(c)** Calculation of the design parameters.
- **(d)** Using the CST filter design 3D tool to analyse the filter.
- **(e)** The Eigenmode Solver in CST microwave studio is used to tune first a single cavity for the resonant frequency, then tune inter-resonator coupling for coupling bandwidth and external coupling for external quality factors.
- **(f)** The frequency domain solver in CST Microwave Studio is used to simulate and optimise the filter.

6.2.1 Obtain low-pass prototype from specification

The filter specification is outlined in Section 1.4, with the passband bandwidth equal to 500 MHz, resonant frequency of 8.2462 GHz, S_{11} less than −12 dB over the transmitting band. The return loss of 25 dB is aimed at instead of the minimum required return loss of 12 dB.

With the target return loss (l_r) of 25 dB, Equations 2.3 to 2.5 on page 12 are used to calculate Chebyshev g values shown in Table 6.1 up to N equal to 6 using MATLAB. The stopband insertion loss of 30 dB is used to determine the filter order (N) from the chart of 0.01 dB ripple (l_{ripple}) Chebyshev filter in Figure 2.5 by using Equation 2.10. A fourth-order filter (N=4) with its low-pass prototype filter shown in Figure 6.1 is found to be suitable to meet the required insertion loss at the stop band.

Table 6.1: *g* values of a Chebyshev filter with 25 dB return loss

N	g0	g1	g2	g3	g4	g5	g6	g7
1	1	0.112652	1					
2	1	0.488213	0.436226	1.119176				
3	1	0.670353	1.002750	0.670353	1			
4	1	0.753323	1.225207	1.371222	0.673105	1.119176		
5	1	0.796059	1.324762	1.620666	1.324762	0.796059	1	
6	1	0.820554	1.376850	1.728526	1.544462	1.540938	0.733177	1.119176
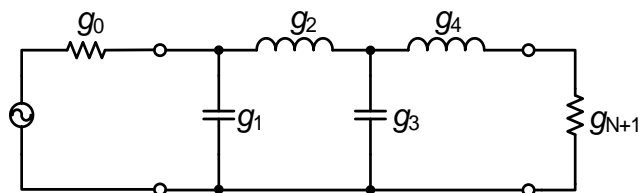
Figure 6.1: Low-pass prototype

6.2.2 Determination of the coupling matrix from low-pass prototype *g* values

The bandpass filter shown in Figure 6.2 uses shunt inductive coupling between resonators that operates similar to the filter with series resonators and impedance inverters shown in Figure 2.13 on page 29.
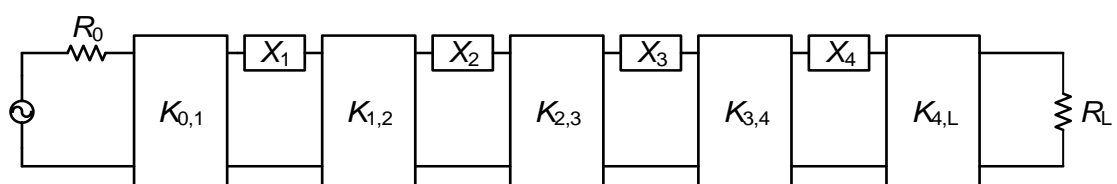
Figure 6.2: Bandpass filter as series resonators with impedance inverters

The normalised coupling matrix *M* given below is obtained by using equations in Table 5.2 on page 84 with *g* values of the 4th-order filter given in Table 6.1 above.

	S	1	2	3	4	L
S	0	1.1522	0	0	0	0
1	1.1522	0	1.0409	0	0	0
2	0	1.0409	0	0.7715	0	0
3	0	0	0.7715	0	1.0409	0
4	0	0	0	1.0409	0	1.1522
L	0	0	0	0	1.1522	0

Figure 6.3: Normalised coupling matrix M and schematic topology of the fourth order filter without transmission zeros

In the normalized coupling matrix in Figure 6.3, it can be seen since the filter does not have cross couplings, all the couplings are positive and the elements in the self-couplings in the main diagonal which represents the resonance frequencies of the individual resonators are all zero. This indicates that all the resonators are tuned to the centre frequency of the filter.

6.2.3 Calculation of the design parameters

The following design parameters for dimensional synthesis are obtained by denormalising the normalised coupling matrix in Figure 6.3 above. The coupling bandwidths are calculated using equations in Table 5.2 on page 84.

$K_{S1} = K_{4L} = 663.73$ MHz

$K_{12} = K_{34} = 520.44$ MHz

$K_{23} = 385.75$ MHz

$f_{0k} = K_{11} = K_{22} = K_{33} = K_{44} = 8246$ MHz

$Q_{(ext)S,1} = Q_{(ext)4,L} = 12.43$

It can be noted from the calculated design parameters that the filter characteristics is symmetric since the resonance frequencies of the resonators are all at 8.246 GHz.

6.2.4 Using CST filter design 3D to analyse the filter

The CST filter design 3D synthesis tool is used to tune the filter by producing a realistic coupled resonator topology with its coupling matrix as illustrated in Figure 6.4. The filter report in Figure 6.4 also gives the coupling matrix, coupling bandwidths and external quality factors which are in good agreement with the ones calculated in Section 6.2.3 above.

Normalized Matrix Elements
$m_{1,1} = 0.0$
$m_{2,2} = 0.0$
$m_{3,3} = 0.0$
$m_{4,4} = 0.0$
$m_{5,1} = m_{1,5} = 1.15216$
$m_{1,2} = m_{2,1} = 1.0409$
$m_{2,3} = m_{3,2} = 0.771517$
$m_{3,4} = m_{4,3} = 1.0409$
$m_{4,L} = m_{L,4} = 1.15216$

Resonance Frequencies
$f_1 = 8246.211251$ MHz
$f_2 = 8246.211251$ MHz
$f_3 = 8246.211251$ MHz
$f_4 = 8246.211251$ MHz

S ◆ ● ● ● ● L

	S	1	2	3	4	L
S	0.0	1.152161679	0.0	0.0	0.0	0.0
1	1.152161679	0.0	1.040902505	0.0	0.0	0.0
2	0.0	1.040902505	0.0	0.7715166246	0.0	0.0
3	0.0	0.0	0.7715166246	0.0	1.040902505	0.0
4	0.0	0.0	0.0	1.040902505	0.0	1.152161679
L	0.0	0.0	0.0	0.0	1.152161679	0.0

Coupling Bandwidth
$CBW_{S,1} = 663.738$ MHz
$CBW_{1,2} = 520.451$ MHz
$CBW_{2,3} = 385.758$ MHz
$CBW_{3,4} = 520.451$ MHz
$CBW_{4,L} = 663.738$ MHz

External Quality Factors
$Q_{S,1} = 12.4239$
$Q_{4,L} = 12.4239$

Figure 6.4: Direct coupled resonator topology and coupling bandwidths produced with CST filter design 3D tool

6.2.5 Using Eigenmode Solver in CST microwave studio to tune the filter

The single SIW cavity is designed using Equation 6.1 which is related to Equation 3.11 and Equation 4.2 where C_0 is the speed of the light in the air, $w_{eff} = w - \frac{d^2}{0.95p}$, $l_{eff} = l - \frac{d^2}{0.95p}$ and where w and l are the geometric dimensions of the SIW cavity.

$$f_0 = \frac{C_0}{2\sqrt{\varepsilon_r}}\sqrt{\left(\frac{1}{w_{eff}}\right)^2 + \left(\frac{1}{l_{eff}}\right)^2} \qquad 6.1$$

The filter is designed on a Substrate Rogers RO4003C™ with a thickness of 1.524 mm. The width of the 50 Ω microstrip line is calculated using the Equations 6.2 and 6.3 given by Hammerstad (1975:269). The 50 Ω microstrip line is needed in the filter, as the VNA used to measure the filter needs to be connected to a 50 Ω transmission line.

$$B = \frac{376.73\pi}{2Z_0\sqrt{\varepsilon_r}} \qquad 6.2$$

$$\frac{w}{h} = \frac{2}{\pi} \left[B\text{-}1\text{-}\ln(2B\text{-}1) + \frac{\varepsilon_r\text{-}1}{2\varepsilon_r} \left\{ \ln(B\text{-}1) + 0.39\text{-}\frac{0.61}{\varepsilon_r} \right\} \right], \; {}^{w}\!/_{h} \geq 2$$

<div align="right">6.3</div>

With the diameter (d) equal to 0.6 mm, design dielectric constant (ε_r) equal to 3.55, the spacing between vias (p) equal to 0.9mm and the resonant frequency equal to 8.25 GHz, the SIW dimensions are calculated to be 14.07 mm by 14.07mm using Equation 6.1. The dimensions of the SIW cavity are the design parameters that determine the resonant frequency; hence a parameter sweep over the range of the dimensions of the SIW cavity shown in Figure 6.6 produced a curve illustrated in Figure 6.5 that relates cavity dimension to the resonant frequency.
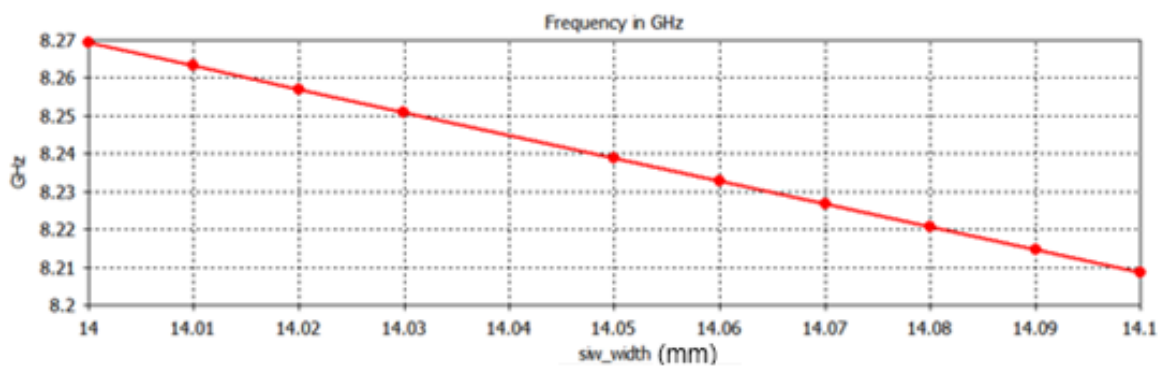
Figure 6.5: Results of parameter sweep over SIW cavity dimensions, plotting resonant frequency versus the dimensions of the SIW cavity

The above curve in Figure 6.5 is used to read the SIW dimensions required to produce the resonant frequency of 8.25 GHz. Using the values from the graph in Figure 6.5 as the initial SIW resonator dimensions, the SIW resonator is tuned to the resonant frequency of 8.25 GHz using the CST Eigenmode Solver by setting the dimensions of the SIW cavity to 14.03 mm by 14.03 mm. The electric field distributions in the SIW cavity with the dimensions of 14.03 mm by 14.03 mm show that the cavity supports more than one mode, the fundamental mode, TE_{101} at 8.25GHz, and the high-order mode, TE_{102} at 13.01 GHz, as illustrated in Figure 6.6(a) and (b) respectively.
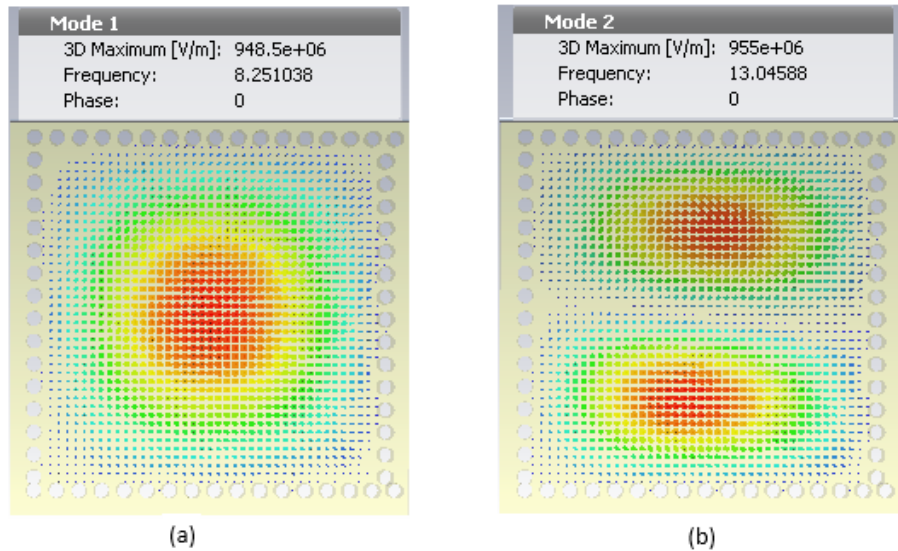
Figure 6.6: Electric field distribution in the SIW cavity (a) Fundamental mode TE$_{101}$ and (b) Higher order mode TE$_{102}$

The next step is to plot the design curve shown in Figure 6.7 that relates the via-free gap to the coupling bandwidth (CBW), with the table showing the via-free gap that has been optimised to match the required CBW of each pair of SIW resonators. The coupling bandwidth that represents the coupling between each pair of SIW cavities is calculated in Section 6.2.3 above and also in the CST filter design 3D tool as shown in Figure 6.4. The electromagnetic signal is coupled from the first SIW cavity into the next SIW cavity by the via-free gap as illustrated in Figure 6.7.

Resonator	Required CBW (MHz)	Via-free gap (mm)
1-2	520.451	6.474
2-3	385.758	5.75
3-4	520.451	6.474
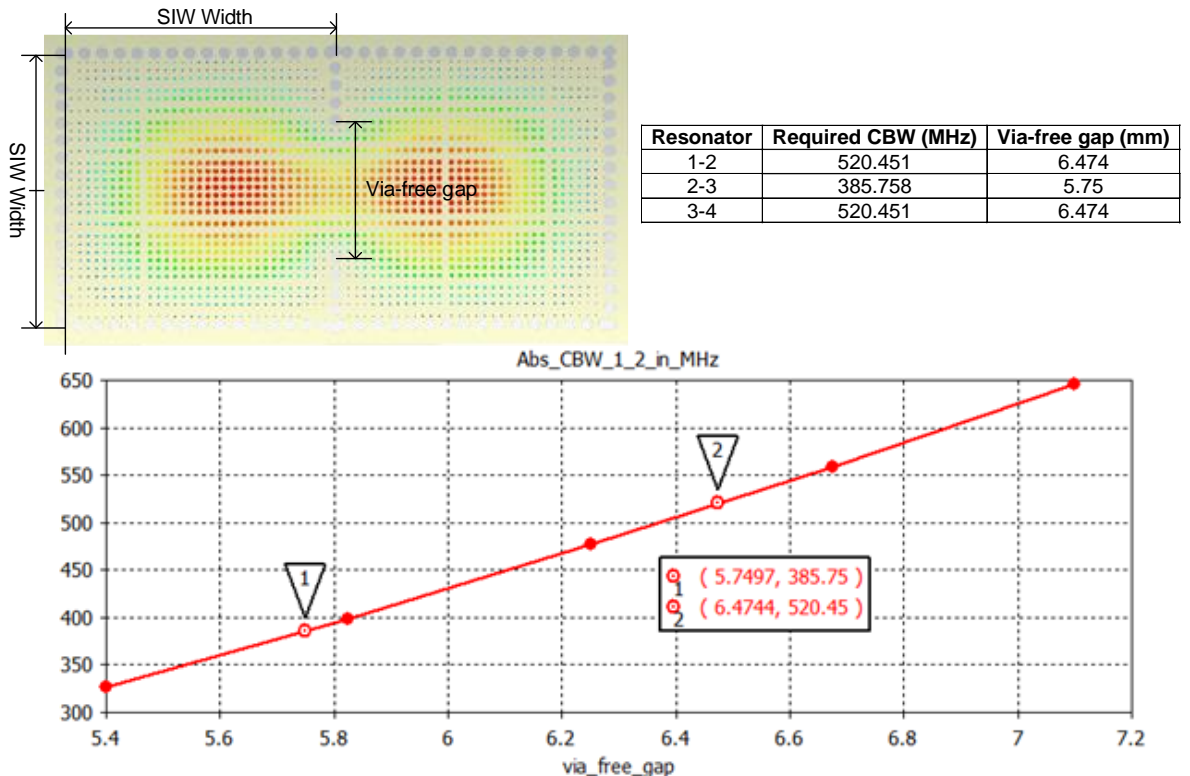
Figure 6.7: Design curve for inter-coupling, relating CBW to the via-free gap

The energy coupled into the first SIW cavity is determined by the external quality factor (Q_{ext}). The SIW cavity is excited through the 50 Ω microstrip line as illustrated in Figure 6.8. The via-free gap that couples the 50 Ω microstrip line to the SIW cavity is parametised in order to match the required Q_{ext} calculated in Section 6.2.3. The design curve that relates the external quality factors to the via-free gap is plotted as illustrated in Figure 6.8, with the table showing the optimised gap to match the required Q_{ext}.

	Required external Q factor	Via-free gap(mm)
$Q_{s,1}$	12.433	4.23
$Q_{4,L}$	12.433	4.23
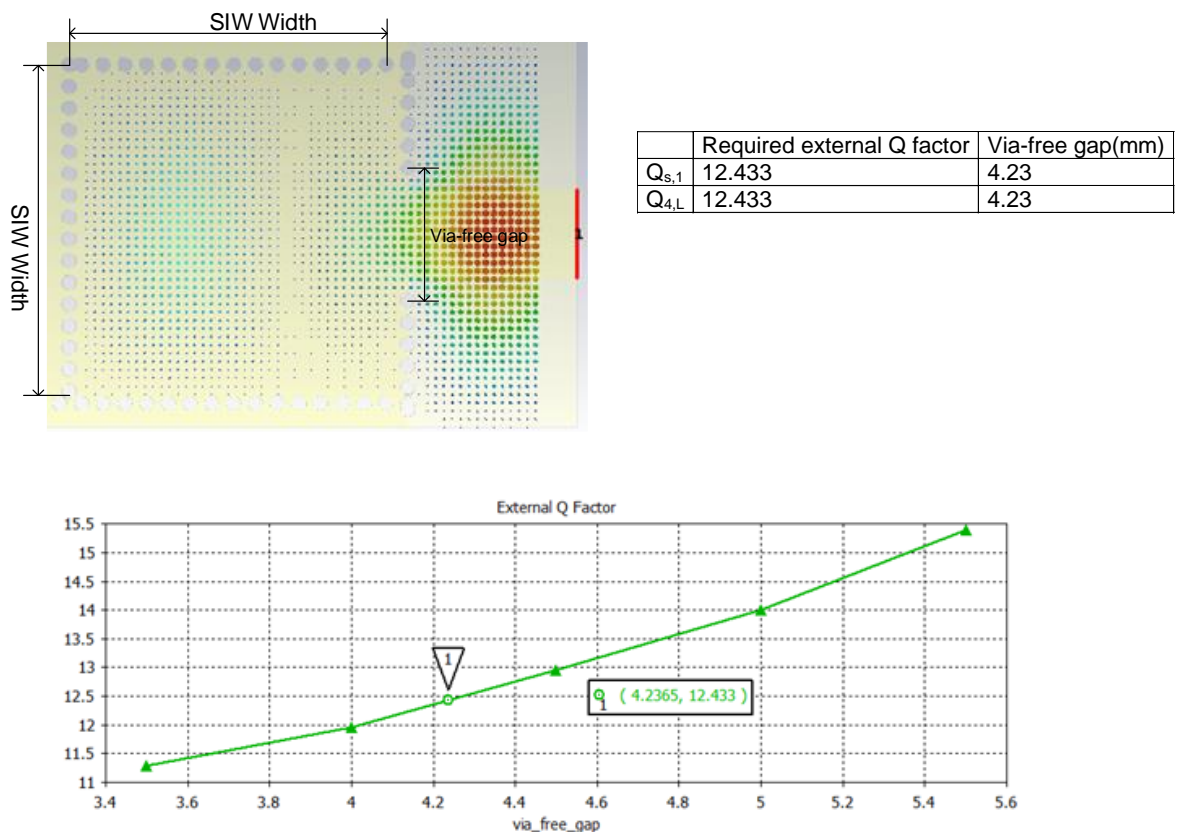
Figure 6.8: Design curve for external coupling, relating external quality factor to the via-free gap

6.2.6 Tuning the SIW filter using CST Microwave Studio

The individual pairs of SIW cavities computed in Section 6.2.5 above are assembled to form an SIW filter as shown in Figure 6.9. The frequency response behaviour of the SIW filter shown in Figure 6.9 is not as expected due to coupling detuning; there is a frequency shift in the passband to the lower frequencies, bad insertion loss and poor return loss in the passband.
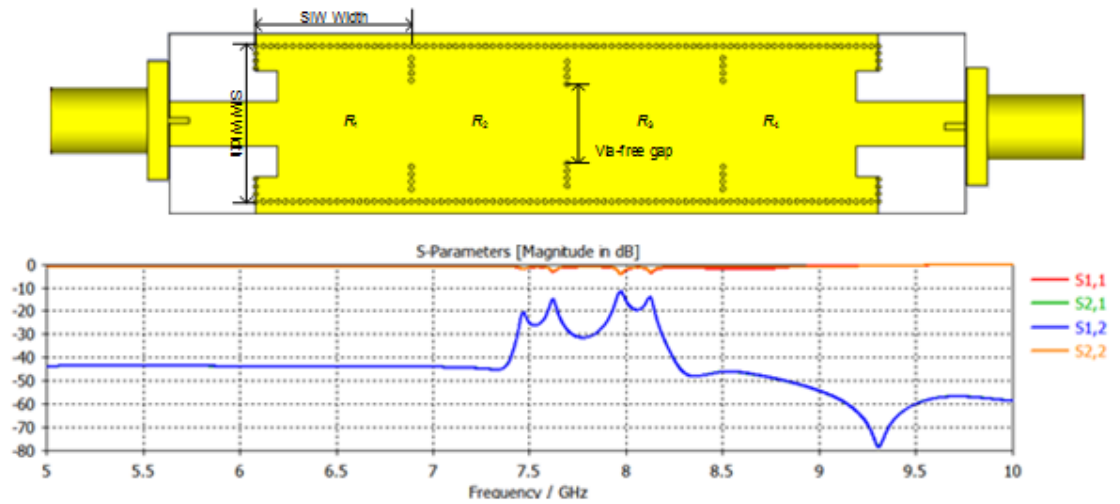
	Required external Q factor	Required CBW (MHz)	Via-free gap (mm)	Parameters of the SIW resonator	
$Q_{S,1}$	12.433		4.22	SIW resonator width	14.3 mm
$CBW_{1,2}$		520.451	6.475	Via diameter	0.6 mm
$CBW_{2,3}$		385.758	5.748	Via spacing	0.9 mm
$CBW_{3,4}$		520.451	6.475		
$Q_{4,L}$	12.433		4.22		

Figure 6.9: S-parameters of the SIW filter before tuning

The frequency shift in the passband is rectified by decreasing the width of the SIW resonator. The SIW filter is fine-tuned and optimised to improve the insertion loss and return loss. The parameters of the SIW filter are tuned and optimised to the new values as shown in Figure 6.10 to produce the required frequency response. The SIW filter model is named Filter 1, and its frequency response is illustrated in Figure 6.10 with the new optimised parameters of the filter.

Coupling	Via-free gap (mm)
S−1	8.4
1−2	7.11
2−3	6.34
3−4	7.11
4−L	8.4

Parameters of the SIW resonator	
SIW resonator width	12.7 mm
Via diameter	0.4 mm
Via spacing	0.6 mm
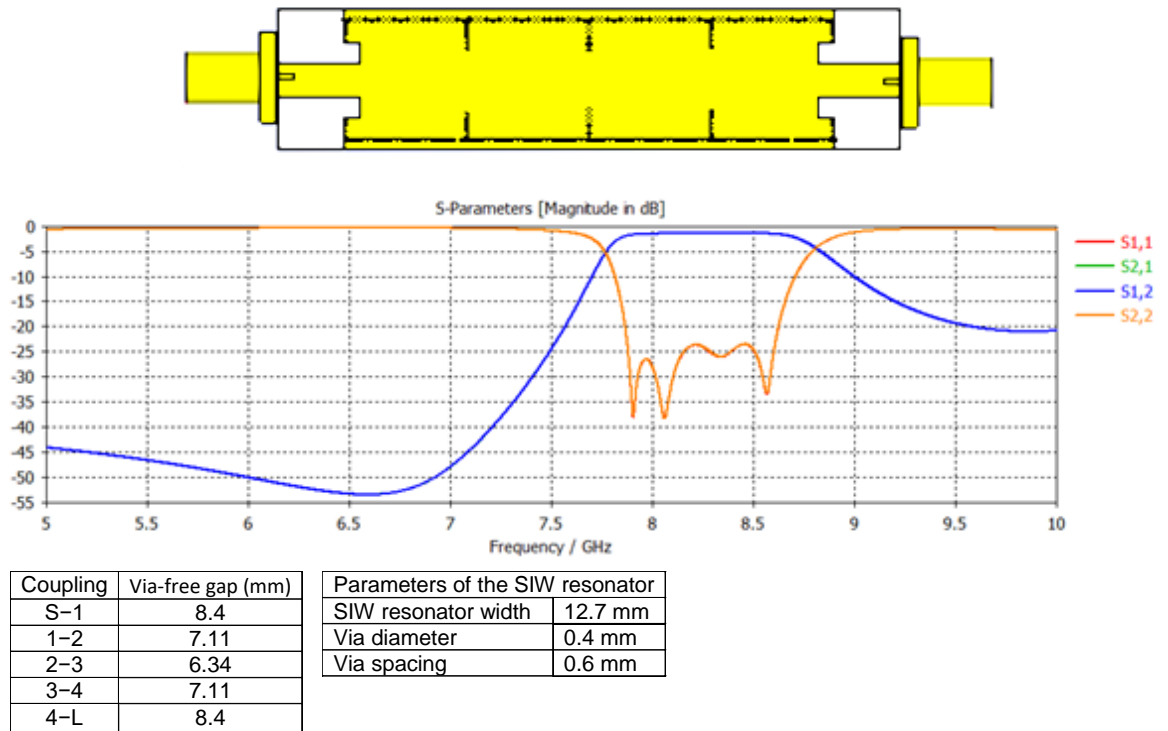
Figure 6.10: Structure and simulated results of Filter 1

6.3   X-band filter design and synthesis

The filter design process starts with the given filter specification with a goal to find a physical realisation that can fulfil the requirements. The design methodology used to design the SIW filter with transmission zeros is divided into two categories.

1. The filter synthesis, which concentrates on the derivation of characteristic polynomials which represents the transfer and reflection characteristics (S_{21} and S_{11}) to satisfy the rejection and in-band specification of the filter and the corresponding coupling matrix to obtain design parameters.

2. The filter realisation which concentrates on the realisation of the physical network.

The design methodology used is illustrated in figures 6.11 and 6.12. In this design methodology, Matlab is used to calculate and plot parameters used in the filter design process, while CST Microwave Studio is used for EM simulation. Matlab code used in this filter design is given in appendices A and B.
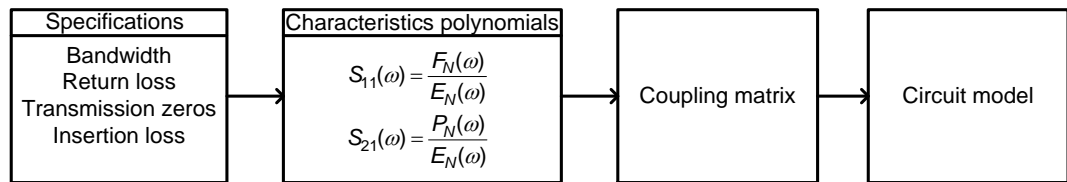
Figure 6.11: Filter synthesis process
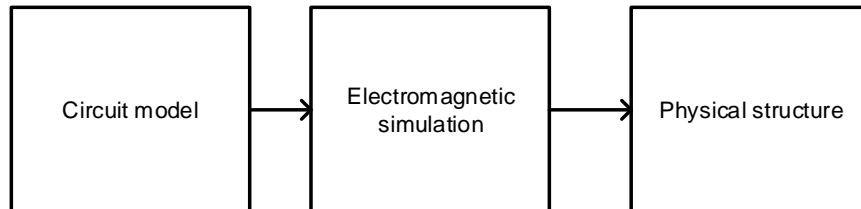
Figure 6.12: Filter realisation process

6.3.1 Filter synthesis

The filter specification outlined in Section 1.4 is summarised in the Table 6.2 for the fourth order SIW filter.

Table 6.2: Summarised SIW filter specifications

	Frequency (GHz)	Normalised frequency
Prescribed transmission zeros	7	-j5.4286
	5.8	-j11.843
Lower cutoff frequency	8	-j1
Upper cutoff frequency	8.5	j1
Centre frequency	8.2462	0
Return loss= 25 dB		

The prescribed frequencies in Table 6.2 are normalised using Equation 2.10 on page 16. The recursive technique outlined in Section 2.4 is applied and gives reflection zeros, transmission/reflection poles and in-band reflection maxima given in Table 6.3. Equations 2.30 to 2.33 are used to find reflection zeros and in-band reflection maxima. The transmission/reflection poles are found by rooting each term on the right-hand side of Equation 2.34. The pattern of the roots of $E(s)E(s)^*$ as in Equation 2.34 are plotted in Figure 6.13 using Matlab. The roots of $E(s)E(s)^*$ that are in the left-half plane belong to $E(s)$ since roots of $E(s)$ are strictly Hurwitz and those in the right-half plane belong

to $E(s)^*$. The value of ε_r is equal to 1 for partially canonical ($N \neq n_{fz}$) and the value of the constant ε is calculated using Equation 2.12.
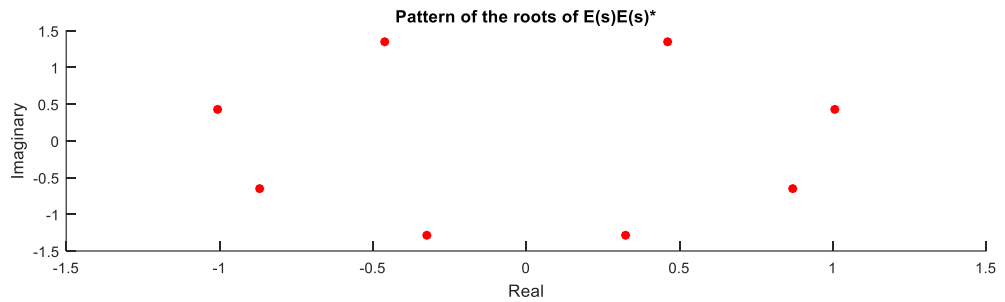
Figure 6.13: Pattern of the roots of E(s) E(s)* in the complex plane

Table 6.3: Singularities of the fourth order filter with two prescribed transmission zeros

Transmission zeros	Reflection zeros (roots of $F_4(s)$)	Transmission/ reflection poles (roots of $E_4(s)$)	In-band reflection maxima (roots of $V_4(s)$)
-j11.8483	-j0.9336	-0.3222-j1.2782	-j0.7403
-j5.4286	-j0.4398	-0.8679-j0.6496	-j0.0676
$j\infty$	j0.3245	-1.0064+j0.4355	j0.6727
$j\infty$	j0.9138	-0.4606+j1.3571	
ε=28.6821	ε_r=1		

With transmission/reflection poles, transmission and reflection zeros determined as listed in Table 6.3, the polynomials E(s), P(s) and F(s) are also determined and their coefficients normalised to the highest degree are given in Table 6.4. Since (N-n_{fz}) is an even number, the coefficients of polynomial $P(s)$ are multiplied by j to ensure orthogonality between F(s) and P(s) vectors.

Table 6.4: Coefficients of E(s), F(s) and P(s) Polynomials

s^i i	Coefficients of S_{11} and S_{21} Denominator Polynomial E(s)	Coefficients of S_{11} Numerator Polynomial F(s)	Coefficients of S_{21} Numerator Polynomial P(s)
0	2.1357 + j0.6945	0.1217	-j64.3192
1	4.4239 + j0.8117	j0.1012	-17.2768
2	4.5235 + j0.4470	0.9935	j1
3	2.6571 + j0.1352	j0.1352	
4	1	1	
		ε_r=1	ε=28.6821

With the polynomials $E(s)$, $F(s)$ and $P(s)$ calculated and given in Table 6.4, Equation 2.11 is used to plot the transfer and reflection characteristics (S_{21} and S_{11}) of the prototype filter in Figure 6.14 using Matlab. Figure 6.14 indicate that the reflection zeros and in-band reflection maxima correspond with the calculated ones in Table 6.3, and

also indicate that the transmission zeros are at the prescribed location (-j11.843 and -j5.4286) as tabulated in Table 6.3.
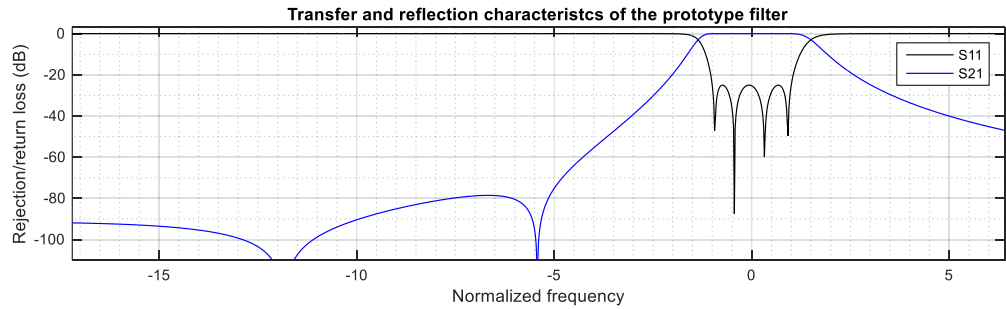
Figure 6.14: Transfer and reflection characteristics of the prototype filter

With the transfer and reflection characteristics determined, the numerator and denominator polynomials of $y_{21}(s) = y_{21n}(s)/y_d(s)$ and $y_{22}(s) = y_{22n}(s)/y_d(s)$ are constructed using equations 2.35, 2.37 and 2.38 for N is even. The coefficients of numerator and denominator polynomials of $y_{21}(s)$ and $y_{22}(s)$ normalised to the highest degree coefficient of $y_d(s)$ are listed in Table 6.5.

Table 6.5: Coefficients of numerator and denominator Polynomials $y_{21}(s)$ and $y_{22}(s)$

s^i i	Coefficients of Denominator Polynomial of $y_{21}(s)$ and $y_{22}(s)$ ($y_d(s)$)	Coefficients of Numerator Polynomial of $y_{22}(s)$ ($y_{22n}(s)$)	Coefficients of Numerator Polynomial of $y_{21}(s)$ ($y_{21n}(s)$)
0	1.1287	j0.3472	$-j$1.1212
1	j0.4565	2.2120	-0.3012
2	2.7585	j0.2235	j0.0174
3	j0.1352	1.3285	
4	1		

The associated residues r_{21k} and r_{22k} of $y_{21}(s)$ and $y_{22}(s)$ are found with partial fraction expansion or Equations 2.40 and 2.41, respectively. The eigenvalues λ_k are determined by finding the roots of $y_d(s)$ and then multiply them by $-j$. The eigenvectors T_{1k} and T_{Nk} which are the input couplings (M_{sk}) and output couplings (M_{Lk}) respectively are

determined using Equation 2.48. The determined eigenvalues λ_k and eigenvectors T_{1k} and T_{Nk} are listed in Table 6.6.

Table 6.6: The calculated eigenvalues, residues and eigenvectors

k	Eigenvalues	Residues		Eigenvectors	
	λ_k	r_{22k}	r_{21k}	$T_{Nk}=\sqrt{r_{22k}}$	$T_{1k}=r_{21k}/\sqrt{r_{22k}}$
1	-1.4502	0.1897	-0.1897	0.4355	-0.4355
2	-0.8322	0.4183	0.4183	0.6468	0.6468
3	0.6075	0.4746	-0.4746	0.6889	-0.6889
4	1.5397	0.2460	0.2460	0.4960	0.4960

The values of the eigenvalues λ_k represent the self-couplings M_{11} to M_{NN} as stated by Equation 2.47 and eigenvectors T_{1k} and T_{Nk} represent input couplings (M_{Sk}) and output couplings (M_{Lk}) respectively as defined in Equation 2.48. The source to load coupling (M_{SL}) is zero for partial canonical function ($n_{fz} < N$) for the transversal array of a N coupled resonator filter shown in Figure 2.9. With the calculated values of the self-couplings M_{11} to M_{NN}, input couplings M_{Sk} and output couplings M_{Lk}, and source to load coupling M_{SL}, the $N+2$ transversal coupling matrix is completed as shown in the table below.

Table 6.7: Calculated transversal coupling matrix for the filtering function

	S	1	2	3	4	L
S	0	-0.4355	0.6467	-0.6889	0.4960	0
1	-0.4355	1.4502	0	0	0	0.4355
2	0.6467	0	0.8322	0	0	0.6467
3	-0.6889	0	0	-0.6075	0	0.6889
4	0.4960	0	0	0	-1.5397	0.490
L	0	0.4355	0.6467	0.6889	0.4960	0

Since the transversal topology is impractical to realise, the transversal coupling matrix in Table 6.7 is transformed to the coupling matrix of the folded network using the procedure outlined in Section 2.5 with the series of rotations given in Table 6.8. The Matlab code with rotation sequence in Table 6.8 for the reduction of transversal coupling matrix to the folded configuration is given in Appendix B. The resulting coupling matrix M and its topology is shown in Figure 6.15.

Table 6.8: Rotation sequence for reduction of the transversal coupling matrix

Transform number r	Pivot [i, j]	Element to be annihilated	$\theta_r = \tan^{-1}(cM_{kl}/M_{mn})$				
			c	k	l	m	n
1	[3,4]	M_{S4} in row S	-1	S	4	S	3
2	[2,3]	M_{S3} in row S	-1	S	3	S	2
3	[1,2]	M_{S2} in row S	-1	S	2	S	1
4	[2,3]	M_{2L} in column L	1	2	L	3	L
5	[3,4]	M_{3L} in column L	1	3	L	4	L
6	[2,3]	M_{13} in row 1	-1	1	3	1	2

	S	1	2	3	4	L
S	0	1.1526	0	0	0	0
1	1.1526	-0.0331	1.0430	0	0.0132	0
2	0	1.0430	-0.0562	0.7456	-0.2148	0
3	0	0	0.7456	0.2577	1.0206	0
4	0	0.0132	-0.2148	1.0206	-0.0331	1.1526
L	0	0	0	0	1.1526	0
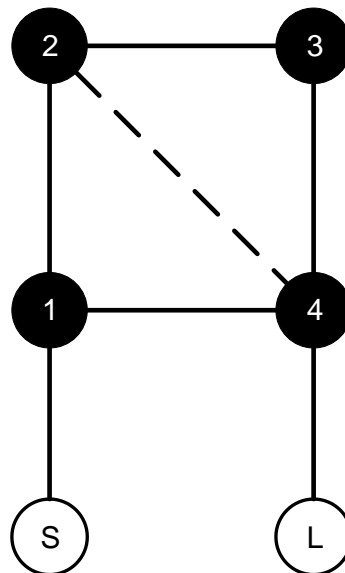
Figure 6.15: Normalised coupling matrix M and its folded structural topology

The technique presented in Cameron et al. (2018:350-356) for reducing transversal coupling matrix to cascaded tuplets was also used. This is accomplished by performing a sequence of matrix rotations similar to those outlined in Section 2.5 to convert the

transversal coupling to the arrow form, then using associated transmission zero to create and position trisection. The trisections are then reconfigured to the cascaded tuplets. When the transversal coupling matrix in Table 6.7 is reduced using this technique, it yields to the same values of the coupling matrix as given in Figure 6.15.

	S	1	2	3	4	L
S	0	1.1526	0	0	0	0
1	1.1526	-0.0331	1.0430	0	0.0132	0
2	0	1.0430	-0.0562	0.7456	-0.2148	0
3	0	0	0.7456	0.2577	1.0206	0
4	0	0.0132	-0.2148	1.0206	-0.0331	1.1526
L	0	0	0	0	1.1526	0
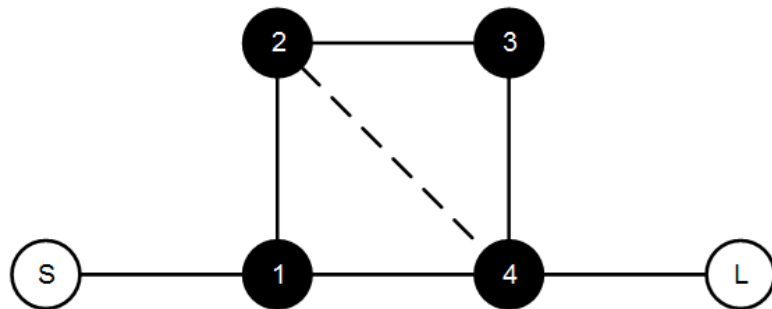
Figure 6.16: Normalised coupling matrix M and its structural topology

In the normalised coupling matrix in Figure 6.15 and Figure 6.16, it can be seen that all the couplings are positive except the cross coupling between resonators 2 and 4 which is negative and the elements in the self-couplings in the main diagonal which represents the resonance frequencies of the individual resonators are all nonzero. This indicates that all the resonators will have frequencies which deviated from the passband centre frequency of the filter.

The coupling matrix in Figure 6.15 or Figure 6.16 is denormalised to obtain the design parameters (coupling bandwidths, external quality factors and resonant frequencies of the resonators) for dimensional synthesis using the equations in Table 5.2 on page 84. The calculated design parameters are given in Table 6.9 with the self-couplings in the main diagonal represent the resonance frequencies of the individual resonators in MHz.

Table 6.9: Calculated coupling bandwidth (MHz), resonant frequencies (MHz) and external quality factors

	S	1	2	3	4	L
S	0	664.24	0	0	0	0
1	664.24	8254.48	521.50	0	6.60	0
2	0	521.50	8260.26	372.80	-107.40	0
3	0	0	372.80	8181.03	510.30	0
4	0	6.60	-107.40	510.30	8254.48	664.24
L	0	0	0	0	664.24	0
$Q_{eS1}= Q_{eS1}=12.4$						

6.3.2 Filter realisation

The calculated design parameters given in Table 6.9 together with Equation 6.1 are used to estimate the initial sizes of the filter that has a structural topology shown in Figure 6.15. The coupling method described in Chapter 5 is used to implement the filter. The filter parameters are fine-tuned using CST by modifying the resonator and each coupling to achieve the desired response. The final geometric dimension and simulated frequency response of Filter 2 and 3 are depicted in figures 6.17 and 6.18 respectively.
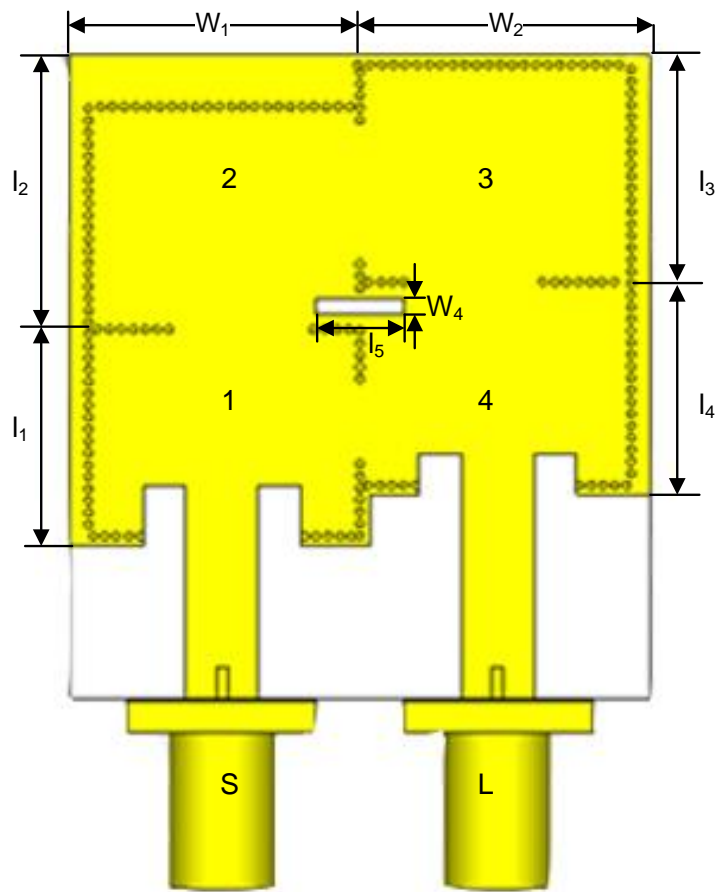
Parameter	l_1	l_2	l_3	l_4	l_5	W_1	W_2	W_3	Via spacing	Via spacing
Value (mm)	11.4	12	12	11.4	4.5	13.2	13.2	0.75	0.6	0.4

Coupling	S-1	1-2	1-4	2-3	2-4	3-4	4-L
Via-free gap (mm)	7.8	7.2	4.8	6.6	6.2	6.9	7.8
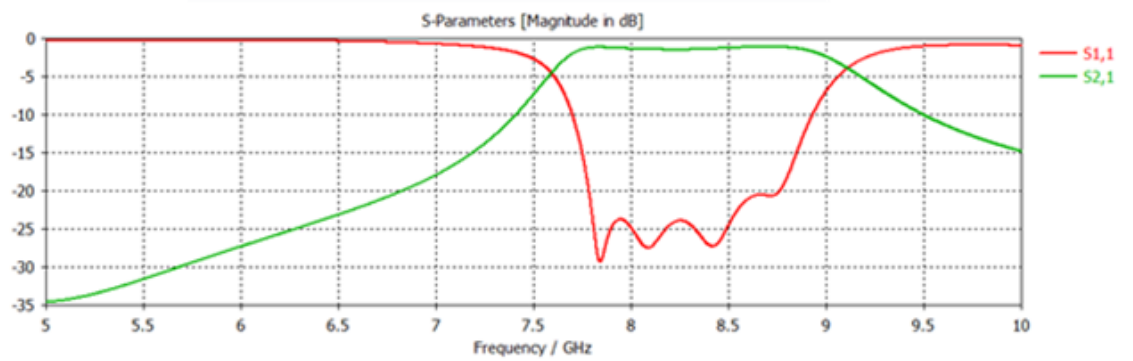
Figure 6.17: Geometric dimension and simulated frequency response of Filter 2

104
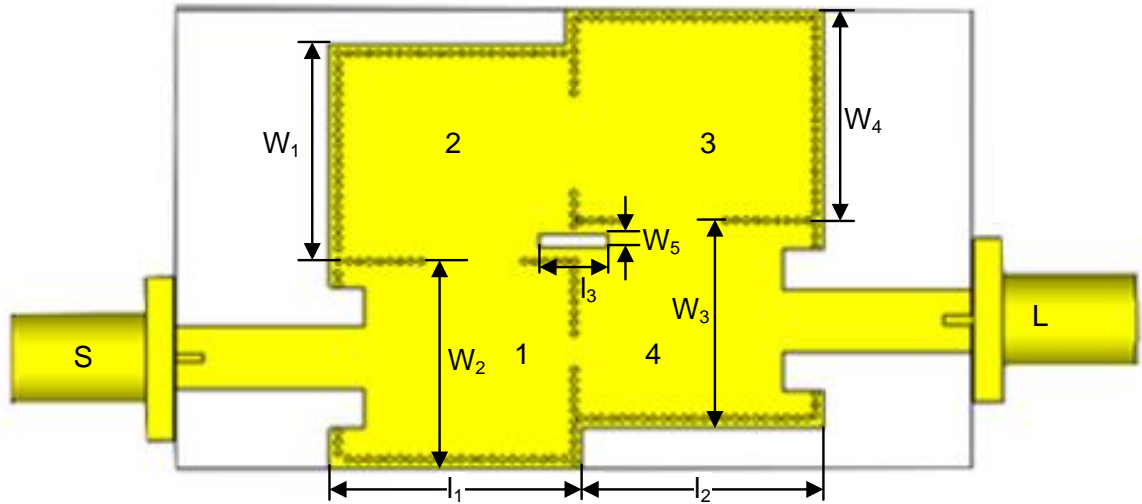
Parameter	l_1	l_2	l_3	W_1	W_2	W_3	W_4	W_5	Via spacing	Via spacing
Value (mm)	13.8	14.4	4	12.6	13.2	13.2	12.6	0.75	0.6	0.4

Coupling	S-1	1-2	1-4	2-3	2-4	3-4	4-L
Via-free gap (mm)	6.5	6	3	5.6	5.5	5.8	6.5
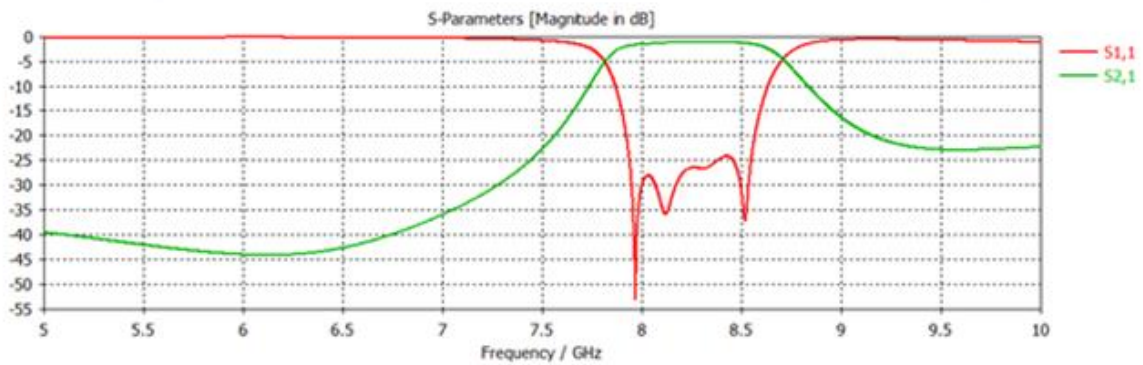
Figure 6.18: Geometric dimension and simulated response of Filter 3

All the direct internal coupling which provides positive coupling are realised by the via-free gap to implement the magnetic coupling. The cross coupling between cavity resonators 2 and 4 is negative coupling, which is implemented with the via-free gap and microstrip line for mixed coupling with negative coupling larger than positive coupling.

6.4   Summary

In this chapter, two design methods that are used to design the SIW filters are presented. Filter 1 is designed using the design method that is based on the calculations of the Chebyshev *g* values from the specifications then followed by the computation of the coupling bandwidth of the coupled resonator filter from the Chebyshev *g* values. The simulated frequency response of Filter 1 has a good return

loss in the passband that is very close to the design goal of 25 dB, and the insertion loss in the stopband that meets the targeted attenuation of 30 dB.

Filters 2 and 3 are designed using the design method that involves generation of the transfer and reflection polynomials from the prescribed transmission zeros. This is followed by the calculation of coupling element values from the transfer and reflection polynomials. The ideal frequency response that has a return loss of 25 dB in the passband and the insertion loss that is below 80 dB in the lower stopband for transmission zeros, is shown in Figure 6.14. Transmission zeros are generated to improve the stopband attenuation of the filter by introducing cross-coupling between resonators 1 and 4, and between resonators 2 and 4. Filters 2 and 3 are smaller in size compared to Filter 1. The simulated results of filters 2 and 3 have a return loss that is very close to 25 dB and are in reasonable agreement with the ideal response. The deviation of the insertion loss in the passband of the simulated results from the ideal response is caused by the dielectric constant of the material. A slight deviation of the insertion loss in the lower stopband of the simulated results from the ideal response is observed and is attributed to the weakly cross-coupling between resonators. The simulated results are compared with the measured results in Chapter 7.

CHAPTER 7. FABRICATION AND MEASUREMENTS

7.1 Introduction

This chapter commences by outlining steps used to manufacture the designed SIW filters using the in-house PCB prototyping machine; it then presents the test setup used to test the SIW filters. The SIW filters presented in the previous chapter are manufactured and tested using the HP8720 ET VNA. Then the measured results are compared with the simulated results presented in Chapter 6.

7.2 Fabrication

The SIW filters are fabricated on the same dielectric material used in simulations. The SIW filters are fabricated using the LPKF ProtoMat® S100 shown in Figure 7.1, which is the in-house PCB prototyping machine which belongs to F'SATI and the Department of Electrical Engineering at the Cape Peninsula University of Technology. The machine enables undergraduate and postgraduate students to produce PCBs for practical exercises and experiments.
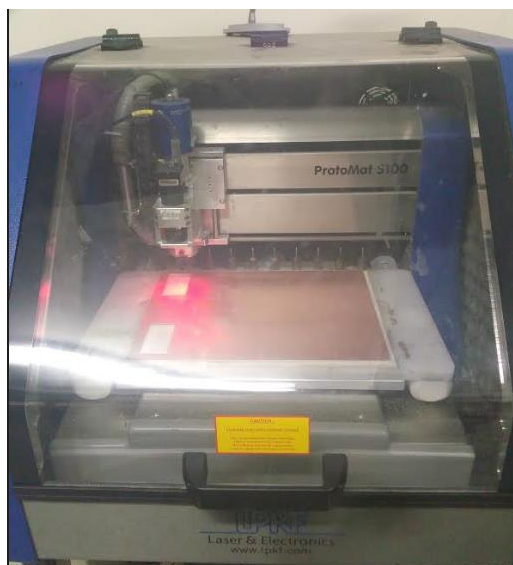
Figure 7.1: LPKF ProtoMat machine

The manufacturing steps of SIW filters shown in Figure 7.2 are as follows:

- Upload Gerber files to the control computer of the LPKF ProtoMat machine.
- LPKF ProtoMat machine drills via holes.
- Apply LPKF ProConduct paste for through-hole plating.
- Bake the PCB at 160 °C for 30 minutes to allow the ProConduct paste to dry hard.
- Mill off the unwanted copper from the PCB using the LPKF ProtoMat machine.
- Cut out the SIW filter board.
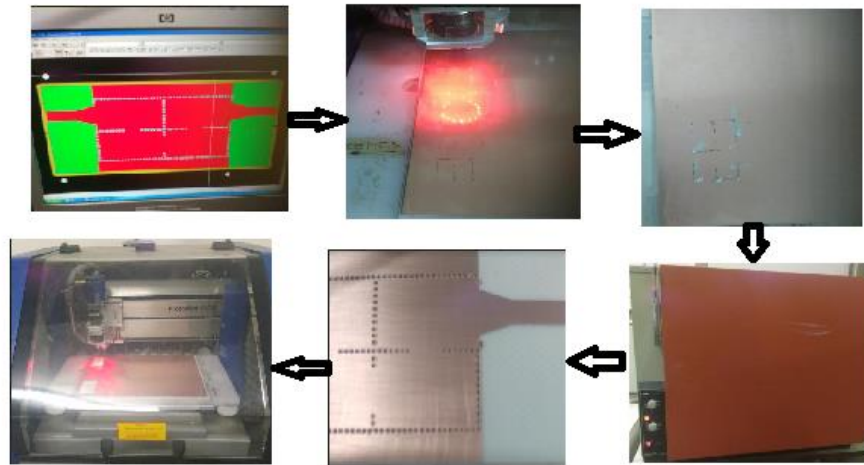
Figure 7.2: Steps used to fabricate SIW filter

Figure 7.3 and Figure 7.4 below show the manufactured SIW filters and manufactured SIW filters with SMA connectors, respectively.
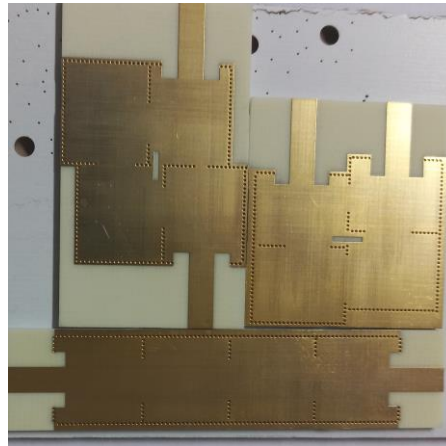
Figure 7.3: Manufactured SIW filters
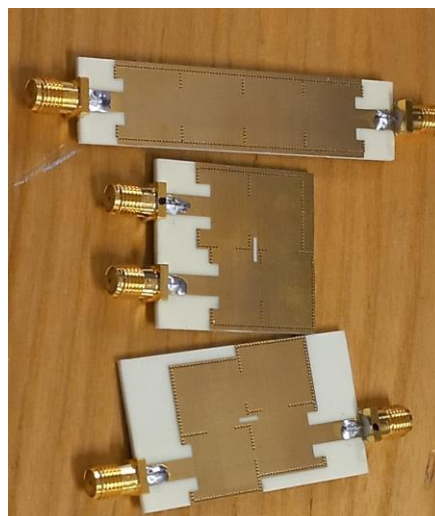
Figure 7.4: Manufactured SIW filters with SMA connectors

7.3   Inspection of the SIW filter

The fabrication process of an SIW filter can lead to manufacturing defects such as plating voids. A visual inspection on plating voids is not practicable for SIW, as the plating in the via holes cannot be visualised from the outside. Quick identification of these defects is necessary, as they will present a challenge to the measurements of the SIW filter.

2D and 3D Computed Tomography (CT) inspection techniques are used to inspect for defects in plated via holes of the fabricated SIW filter. The image in Figure 7.5 below illustrates SIW filters under inspection for via-hole plating voids. The test setup in Figure 7.5 consists of a SIW filter and a CT scan.
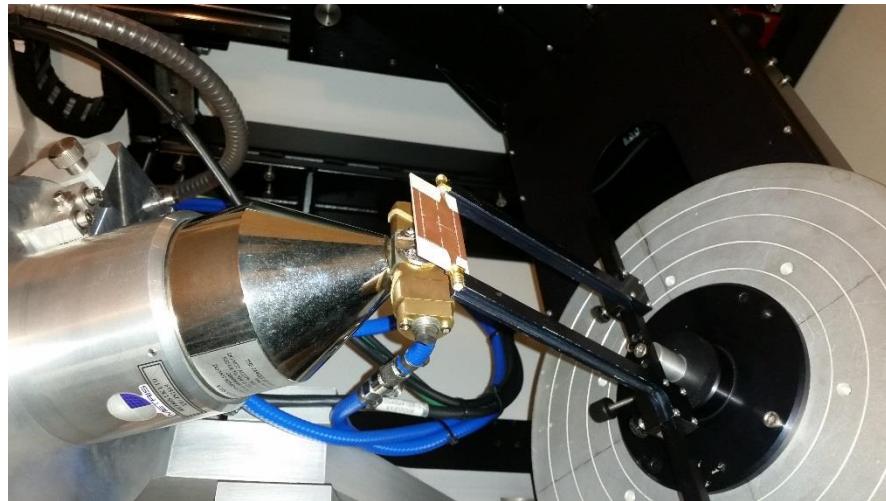
Figure 7.5: Test setup for SIW filter 2D inspection and 3D CT scan

The technique involves placing the SIW filter in between an X-ray source and detector. The X-ray source is used to generate X-ray radiation that is passed through the SIW filter. The detector captures 2D images of the X-ray patterns that passed through the SIW filter. The 2D X-ray image goes through reconstruction software to generate a 3D CT volume.

The image of the SIW filter from a 2D inspection is shown in Figure 7.6 below. The image in Figure 7.6 shows some via holes of light colour indicating low plating volume, and dark colour indicating high plating volume. The dark colour indicates very good plating, compared with the light colour, which indicates good plating as shown in Figure 7.6. Through-holes with low plating volume are acceptable as they meet the requirement to form plated via holes required in SIW filters. The image in Figure 7.6 illustrates that there are no via-hole voids in the fabricated SIW filter.

The plating is not efficient

Dark area, plating is very efficient
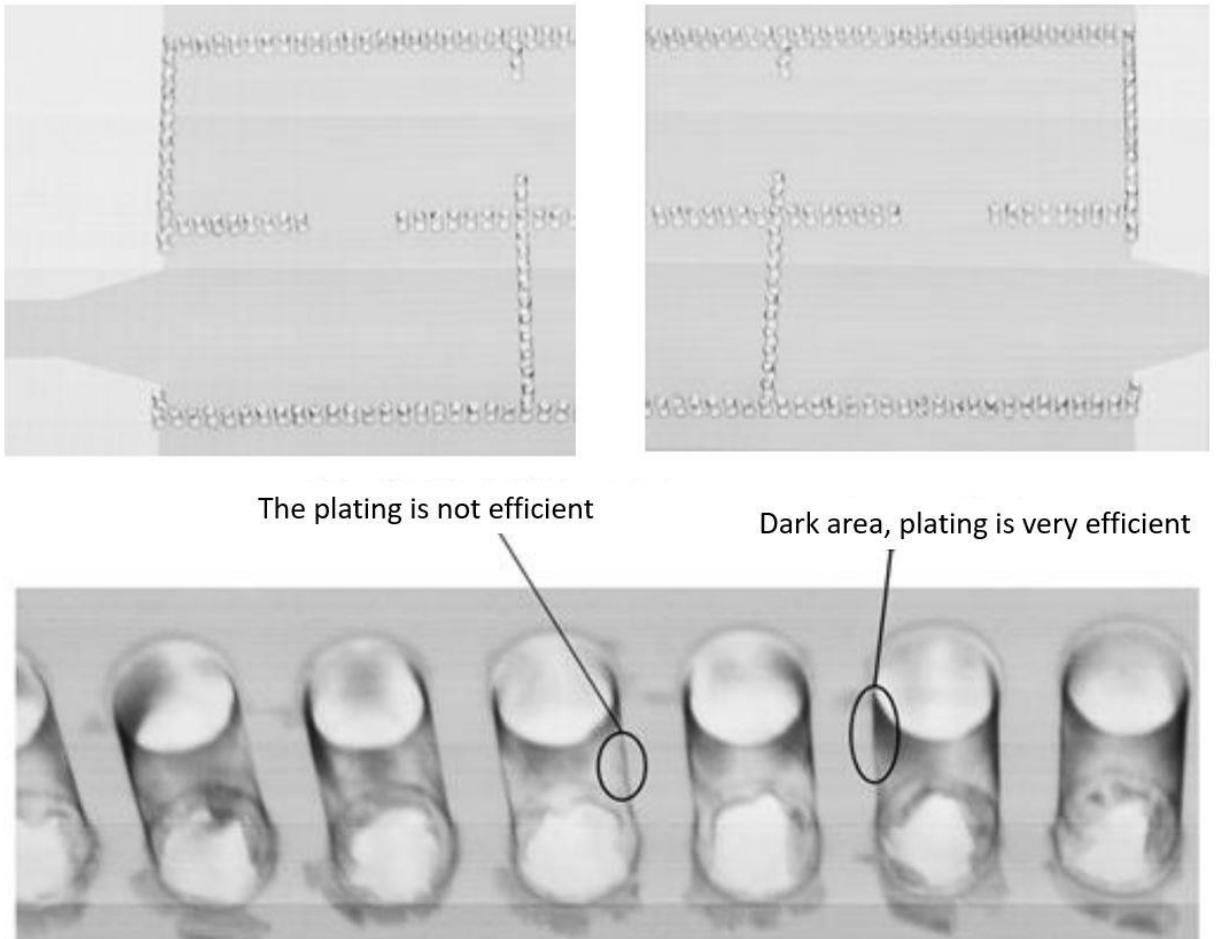
Figure 7.6: 2D scan image of the SIW filter

7.4 Measurements

The SIW filters were manufactured as shown in Figure 7.2. The measurements were carried out with the HP 8720 ET VNA shown in Figure 7.7 below. While the VNA is a highly linear receiver with enough purity in its source to make a good measurement, there are errors that limit measurements done without calibrations, thus these errors need to be corrected (Buxton, 2011:1-2). These systematic errors are removed using the vector error correction calibration kit in order to obtain accurate measurements. The measurement calibration was performed as part of the setup to test the SIW filter. Figure 7.7 shows an SIW filter under test using the HP 8720 ET VNA.
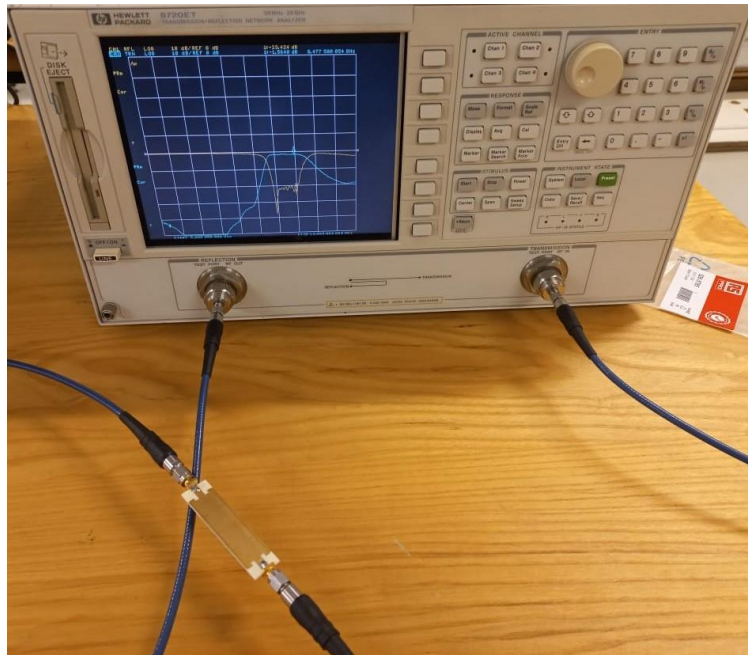
Figure 7.7: VNA and SIW filter under test

The comparison between the measured and simulated results of Filter 1 is shown in Figure 7.8 below.
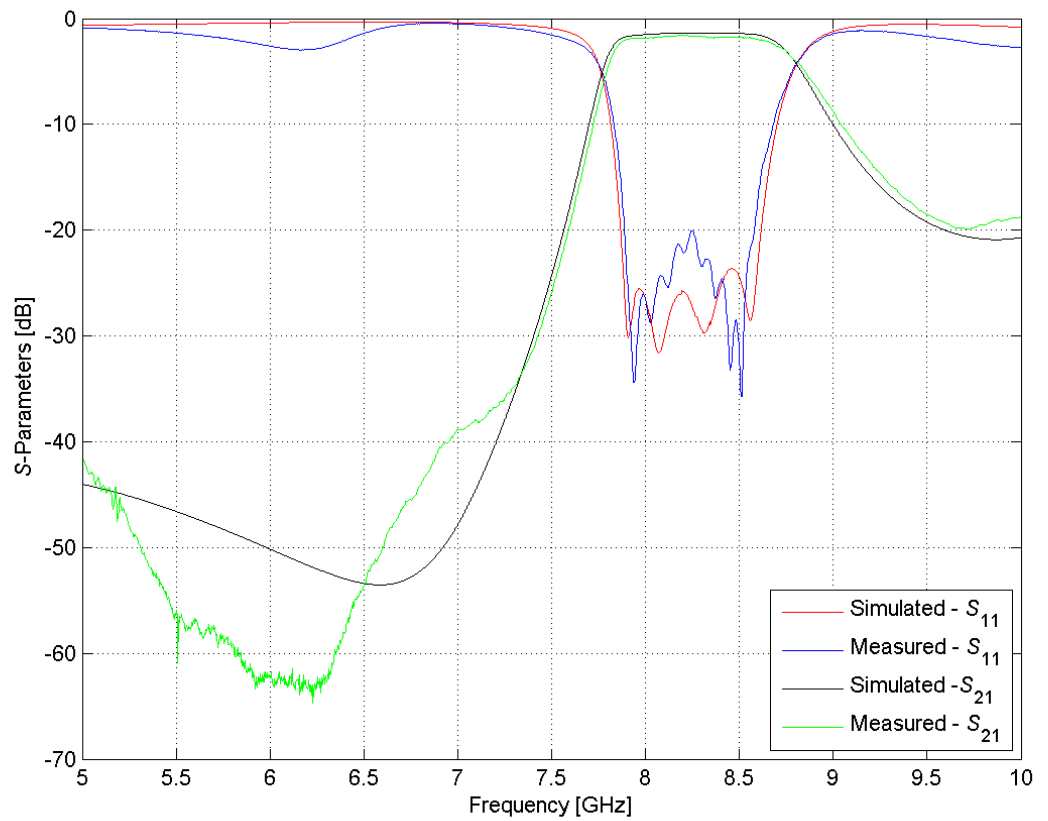
Figure 7.8: Measured results vs simulated results of Filter 1

In Figure 7.8 above, it can be seen that the measured results are in good agreement with the simulated results, thus meeting the functional specification of the required SIW filter. There is a slight difference in the passband, where the return loss of the measured filter is 20 dB, while the simulated value is at 25 dB. The return loss of 20 dB in the passband is within the limit of the minimum required return loss of 12 dB of the specification. The results in Figure 7.8 show that the measured filter attains higher levels of attenuation than the simulated results in the stopband region for transmission zeros.

The figures below compare the measured results of the SIW filters (Filter 2 and Filter 3) with the simulated results presented in Chapter 6.
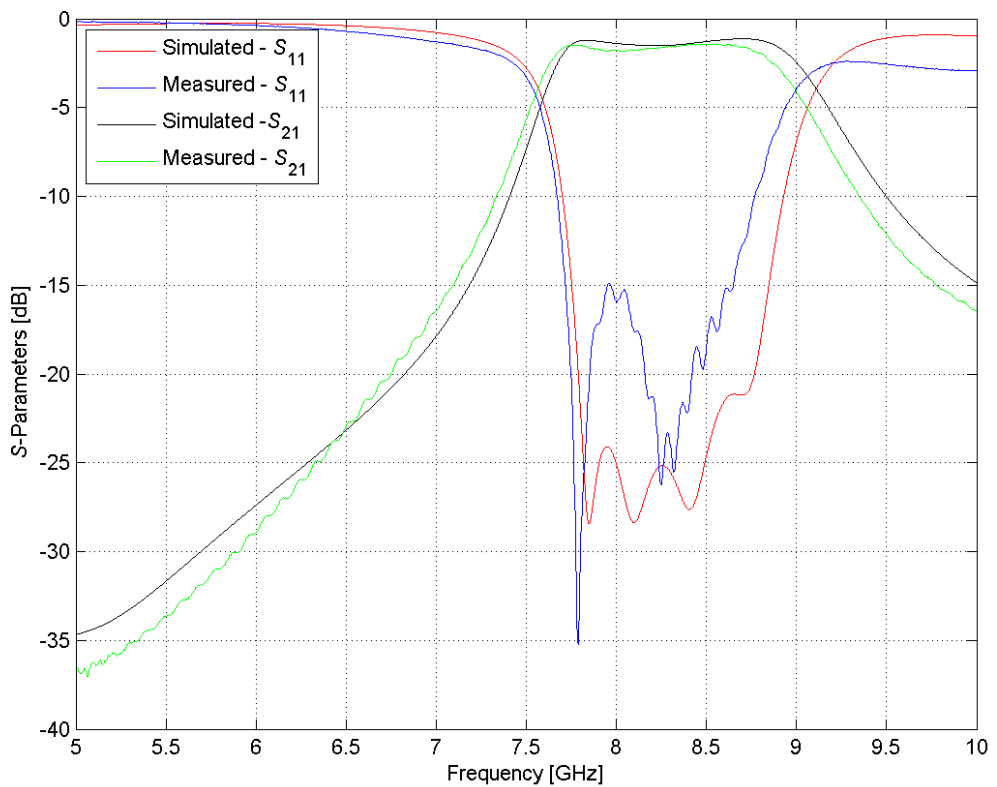
Figure 7.9: Measured results vs simulated results of Filter 2
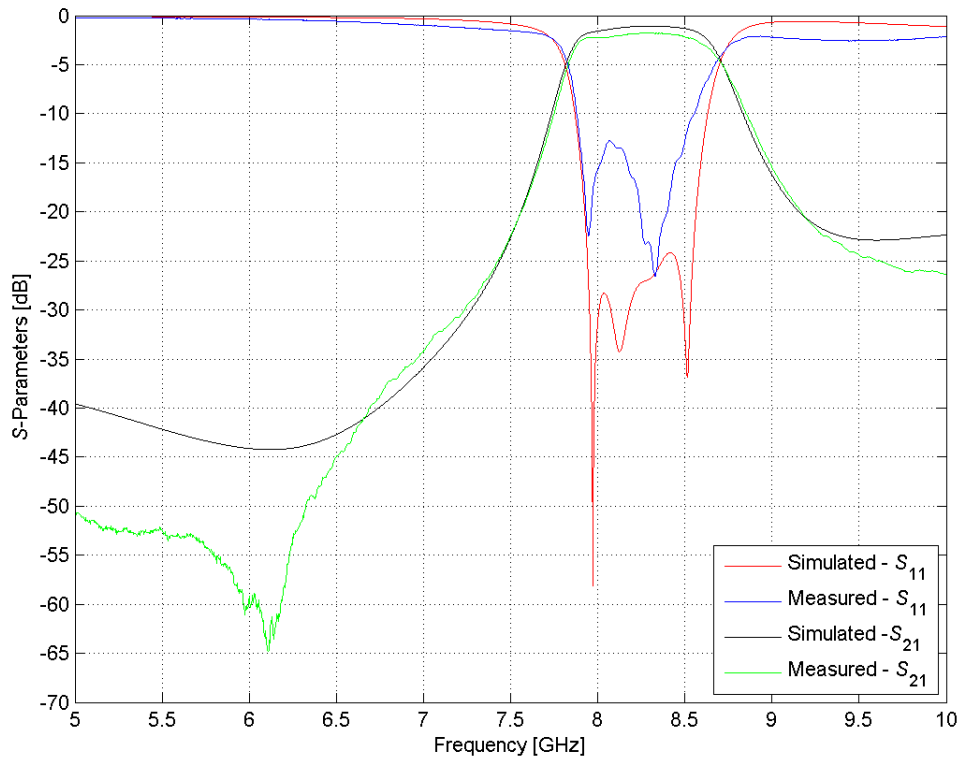
Figure 7.10: Measured results vs simulated results of Filter 3

In the figures above, it can be seen that the measured results are in good agreement with the simulated results, except for the distortion in the passband return loss which is still better than 12 dB across the passband. The figures above also show that measured results of Filter 3 attain higher levels of attenuation than the simulated results in the stopband region for transmission zeros. The distortion of the bandpass return loss could be caused by radiation loss at geometrical discontinuities of the 50 Ω microstrip line and by the SMA connectors used during measurements. The inaccurate drilling positions of metallised via holes, diameter of metallised via holes could be the cause of the minor discrepancy between the measured and simulated results.

In order to investigate the cause of the discrepancy between simulated and measured results, more boards of Filter 3 were built and measured. Figure 7.11 below illustrates the remanufactured SIW filters (Filter 3). Figure 7.12 compares the measured results of the remanufactured SIW filter with the simulated results presented in Chapter 6.
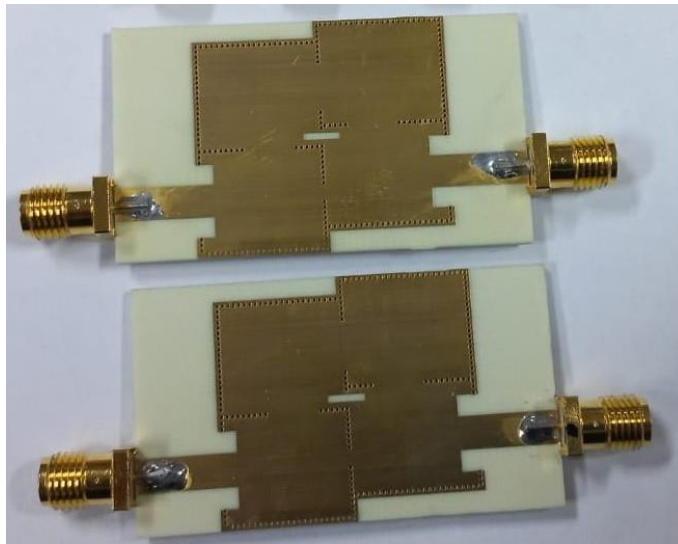
Figure 7.11: Remanufactured SIW filters (Filter 3)
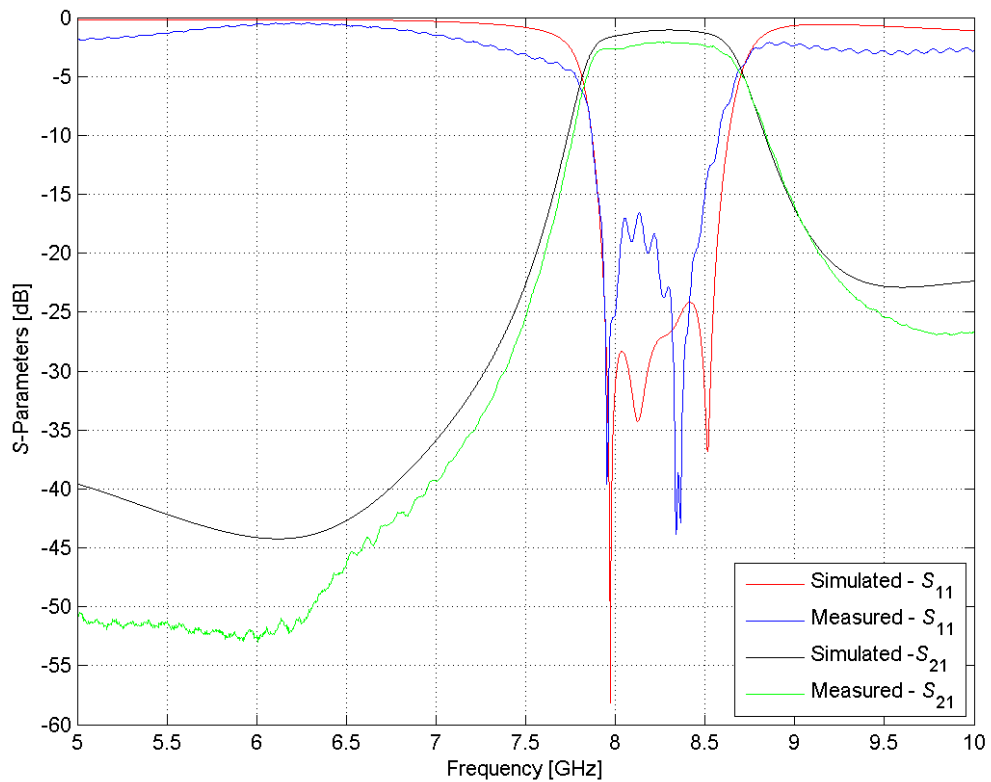
Figure 7.12: Measured results vs simulated results of remanufactured Filter 3

The measured results of Filter 3 in Figure 7.12 exhibit an improved filter response compared to those in Figure 7.10 with a bandpass return loss that is greater than 15 dB and stopband insertion loss that is greater than 35 dB. This shows that the

manufacturing tolerances and/or connector soldering inconsistencies have contributed to the discrepancy of measured and simulated response.

7.5 Temperature test

According to Gilmore (2002:22), a satellite orbiting in Low Earth Orbit (LEO) views a small part of the globe at any given time, since the LEO altitude is smaller than the Earth's diameter. This results in the satellites being exposed to a rapid change of environmental conditions as it passes over regions having different combinations of land, ocean, snow and cloud cover. Space thermal environments experienced by the satellite orbiting in LEO are direct sunlight (solar flux), sunlight reflected off Earth (albedo) and infrared energy emitted from the Earth. Solar flux is a function of the distance from the sun, while albedo and the Earth's infrared energy are functions of the altitude of the orbit (Gilmore, 2002:22-24).

Larson and Wertz (1999:105-109) analysed two typical orbits of a satellite, namely the eclipses for LEO and the sun angle. An eclipse case occurs when the disk of the Earth crosses in front of the sun, resulting in satellite exposure to only low temperatures of the earth's infrared energy, as there will be no effects of the solar flux and albedo. In the sun angle, the satellite faces the sun as it travels in its orbit, resulting in the satellite's exposure to high-temperature environments. Thus there is a need for a temperature test to establish whether the filter will still function as expected when exposed to a space environment that changes in temperature, as the satellite will experience both cold and hot environments while orbiting.

The temperature test is done with the temperature chamber operated in a temperature range of −25°C to 60°C in conjunction with the VNA measuring the SIW filter as illustrated in Figure 7.13

Figure 7.13:Temperature test setup

The minimum and maximum allowable temperature range for the X-band transmitter from African Space Innovation Centre (ASIC) database is −25°C to 60°C. Therefore, the SIW filter was left at least 10 minutes at low temperature (−25°C), room temperature (20°C), and high temperature (60°C) before taking the measurement. The rate of temperature change was set to 2°C per minute and set to remain for 10 minutes at every step of 10°C, then continue changing at a rate of 2°C per minute as illustrated by the graph in Figure 7.14. The test took close to 2 hours and 35 minutes as shown in the graph in Figure 7.14.
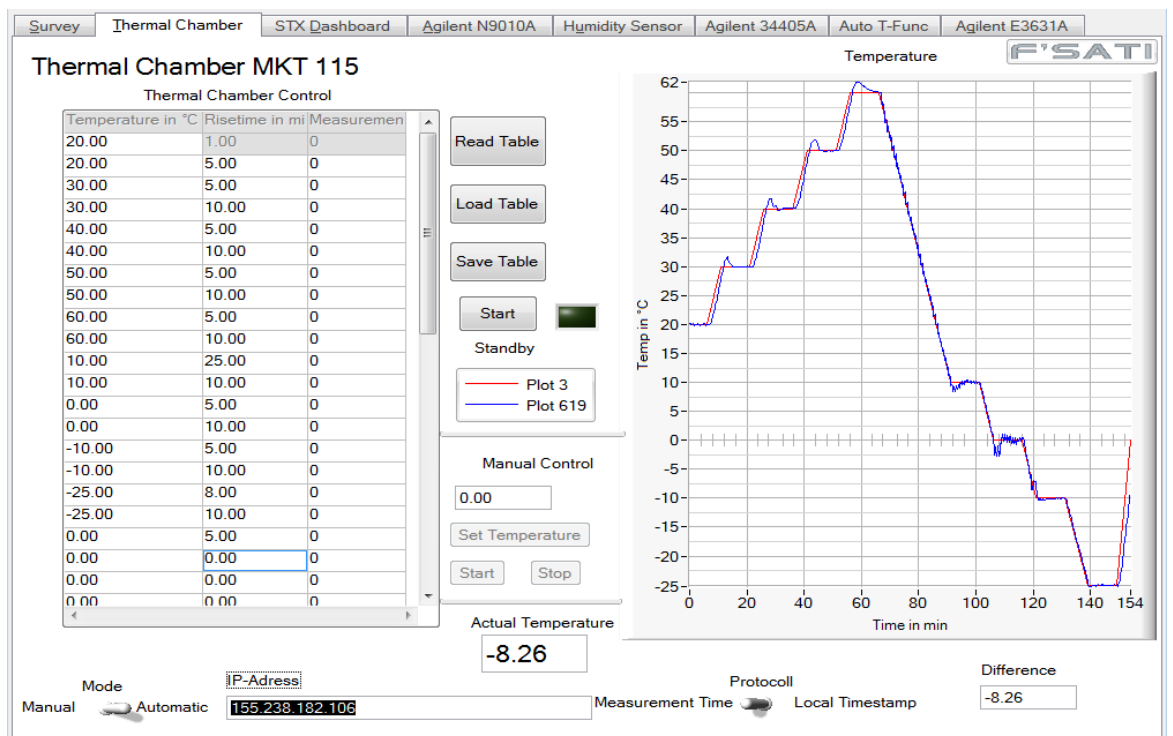
Figure 7.14: Temperature vs time graph

The measured results of the SIW filter at various temperatures are shown in Figure 7.15. The measured results show that the SIW filter is stable between the extreme temperature changes: both passband and stopband are stable. The transmission in the stopband is below −30 dB and reflection in the passband is well below −20 dB across the temperature changes.
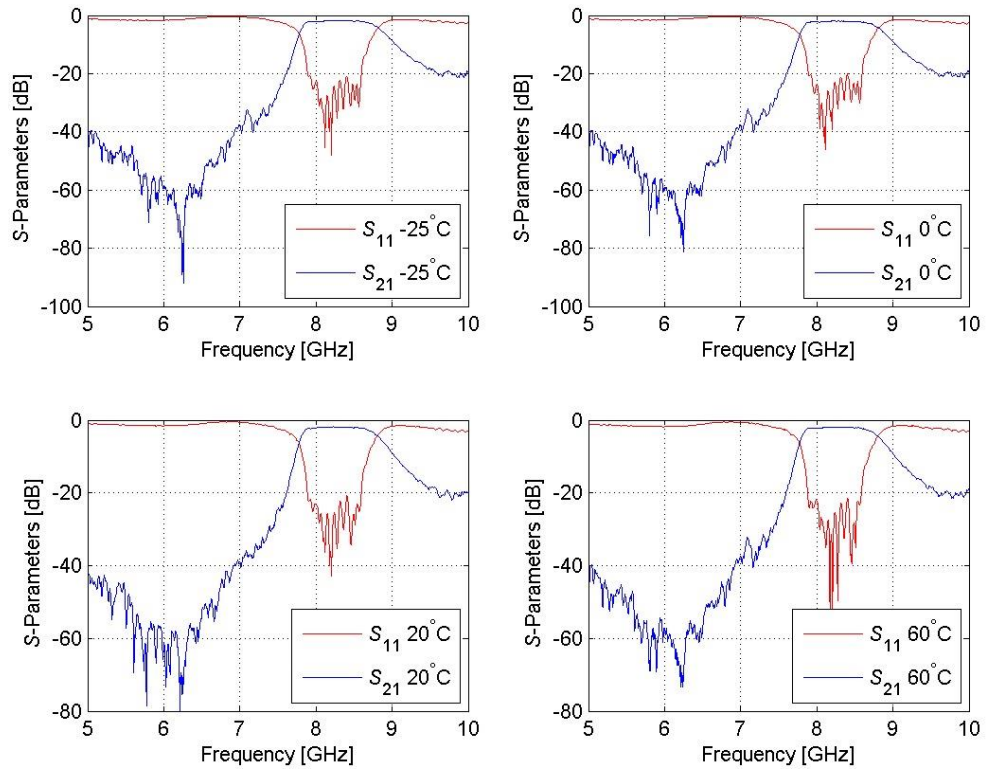
Figure 7.15: Measured results at various temperatures

The measured results are zoomed in for the passband (8 to 8.5 GHz) as illustrated in Figure 7.16. There is a small shift in frequency within the passband as the temperature changes; however the shift is still within the passband and the return loss is still greater than 20 dB, thus it will not affect the functionality of the filter.
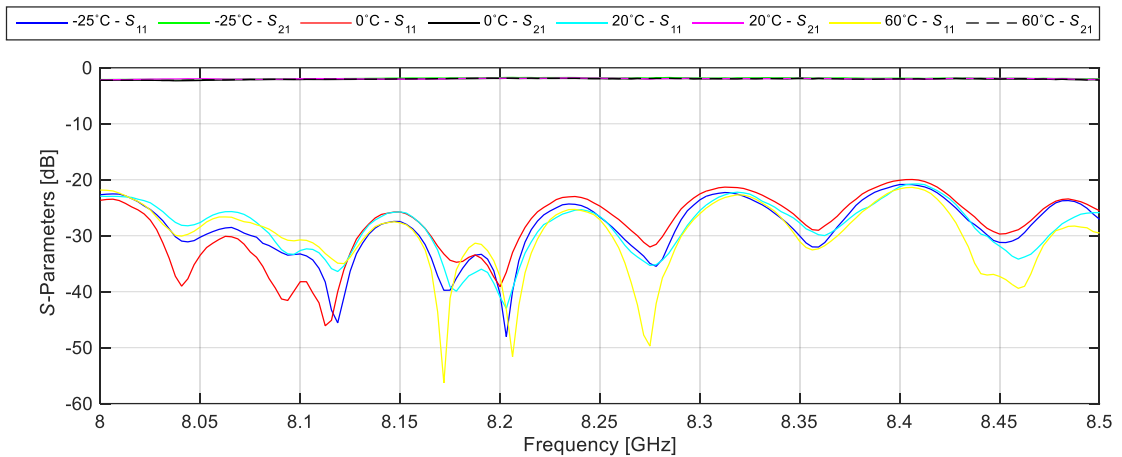
Figure 7.16: Measured results within the passband at various temperatures

7.6 Summary

The manufacturing process of the SIW filter using an in-house PCB Prototyping Machine is presented.

As can be seen, the measured results are in good agreement with the simulated results. The measured passband return loss is greater than 20 dB for Filter 1, 15 dB for Filter 2 and Filter 3. The measured lower stopband insertion loss is better than 35 dB for Filter 1 and Filter 3, and 15 dB for Filter 2 from 7.2 GHz down to 5 GHz. The measured results of Filter 1 and 3 show that filters attain a high level of attenuation in the lower stopband for transmission zeros. By comparing the simulated results and measured results, a little discrepancy is observed which is influenced by the manufacturing tolerance, including dielectric and conductor loss, and connector soldering inconsistencies. This might be also due to radiation loss at geometrical discontinuities of the 50 Ω microstrip line and losses of the connectors.

In overall, Filter 1 and Filter 3 would perfectly meet the functional specifications (presented in Section 1.4) of the filter required at F'SATI.

CHAPTER 8. CONCLUSION AND RECOMMENDATIONS FOR FUTURE WORK

8.1 Introduction

A filter for an X-band transmitter that has a passband of 8.025 GHz to 8.45 GHz with transmission zeros at the local oscillator (6.8 to 7.2 GHz) and at image frequencies (5.6 to 6 GHz) is required for CubeSats developed by F'SATI. The planar technology, such as microstrips lines, is small in size and low cost, but exhibits high losses compared with the metallic rectangular waveguide. Although metallic rectangular waveguides are high quality, their drawback is their size and heavyweight, which makes them unsuitable for some applications. The SIW technology is introduced as an alternative to overcome some of the drawbacks, as it combines the better of the two technologies. An SIW technology is identified as a suitable technology to be used to design the required filter, thus the research project focused on the development of the X-band SIW filter.

8.2 Conclusion

One of the concerns for circuits in space is the large temperature fluctuation that can alter the dielectric constant of the PCB material; hence the temperature test is essential for these circuits. The temperature test conducted in the designed SIW filter showed that the SIW filter is stable between the extreme temperature changes.

The functional specifications of the required filter are met. The measured insertion loss in the passband is 2.5 dB and is reasonably good for an SIW filter with a microstrip line coupled to it as the feeding line. The 50 Ω microstrip line suffers from radiation loss at geometrical discontinuities owing to its open nature. The radiation loss in the microstrip line and losses of the two SMA connectors used during measurements are added to the amount of the measured insertion loss. Removing the two SMA connecters used during testing will definitely improve the insertion loss over the passband. The return loss is better than 15 dB within the passband.

The stopband attenuation over the local oscillator frequency range (6.8 to 7.2 GHz) and image frequency range (5.6 to 6 GHz) where transmission zeros are required, is better than 30 dB, showing high levels of attenuation. The return loss over the local oscillator frequency range (6.8 to 7.2 GHz) and image frequency range (5.6 to 6 GHz) is close to 0 dB, showing no transmission because of the high reflection.

The measured and simulated results are generally in good agreement, except for the minor discrepancy between them that may be due to manufacturing error or imperfect

simulations. The measured results show that the SIW filters meet the filter specifications.

8.3　Recommendations for future work

The open nature of the microstrip line configuration can lead to an unwanted interaction with other parts of the circuit in a CubeSat, owing to external electromagnetic coupling. Thus it is recommended that the SIW filter be sandwiched in the inner layer of the PCB as illustrated in Figure 8.1 in order to avoid the use of the microstrip line and SMA connectors. The top and the bottom part of the PCB can be utilised to place SMT components, as CubeSats have size constraints.
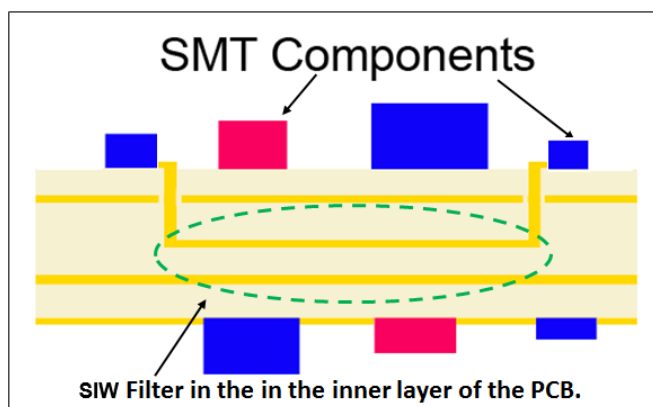
Figure 8.1: SIW filter buried in the inner layer of the PCB

A laser drill for accurate positioning of metallised via holes, diameters of metallised via holes and milling may reduce the manufacturing error of SIW filters.

BIBLIOGRAPHY

Bozzi, M., Pasian, M., Perregrini, L. & Wu, K. 2009. On the losses in substrate-integrated waveguides and cavities. *International Journal of Microwave and Wireless Technologies*, 1(5):395-401, September.

Bozzi, M., Perregrin, L. & Wu, K. 2008a. Modeling of conductor, dielectric and radiation losses in substrate integrated waveguide by the boundary integral-resonant mode expansion method. *IEEE Transactions on Microwave Theory and Techniques*, 58(12):3153-3161, December.

Bozzi, M., Perregrini, L. & Wu, K. 2008b. Modeling of losses in substrate integrated waveguide by boundary integral-resonant mode expansion method. In Denniston, D.B. (ed.). *Proceedings of the 2008 IEEE MTT-S International Microwave Symposium Digest, Atlanta, GA,15–20 June*. Piscataway, NJ: IEEE: 515-518.

Buxton, B. 2011. Calibration techniques help ensure accurate VNA measurements. *RF Globalnet Newsletter*: 1-5, May 11.

Cameron, R.J. 2011. Advance filter synthesis. *IEEE Microwave Magazine*, 12(6):42-61, September.

Cameron, R.J., Kudsia, C.M. & Mansour, R.R. 2018. *Microwave filters for communication systems fundamentals, design and applications*. 2nd ed. Hoboken, USA: John Wiley & Sons Inc.

Cassivi, Y., Perregrini, L., Arcioni, P., Bressan, M., Wu, K. &Conciauro, G. 2002. Dispersion characteristics of substrate integrated rectangular waveguide. *IEEE Microwave and Wireless Components Letters*, 12(9):333-335, September.

Cassivi, Y., Perregrini, L., Wu, K. & Concerto, G. 2002. Low-cost and High-Q millimeter-wave resonator using substrate integrated waveguide technique. In *Proceedings of the 32nd European Microwave Conference 2002*, *Milan, Italy, 23–26 September*. London: Microwave Engineering Europe: 1-4.

Che, W., Li, C., Deng, K. &Yang, L. 2008. A novel bandpass filter based on complementary split rings resonators and substrate integrated waveguide. *Microwave and Optical Technology Letters*, 50(3):699-701, March.

Chen, X., Hong, L., Cui, T., Chen, J.& Wu, K. 2005. Substrate integrated waveguide linear phase filter. *IEEE Microwave and Wireless Components Letters*, 15(11):787-789, November.

Chen, X., Wu, K. & Drolet, D. 2009. Substrate integrated waveguide filter with improved stopband performance for satellite ground terminal. *IEEE Transactions on Microwave Theory and Techniques*, 57(3):674-683.

Chen, X. & Wu, K. 2008. Substrate integrated waveguide cross-coupled filter with negative coupling structure. *IEEE Transactions on Microwave Theory and Techniques*, 56(1):142-149.

Chen, X. & Wu, K. 2009a. Low-loss ultra-wideband transition between conductor-backed coplanar waveguide and substrate integrated waveguide. In *Proceedings of the 2009 IEEE MTT-S International Microwave Symposium Digest, Boston, MA, 7–12 June*. Piscataway, NJ: IEEE: 349-352.

Chen, X.& Wu, K. 2009b. Self-equalized pseudo-elliptical filter made of substrate integrated waveguide. *Electronic Letters*, 45(2):112-113, January.

Chen, X. & Wu, K. 2014a. Substrate integrated waveguide filter: basic design rules and fundamental structure features. *IEEE Microwave Magazine*, 15(5):108-116, July.

Chen, X. & Wu, K. 2014b. Substrate integrated waveguide filter: practical aspects and design considerations. *IEEE Microwave Magazine*, 15(7):75-83, November.

Cheng, Y.J., Zhang, C. A. & Fan, Y. 2011. Miniaturized multilayer folded substrate integrated waveguide butler matrix. *Progress in Electromagnetics Research C*, 21:45-58.

Connor, F.R. 1986. *Waves: introductory topics in electronics and telecommunication*. London: Edward Arnold.

Deslandes, D. 2010. Design equations of tapered microstrip to substrate integrated waveguide transitions. In *Proceedings of the 2010 IEEE MTT-S International Microwave Symposium Digest, Anaheim, CA, 23–28 May.* Piscataway, NJ: IEEE: 704-707.

Deslandes, D. & Wu, K. 2001a. Integrated transition of coplanar to rectangular waveguides. In *Proceedings of the 2001 IEEE MTT-S International Microwave Symposium Digest, Phoenix, AZ, 20–24 May.* Piscataway, NJ: IEEE: 619-622.

Deslandes, D. & Wu, K. 2001b. Integrated microstrip and rectangular waveguide in planar form. *IEEE Microwave and Wireless Components Letters*, 11(2):68-70, February.

Deslandes, D. & Wu, K. 2002. Design consideration and performance analysis of substrate integrated waveguide components. In *Proceedings of the 32nd European Microwave Conference 2002, Milan, Italy, 23–26 September.* London: Microwave Engineering Europe: 1-4.

Deslandes, D. & Wu, K. 2003a. Single-substrate integration technique of planar circuits and waveguide filters. *IEEE Transactions on Microwave Theory and Techniques*, 51(2): 593-596, February.

Deslandes, D. & Wu, K. 2003b. Millimeter-wave substrate integrated waveguide filters. In *Proceedings of the 2003 Canadian Conference on Electrical and Computer Engineering, Montreal, Quebec, Canada,4-7 May*. Piscataway, NJ: IEEE:1917-1920.

Deslandes, D. & Wu, K. 2006. Accurate modeling, wave mechanisms, and design considerations of a substrate integrated waveguide. *IEEE Transactions on Microwave Theory and Techniques*, 54(6): 2516-2526, June.

De Villiers, D. & Van Zyl, R. n.d. *ZACube-2: The successor to Africa's first nanosatellite.*http://www.amsatsa.org.za/ZACube-2%20%20The%20successor%20to%20Africa%E2%80%99s%20first%20nanosatellite.pdf [28 August 2017].

Ding, Y. & Wu, K. 2009. Miniaturized hybrid ring circuits using T-type folded substrate integrated waveguide. In *Proceedings of the 2009 IEEE MTT-S International Microwave Symposium Digest, Boston, USA,7-12 June.* Piscataway, NJ: IEEE: 705-708.

Djerafi, T., Wu, K. & Deslandes D. 2012a. A temperature-compensation technique for substrate integrated waveguide cavities and filters. *IEEE Transactions on Microwave Theory and Techniques*, 60(8):2448-2455, June.

Djerafi, T., Wu, K. & Deslandes D. 2012b. Temperature drift compensation technique for substrate integrated waveguide oscillator. *IEEE Microwave and Wireless Components Letters*, 22(9):489-491, August 20.

Gilmore, D.G. (ed.). 2002. *Spacecraft thermal control handbook, Volume I: Fundamental technologies*. Washington, DC: American Institute of Aeronautics and Astronautics.

Gowri, R. 2008. *Microwave and radar engineering.* New Delhi: S.K. Kataria.

Grigoropoulos, N., San-Izquierdo. B. & Young, P. R. 2005. Substrate integrated folded waveguides and filters. *IEEE Microwave and Wireless Components Letters*, 15(12):829-831, December.

Guan, X., Wang, B., Wang, X., Liu, H., Yuan, Y. & Zhang, X. 2012. Design of a dual-mode substrate integrated waveguide filter with slot-line perturbation. In *Proceedings of the 2012 International*

*Conference on Microwave and Millimeter Wave Technology, Shenzhen, China, 5–8 May.*Piscataway, NJ: IEEE: 1-4.

Hammerstad, E.O. 1975. Equations for Microstrip Circuit Design. In *Proceedings of the 5th European Microwave Conference 1975, Hamburg, Germany, 1-4 September.* Sevenoaks: Microwave Exhibitions and Publishers Ltd: 268-272.

Hao, Z.C., Hong, W., Chen, X.P., Chen, J.X., Wu, K. & Cui, T.J. 2005. Multilayered substrate integrated waveguide (MSIW) elliptic filter. *IEEE Microwave and Wireless Components Letters*, 15(2): 95-97.

Hao, Z.C., Hong, W., Li, H., Zhang, H. & Wu, K. 2005. A broadband substrate integrated waveguide (SIW) filter. In *Proceedings of the 2005 IEEE Antennas and Propagation Society International Symposium, Washington, DC 3–8 July.* Piscataway, NJ: IEEE: 598-601.

Hong, J. 2011. *Microstrip filters for RF/microwave applications.* 2nd ed. Hoboken, NJ: John Wiley

Hong, W., Liu, B., Wang, Y., Lia, Q., Tang, H., Yin, X., Dong, Y., Zhang, Y. & Wu, K. 2006. Half mode substrate integrated waveguide: A new guided wave structure for microwave and millimetre wave application. In *Proceedings of the 2006 Joint 31st International Conference on Infared Millimeter Waves and 14th International Conference on Teraherz Electronics, Shanghai, China, 18–22Sept.* Piscataway, NJ: IEEE: 219.

Huang, T., Shen, T. & Wu, R. (2010). Design and modeling of microstrip line to substrate integrated waveguide transitions, passive microwave components and antennas. In Zhurbenko, V. (ed.). *Passive microwave components and antennas.* Rijeka, Croatia: InTech: 225-246.

Hunter, I. 2001. *Theory and design of microwave filters.* London: Institution of Engineering and Technology.

Jones, T. R. & Daneshmand, M. 2017. Miniaturized folded ridged half mode substrate integrated waveguide. In *Proceedings of the 2017 47th European Microwave Conference, Nuremburg, Germany, 10–12 October.* Piscataway, NJ: IEEE: 528-531.

Karunanithi, V.,Verhoeven, C.J.M. & Lubbers, W. 2015. LINC transmitter architecture for nano-satellite applications. In *Proceedings of the 2015 Conference of IEEE Aerospace, Big Sky, MT, 7–14 March.* Piscataway, NJ:IEEE:1-9.

Kudsia, C., Cameron, R. & Tang W.1992. Innovations in microwave filters and multiplexing networks for communications satellite systems. *IEEE Transactions on Microwave Theory and Techniques,* 40(6):1133-1149, June.

Kumar, H., Jadhav, R.& Ranade, S. 2012. A review on substrate integrated waveguide and its microstrip interconnect. *IOSR Journal of Electronics and Communication Engineering*, 3(5):36-40, September–October.

Kumari, A., Kumar, D. & Kumar, A. 2017. A Ka-band bandpass filter with cylindrical cavity resonators using substrate integrated waveguide (SIW*). International Journal of Microwaves Applications*, 6(1):14-17, January–February.

Kumari, S. & Srivastava, S. 2013. Losses in waveguide and substrate integrated waveguide (SIW) for Ku band. *International Journal of Modern Engineering Research*, 3(1):53-57, January–February.

Ladani, F.T., Jam, S. & Safian, R. 2010. A novel X-band bandpass filter using substrate integrated waveguide resonators. In *Proceedings of 2010 IEEE Asian-Pasific Conference on Applied Electromagnetics, Port Dickson, Malaysia, 9-11 November.* Piscataway, NJ: IEEE: 1-5.

Lai, Q., Fumeaux. C., Hong, W. & Vahldieck, R. 2009. Characterization of the propagation properties of the half-mode substrate integrated waveguide. *IEEE Transactions on Microwave Theory and Techniques*, 57(8): 1996-2004, August.

Laplante, P.A. (ed.). 2005. *Comprehensive dictionary of electrical engineering*. Boca Raton, FL: CRC Press.

Larson, W.J. & Wertz, J.R. (eds). 1999. *Space mission analysis and design*. 3rd ed. Torrance, CA: Microcosm Press.

Macchiarella, G. & D'Oro, S.C.1998. Design of generalized comb filters with asymmetric transmission zeros using arbitrary cascaded triplet and quadruplet sections. In *Proceedings of the 199828th European Microwave Conference, Amsterdam, Netherlands, 5–9 October*. Piscataway, NJ: IEEE: 179-183.

Makimoto, M. & Yamashita, S. 2013. *Microwave resonators and filters for wireless communication: theory, design and applications*. New York, NY: Springer.

Mansour, R.R. 2009. High-Q tunable dielectric resonator filters. *IEEE Microwave Magazine*, 10(6):84-98, September.

Martin, P. & Ness, J.1999. Coupling bandwidth and reflected group delay characterization of microwave band-pass filters. *Applied Microwave and Wireless*, 11(5):86-98, May.

Matthaei, G., Young, L.& Jones, E.M.T. 1980. *Microwave filters, impedance-matching networks, and coupling structures*. Norwood, MA: Artech House.

Mehdi, D., Keltouma, N., Bouazza, T.H.C. & Feham, M. 2014. Design of substrate integrated waveguide bandpass filter of SCRRs in the microstrip line. *International Journal of Engineering Research and General Science*, 2(3):302-314, April–May.

Mira, F., Mateu, J., Cogollos, S. & Boria, V.E. 2009. Design of ultra-wideband substrate integrated waveguide filters in zigzag topology. *IEEE Microwave and Wireless Components Letters*, 19(5):281-283.

National Telecommunications Commission. n.d. http://ntc.gov.ph/wp-content/uploads/2016/nrfat/NRFAT-2016-Rev-2.pdf[29 August 2017].

Ness, J.B., 1998. A unified approach to the design, measurement, and tuning of coupled-resonator filters. *IEEE Transactions on Microwave Theory and Techniques*, 46(4):343-351, April.

Patel, A., Kosta, Y.P., Vala, A. & Goswami, R. 2015. Design and performance analysis of metallic posts coupled SIW-based multiband bandpass and bandstop filter. *Microwave and Optical Technology Letters*, 57(6):1409-1417, June.

Pozar, D.M. 2012. *Microwave engineering*. 4thed. Hoboken, NJ: John Wiley.

Rabah, M.A., Abri, M., Tao, J.W. & Vuong, T. 2014. Substrate integrated waveguide design using the two dimentionnal finite element method. *Progress in Electromagnetics Research M*, 35:21-30.

Rhbanou, A., Sabbane, M. & Bri, S. 2015. Design of K-band substrate integrated waveguide band-pass filter with high rejection. *Journal of Microwaves, Optoelectronics and Electromagnetic Applications*, 14(2):155-169, December.

Salehi, M., Bornemann, J. & Mehrshahi, E. 2013. Substrate-integrated waveguide bandpass filters with frequency-dependent coupling elements. *International Journal of RF and Microwave Computer-Aided Engineering*, 24(2):237-242.

Shang, X., Xia, W.& Lancaster, M.J. 2014. The design of waveguide filters based on cross-coupled resonators. *Microwave and Optical Technology Letters*, 56(1):3-8, January.

Shen, W., Yin, W. & Sun, X. 2011. Miniaturized dual-band substrate integrated waveguide filter with controllable bandwidths. *IEEE Microwave and Wireless Components Letters*, 21(8):418-420, August.

Shen, W., Yin, W., Sun, X. & Wu, L. 2013. Substrate-integrated waveguide bandpass filters with planar resonators for system-on-package. *IEEE Transactions on Components, Packaging and Manufacturing Technology*, 3(2):253-261, December.

Shirgur, B. & Shannon, D. 2000. The design and feasibility study of nanosatellite structures for current and future FSI micromissions. In Redd, F.J.& Meurer, R.H. (eds). *Proceedings of the 14thAIAA/USU Conference on Small Satellites, Logan, UT, 21–24 August.* Logan, UT: Utah State University; American Institute of Aeronautics and Astronautics: 1-12.

Srivastava, G.P. & Gupta, V.L. 2006. *Microwave devices and circuit design*. New Delhi: Prentice Hall.

Szydlowski, L., Leszczynska, N. & Mrozowski, M. 2013. A linear phase filter in quadruplet topology with frequency-dependent couplings. *IEEE Microwave and Wireless Components Letters*, 24(1):32-34.

Szydlowski, L., Leszczynska, N., Lamecki, A. & Mrozowski, M. 2012. A substrate integrated waveguide (SIW) bandpass filter in a box configuration with frequency-dependent coupling. *IEEE Microwave and Wireless Components Letters*, 22(11):556-558.

Tang, H.J., Hong, W., Chen, J., Luo, G.Q. & Wu, K.2007. Development of millimetre-wave planar diplexers based on complementary characters of dual-mode substrate integrated waveguide filters with circular and elliptic cavities. *IEEE Transactions on Microwave Theory and Techniques*, 55(4):776-782, April.
Tang, H.J., Hong, W., Hao, Z.C., Chen, J.X. & Wu, K. 2005. Optimal design of compact millimetre-wave SIW circular cavity filters. *ElectronicLetters*, 41(19):1-2, September.

Tang, Y.,Wu, K. &Mallat, N.K. 2015. Development of substrate-integrated waveguide filters for low-cost high-density RF and Microwave Circuit Integration: direct-coupled cavity bandpass filters with Chebyshev response. *IEEE Access*, 3:1313-1325, July.

Tsui, J.B.1992.*Microwave receivers with electronic warfare applications*. New York, NY: John Wiley.

University of Toyko CubeSat Team. n.dhttp://www.space.t.u-tokyo.ac.jp/cubesat/mission/dev/com/old-e.html[30 August 2017].

Wang, K., Wong, S., Sun, G., Chen, Z.N., Zhu, L. & Chu, Q. 2015. Synthesis method for substrate integrated waveguide bandpass filter with even-order Chebyshev response. *IEEE Transactions on Components, Packaging and Manufacturing Technology*, 6(1):126-135, December.

Wu, K. 2001. Integration and interconnect techniques of planar and non-planar structures for microwave and millimeter-wave circuits – current status and future trend. In *Proceedings of the 2001 Asia-Pacific Microwave Conference, Taipei, Taiwan, 3–6 December*. Piscataway, NJ: IEEE: 411-416.

Xie, X., Zhong, Z. & Guo, Y. 2014. X-band predistortion linearized GaN HPA for broadband satellite communications. In *Proceedings of the 2014 IEEE International Conference on Communication Systems, Macau, China, 19–21 November*. IEEE: 433-436.

Xu, F. & Wu, K. 2005. Guided-wave and leakage characteristics of substrate integrated waveguide. *IEEE Transactions on Microwave Theory and Techniques,* 53(1):66-73, January.

Xu, Z.Q., Shi, Y., Wang, P. Liao, J.X. & Wei, X.B. 2012. Substrate integrated waveguide (SIW) filter with hexagonal resonator. *Journal of Electromagnetic Waves and Applications*, 26(11-12):1521-1527, August.

Zheng, B.,Zhao, Z. & Lv, Y. 2010. A K-band SIW filter with bypass coupling substrate integrated circular cavity (SICC) to improved stopband performance for satellite communication. *Progress In Electromagnetics Research C*,17:95-104, November.

Zobel, O.J. 1923. Theory and design of uniform and composite electric wave-filters. *The Bell System Technical Journal*, 2(1):1-46, January.

APPENDICES

APPENDIX A: Matlab code used to calculate and plot the transfer and reflection characteristics of the filter

```
%.......................................................
% 1.CALCULATION OF REFLECTION ZEROS, TRANSMISSION/REFLECTION POLES
%  POLYNOMIALS F(S), P(S) AND E(S)
%   OF y21(s) AND y22(s)
%.......................................................

clear;
symss;
f1=8e9;   % lower cutofffreq of the passband filter
f2=8.5e9;   % upper cutofffreq of the passband filter
BW=f2-f1;   % passband bandwidth
f0=sqrt(f2*f1);   % centre frequency
fTZ1=5.8e9;   % first transmission zero
fTZ2=7e9;   % second transmission zero
fTZ3=Inf;   % third transmission zero
fTZ4=Inf;   % fourth transmission zero


RL=25;   % Return loss in dB
wTZ1=f0/BW*((fTZ1/f0)-(f0/fTZ1));%first normalized TX zero of BPF
wTZ2=f0/BW*((fTZ2/f0)-(f0/fTZ2));%second normalized Tx zero of BPF
wTZ3=Inf;                                    % third normalized Tx zero of BPF
wTZ4=Inf;                                    % Forth normalized Tx zero of BPF
wTZ5=Inf;   % Firth normalized Tx zero of BPF
wTZ6=Inf;   % sixth normalized Tx zero of BPF
wTZ7=Inf;   % seventh normalized Tx zero of BPF
symsws;
wz=sqrt((w^2)-1);%wz- transformed frequency variable given as w'by Cameron

U1=w-(1/wTZ1);
V1=(sqrt((w^2)-1))*(sqrt(1-(1/wTZ1^2)));
U1=simplify(U1);
U1=vpa(collect(U1),5);
V1=simplify(V1);
V1=vpa(collect(V1),5)



U2=w*U1-(U1/wTZ2)+((sqrt(1-wTZ2^-2))*(sqrt((w^2)-1))*V1);
V2=w*V1-(V1/wTZ2)+((sqrt(1-wTZ2^-2))*(sqrt((w^2)-1))*U1);
U2=simplify(U2);
U2=vpa(collect(U2),5);
V2=simplify(V2);
V2=vpa(collect(V2),5);

U3=w*U2-(U2/wTZ3)+((sqrt(1-wTZ3^-2))*(sqrt((w^2)-1))*V2);
V3=w*V2-(V2/wTZ3)+((sqrt(1-wTZ3^-2))*(sqrt((w^2)-1))*U2);
U3=simplify(U3);
U3=vpa(U3,5);
V3=simplify(V3);
V3=vpa(V3,5);

U4=w*U3-(U3/wTZ4)+((sqrt(1-wTZ4^-2))*(sqrt((w^2)-1))*V3);
V4=w*V3-(V3/wTZ4)+((sqrt(1-wTZ4^-2))*(sqrt((w^2)-1))*U3);
U4=simplify(U4)
```

```matlab
U4=vpa(U4,6)
U4=vpa(subs(U4,w,s*-j),5)
V4=simplify(V4)/wz;
V4=vpa(V4,5);
V4=vpa(subs(V4,w,s*-j),5)


U5=w*U4-(U4/wTZ5)+((sqrt(1-wTZ5^-2))*(sqrt((w^2)-1))*V4);
V5=w*V4-(V4/wTZ5)+((sqrt(1-wTZ5^-2))*(sqrt((w^2)-1))*U4);
U5=simplify(U5);
U5=vpa(U5,5);

V5=simplify(V5);
V5=vpa(V5,5);

U6=w*U5-(U5/wTZ6)+((sqrt(1-wTZ6^-2))*(sqrt((w^2)-1))*V5);
V6=w*V5-(V5/wTZ6)+((sqrt(1-wTZ6^-2))*(sqrt((w^2)-1))*U5);
U6=simplify(U6);
U6=vpa(U6,5);
V6=simplify(V6);
V6=vpa(V6,5);

U7=w*U6-(U6/wTZ5)+((sqrt(1-wTZ5^-2))*(sqrt((w^2)-1))*V6);
V7=w*V6-(V6/wTZ5)+((sqrt(1-wTZ5^-2))*(sqrt((w^2)-1))*U6);
U7=simplify(U7);
U7=vpa(U7,5);
V7=simplify(V7);
V7=vpa(V7,5);

%.....................................................
% 1.1 Calculation of the roots of V4s,the IN-BAND REFLECTION MAXIMAE
%.....................................................

v=sym2poly(V4);   % Extract the coefficients of V4
Vs_roots=roots(v)  % Calculate the roots of V4 which are the In-band
% Reflection Maximae

%.....................................................
% 1.2 Calculation of the roots of Fs(Numerator of S11),the REFLECTION ZEROS
%.....................................................

p=sym2poly(U4);   % Extract the coefficients of U4
Fs_roots=roots(p) %calculate the roots of U4 which are the Reflection Zeros



%.....................................................
% 1.3 Prescribed TZ
%.....................................................

Ps=(s-j*wTZ1)*(s-j*wTZ2);% prescribed set of TZ make up polynomial P(s).
Ps=expand(Ps);
Ps=vpa(Ps,5);
Ps_coeff=sym2poly(Ps);
Ps_roots=roots(Ps_coeff)



%.....................................................
% 1.4 Calculation of the roots of polynomial Es(Denominator of S21 & S21) % % from  the known Ps
and Fs (calculated above)
%.....................................................
U41=vpa(U4/(real(p(1:1))+imag(p(1:1))),5)% Normalising to the highest
```

```matlab
Fs=vpa(subs(U41,s,j),5)                      % degree coefficient
Ps2=vpa(subs(Ps,s,j),5)
e=(1/sqrt(-1+10^(RL/10)))*abs(Ps2/Fs)


%er=e/sqrt(e^2-1)                 % er for fully canonical function
er=1;   % er for partial canonical function
Es=(Ps*er)-(j*U41*e);
Es=simplify(Es);
Es=vpa(Es,5);
E=sym2poly(Es)
Es_roots=roots(E)


Es1=(Ps*er)+(j*U41*e);
Es1=simplify(Es1);
Es1=vpa(Es1,5);
E1=sym2poly(Es1)
Es1_roots=roots(E1)
%...................................................................
%1.4.1 Plotting the pattern of the roots of E(s)E(s)*
%...................................................................
set(0,'DefaultAxesFontName','Arial')
set(0,'DefaultAxesFontSize',10)
figure(1)
scatter(real(Es_roots),imag(Es_roots),'filled','red')
hold on
scatter(real(Es1_roots),imag(Es1_roots),'filled','red')
hold off

xlabel('Real')
ylabel('Imaginary')
title('Pattern of the roots of E(s)E(s)*')
%...................................................................
%1.5 Calculation of the coeffients polynomial Fs(Numerator of %S11)normilised to the highest degree
coefficient
%...................................................................

Fs_coeff=sym2poly(U41)

Fs_coeff=flip(Fs_coeff)           % Ordering coefficients from  lowest
% to the highest degree.


%...................................................................
% 1.6 Calculation of the coeffients polynomial Ps(Numerator of S21) from
% the prescribed TZ
%...................................................................

Ps1=Ps*j;   % For N-nfz=even, coefficients of P(s)are multiplied
                                 % by j.
Ps_coeff=sym2poly(Ps1) % coefficients of S21 Numerator polynomial P(s).
Ps_coeff=flip(Ps_coeff)% Ordering coefficients from lowest to the highest
% degree.


%...................................................................
% 1.7 Calculation of the coefficients of polynomial Es(Denominator of S11 & S21)
%    normalised to the highest degree coefficient
%...................................................................
Ez=(s-(-0.3222-j*1.2782))*(s-(-0.8679-j*0.6496))*(s-(-1.0064+j*0.4355))*(s-(-0.4606+j*1.3571))
Ez=expand(Ez);
Ez=vpa(Ez,5);
Es_coeff=sym2poly(Ez)
Es_coeff=flip(Es_coeff)
```

```
%........................................................
%1.8 Plotting transfer and reflection characteristics(S11& S21) from
%the polynomials F(s),P(s) and E(s).
%........................................................

s11=vpa(U41/Ez/er,3)
s21=vpa(Ps1/Ez/e,3)

s11=vpa(subs(s11,s,s*i),3); % Substituting s with imaginary unit i for
s21=vpa(subs(s21,s,s*i),3); % plotting S11 and S21 using normalized freq
S11=[];
S21=[];

for a=-17.2:0.02:6.4        % a=s= Normalized freq, imaginary unit i
% already added in the equations
   S11=[S11,(subs(s11,s,a))];
   S21=[S21,(subs(s21,s,a))];

end

x=-17.2:0.02:6.4;
set(0,'DefaultAxesFontName','Arial')
set(0,'DefaultAxesFontSize',10)
figure(2)
plot(x,(20*log10(abs(S11))),'k',x,(20*log10(abs(S21))),'b')% plotting
                                                      %magnitude of S11 & S21
legend('S11','S21')
grid on
grid minor
xlim([-17.2 6.4])
ylim([-110 3])
xlabel('Normalized frequency')
ylabel('Rejection/return loss (dB)')
title('Transfer and reflection characteristics of the prototype filter')

%........................................................
% 2.CALCULATION OF COEFICIENTS OF NUMERATOR AND DENOMINATOR POLYNOMIALS
%   OF y21(s) AND y22(s)
%........................................................

%........................................................
% 2.1 Calculation of complex-even m1, m1=yd(s),the denominator of polynomial
% y22(s) and y21(s), for N=even
%........................................................

m1=
real(Es_coeff(1:1)+Fs_coeff(1:1))+j*imag(Es_coeff(2:2)+Fs_coeff(2:2))*s+real(Es_coeff(3:3)+Fs_coeff
(3:3))*s^2+j*imag(Es_coeff(4:4)+Fs_coeff(4:4))*s^3+real(Es_coeff(5:5)+Fs_coeff(5:5))*s^4;
m1=simplify(m1);
m1=vpa(m1,5);
m=sym2poly(m1);
m1_coeff=m /(real(m(1:1))+imag(m(1:1)));% Normalising coefficients of m1
%(m1=yd(s),denominator of polynomial
% y22(s)and y21(s),for N=even)to
% the highest degree coefficient.

m1_coeff=flip(m1_coeff)   % Ordering coefficients from lowest
% to the highest degree.

%........................................................
```

% 2.2 Calculation of complex-odd polynomial n1, n1= y22n(s), the numerator
% of polynomial y22(s), for N=even.
%..

n1=j*
imag(Es_coeff(1:1)+Fs_coeff(1:1))+real(Es_coeff(2:2)+Fs_coeff(2:2))*s+j*imag(Es_coeff(3:3)+Fs_coef
f(3:3))*s^2+real(Es_coeff(4:4)+Fs_coeff(4:4))*s^3+j*imag(Es_coeff(5:5)+Fs_coeff(5:5))*s^4;
n1=simplify(n1);
n1=vpa(n1,5);
n=sym2poly(n1);
n1_coeff=n /(real(m(1:1))+imag(m(1:1)));% Normalising coefficients of n1
%(n1=y22n(s),numerator of polynomial
% y22(s),for N=even)to the highest
% degree coefficient of m1=yd(s),
% the denominator of polynomial y22(s)
% and y21(s),for N=even).

n1_coeff=flip(n1_coeff)   % Ordering coefficients from lowest
% to the highest degree.

%..
% 2.3 Calculation of y21n(s),the numerator of polynomial y21(s),for N=even.
%..

y21ns=Ps1/e;   % y21ns is the numerator of the
% polynomial y21.
y21ns=simplify(y21ns);
y21ns=vpa(y21ns,5);

y21n_coeff=sym2poly(y21ns);   % coefficients of polynomial y21(s)).

y21ns_coeff=y21n_coeff/(real(m(1:1))+imag(m(1:1)));% Normalising
%coefficients of y21ns,numerator of polynomial
% y21(s),for N=even)to the highest
% degree coefficient of m1=yd(s),
%(the denominator of polynomial y22(s)
% and y21(s),for N=even).

y21ns_coeff=flip(y21ns_coeff)   % Ordering coefficients from lowest
% to the highestdegree.

%..
% 3.CALCULATION OF RESIDUES,EIGENVALUE AND EIGENVECTORS
%..

%..
% 3.1 Finding the residues of y21(s) and y22(s)
%..

r21=residue(y21n_coeff,m)   % residue r21k
r22=residue(n,m)   % residue r22
lambda_k=-j*roots(m)   % Eigen values = roots of yds

APPENDIX B: Matlab code used for the reduction of the transversal coupling matrix to the folded form

```matlab
% [3,4]
% COLUMN 4
clear;
mss=0;
mll=0;
M21=0;
M12=0;
M31=0;
M13=0;
M32=0;
M23=0;
M41=0;
M14=0;
M42=0;
M24=0;
M43=0;
M34=0;
Msl=0;
Mls=0;
Mll=0;
M1s=-0.4355;
Ms1=M1s;
M1l=0.4355;
Ml1=M1l;
M2s=0.6467;
Ms2=M2s;
M2l=0.6467;
Ml2=M2l;
M3s=-0.6889;
Ms3=M3s;
M3l=0.6889;
Ml3=M3l;
M4s=0.4960;
Ms4=M4s;
M4l=0.4960;
Ml4=M4l;
M11=1.4502;
M22=0.8322;
M33=-0.6075;
M44=-1.5397;
tetha1=-atand(M4s/M3s);
c1=cosd(tetha1);
s1=sind(tetha1);

ms4=s1*Ms3+c1*Ms4;
m14=s1*M13+c1*M14;
m24=s1*M23+c1*M24;
m34=M34*(c1^2-s1^2)+s1*c1*(M33-M44);
m44=s1^2*M33+2*s1*c1*M34+c1^2*M44;
ml4=s1*Ml3+c1*Ml4;
% column3
ms3=c1*Ms3-s1*Ms4;
m13=c1*M13-s1*M14;
m23=c1*M23-s1*M24;
m33=c1^2*M33-2*s1*c1*M34+s1^2*M44;
m43=m34;
ml3=c1*Ml3-s1*Ml4;
```

```
m1=[mss Ms1 Ms2 ms3 ms4 Msl;M1s M11 M12 m13 m14 M1l;M2s M21 M22 m23 m24 M2l;ms3 m13
m23 m33 m34 ml3;ms4 m14 m24 m34 m44 ml4;Mls Ml1 Ml2 ml3 ml4 Mll];

m=m1

%[2;3]
% column3

Mss=mss;
Ms3=ms3;
Ms4=ms4;
M13=m13;
M14=m14;
M23=m23;
M24=m24;
M3s=ms3;
M33=m33;
M34=m34;
M43=m34
M44=m44;
Ml3=ml3;
Ml4=ml4;

tetha2=-atand(M3s/M2s);
c2=cosd(tetha2);
s2=sind(tetha2);
ms3=s2*Ms2+c2*Ms3;
m13=s2*M12+c2*M13;
m23=M23*(c2^2-s2^2)+s2*c2*(M22-M33)
m33=s2^2*M22+2*s2*c2*M23+c2^2*M33;
m43=s2*M42+c2*M43
ml3=s2*Ml2+c2*Ml3;

%column2
ms2=c2*Ms2-s2*Ms3;
m12=c2*M12-s2*M13;
m22=c2^2*M22-2*s2*c2*M23+s2^2*M33;
m32=M23*(c2^2-s2^2)+s2*c2*(M22-M33);
m42=c2*M42-s2*M43
ml2=c2*Ml2-s2*Ml3;

m2=[mss Ms1 ms2 ms3 ms4 Msl;Ms1 M11 m12 m13 m14 M1l;ms2 m12 m22 m32 m42 ml2;ms3 m13
m23 m33 m43 ml3;ms4 m14 m42 m43 m44 ml4;Msl Ml1 ml2 ml3 ml4 Mll];

m2=m2

%[1;2]
% column2
Ms2=ms2
Ms3=ms3
M12=m12
M13=m13
M22=m22
M32=m32
M42=m42
Ml2=ml2
M23=m23
M33=m33
M43=m43
Ml3=ml3
Ms4=ms4
```

```
M14=m14
M44=m44
Ml4=ml4


tetha3=-atand(Ms2/Ms1);
c3=cosd(tetha3);
s3=sind(tetha3);


ms2=s3*Ms1+c3*Ms2;
m12=M12*(c3^2-s3^2)+s3*c3*(M11-M22)
m22=s3^2*M11+2*s3*c3*M12+c3^2*M22;
m32=s3*M31+c3*M32;
m42=s3*M41+c3*M42
ml2=s3*Ml1+c3*Ml2;
%column1
ms1=c3*Ms1-s3*Ms2;
m11=c3^2*M11-2*s3*c3*M12+s3^2*M22;
m21=M12*(c3^2-s3^2)+s3*c3*(M11-M22);
m31=c3*M31-s3*M32;
m41=c3*M41-s3*M42
ml1=c3*Ml1-s3*Ml2;

m3=[mss ms1 ms2 ms3 ms4 Msl;ms1 m11 m12 m31 m41 ml1;ms2 m12 m22 m32 m42 ml2;ms3 m31
m32 m33 m43 ml3;ms4 m41 m42 m43 m44 ml4;Msl ml1 ml2 ml3 ml4 Mll];


m3=m3
%[2;3]
% column3

Ms2=ms2;
M12=m12;
M22=m22;
M32=m32
M23=m32;
M42=m42;
Ml2=ml2;
Ms1=ms1;
M11=m11;
M21=m21;
M31=m31;
M13=m31;
M41=m41;
Ml1=ml1


tetha5=atand(Ml2/Ml3);
c5=cosd(tetha5);
s5=sind(tetha5);


ms3=s5*Ms2+c5*Ms3;
m13=s5*M12+c5*M13;
m23=M23*(c5^2-s5^2)+s5*c5*(M22-M33)
m33=s5^2*M22+2*s5*c5*M23+c5^2*M33;
m43=s5*M42+c5*M43
ml3=s5*Ml2+c5*Ml3;


%column2
ms2=c5*Ms2-s5*Ms3;
m12=c5*M12-s5*M13;
m22=c5^2*M22-2*s5*c5*M23+s5^2*M33;
m32=M23*(c5^2-s5^2)+s5*c5*(M22-M33);
```

```
m42=c5*M42-s5*M43
ml2=c5*Ml2-s5*Ml3;


m5=[mss ms1 ms2 ms3 ms4 Msl;ms1 m11 m12 m13 m41 ml1;ms2 m12 m22 m32 m42 ml2;ms3 m13
m32 m33 m43 ml3;ms4 m41 m42 m43 m44 ml4;Msl ml1 ml2 ml3 ml4 Mll];


m5=m5


%[3,4]
Ms3=ms3
Ms4=ms4
M13=m13
M41=m41
M14=m41
M32=m32
M23=m32
M42=m42
M24=m42
M33=m33
M43=m43
M34=m43
Ml3=ml3
M44=m44
Ml4=ml4;


tetha6=atand(Ml3/Ml4);
c6=cosd(tetha6);
s6=sind(tetha6);
%column 4
ms4=s6*Ms3+c6*Ms4;
m14=s6*M13+c6*M14;
m24=s6*M23+c6*M24;
m34=M34*(c6^2-s6^2)+s6*c6*(M33-M44);
m44=s6^2*M33+2*s6*c6*M34+c6^2*M44;
ml4=s6*Ml3+c6*Ml4;
% column3
ms3=c6*Ms3-s6*Ms4;
m13=c6*M13-s6*M14;
m23=c6*M23-s6*M24;
m33=c6^2*M33-2*s6*c6*M34+s6^2*M44;
m43=m34;
ml3=c6*Ml3-s6*Ml4;


m6=[mss ms1 ms2 ms3 ms4 Msl;ms1 m11 m12 m13 m14 ml1;ms2 m12 m22 m23 m24 ml2;ms3 m13
m23 m33 m43 ml3;ms4 m14 m24 m43 m44 ml4;Msl ml1 ml2 ml3 ml4 Mll];


m6=m6




%[2,3]
Ms2=ms2
Ms3=ms3
M12=m12
M13=m13
M22=m22
M23=m23
M24=m24
M42=m24
Ml2=ml2
M33=m33
```

```
M43=m43
Ml3=ml3


Ms3=ms3;
M13=m13
M23=m23
M24=m24
M42=m24
Ms3=ms3
M33=m33
M34=m34
M43=m34
Ml3=ml3;
tetha6=-atand(M13/M12);
c6=cosd(tetha6);
s6=sind(tetha6);


ms3=s6*Ms2+c6*Ms3;
m13=s6*M12+c6*M13;
m23=M23*(c6^2-s6^2)+s6*c6*(M22-M33)
m33=s6^2*M22+2*s6*c6*M23+c6^2*M33;
m43=s6*M42+c6*M43
ml3=s6*Ml2+c6*Ml3;


%column2
ms2=c6*Ms2-s6*Ms3;
m12=c6*M12-s6*M13;
m22=c6^2*M22-2*s6*c6*M23+s6^2*M33;
m32=M23*(c6^2-s6^2)+s6*c6*(M22-M33);
m42=c6*M42-s6*M43
ml2=c6*Ml2-s6*Ml3;


m6=[mss ms1 ms2 ms3 ms4 Msl;ms1 m11 m12 m13 m14 ml1;ms2 m12 m22 m23 m42 ml2;ms3 m13
m23 m33 m43 ml3;ms4 m14 m42 m43 m44 ml4;Msl ml1 ml2 ml3 ml4 Mll];
m6(1,2)=abs(m6(1,2));
m6(2,1)=abs(m6(2,1));
m6=m6
```